



**HIGH FREQUENCY MAGNETIC FIELD DIRECTION FINDING USING
MGL-S8A B-DOT SENSORS**

THESIS

Michael D. Archer, Captain, USAF

AFIT-ENG-13-M-02

**DEPARTMENT OF THE AIR FORCE
AIR UNIVERSITY**

AIR FORCE INSTITUTE OF TECHNOLOGY

Wright-Patterson Air Force Base, Ohio

DISTRIBUTION STATEMENT A:
APPROVED FOR PUBLIC RELEASE; DISTRIBUTION UNLIMITED

The views expressed in this thesis are those of the author and do not reflect the official policy or position of the United States Air Force, the Department of Defense, or the United States Government.

This material is declared a work of the U.S. Government and is not subject to copyright protection in the United States.

AFIT-ENG-13-M-02

HIGH FREQUENCY MAGNETIC FIELD DIRECTION FINDING USING MGL-S8A
B-DOT SENSORS

THESIS

Presented to the Faculty
Department of Electrical and Computer Engineering
Graduate School of Engineering and Management
Air Force Institute of Technology
Air University
Air Education and Training Command
in Partial Fulfillment of the Requirements for the
Degree of Master of Science in Electrical Engineering

Michael D. Archer, B.S.E.E.

Captain, USAF

March 2013

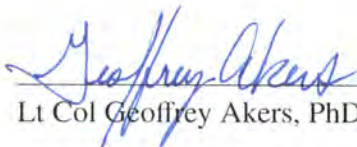
DISTRIBUTION STATEMENT A:
APPROVED FOR PUBLIC RELEASE; DISTRIBUTION UNLIMITED

AFIT-ENG-13-M-02


HIGH FREQUENCY MAGNETIC FIELD DIRECTION FINDING USING MGL-S8A
B-DOT SENSORS

Michael D. Archer, B.S.E.E.
Captain, USAF

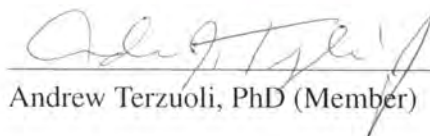
Approved:


Lt Col Geoffrey Akers, PhD (Chairman)

11 Feb 2013
Date


Michael Havrilla, PhD (Member)

11 Feb 2013
Date


Andrew Terzuoli, PhD (Member)

11 Feb 2013
Date

Abstract

Aircraft based direction finding (DF) in the high frequency (HF) band is difficult due to the aircrafts size with respect to wavelength and limited azimuthal resolution. A B-dot sensor is useful for detection of the time varying magnetic field and offers improved integration into an aircraft over classical antennas designed for detecting the electric field. What the B-dot sensor gains in integration it gives up in sensitivity because it is designed for frequencies above 5 GHz. Design of an airborne HFDF array using B-dot sensors is based in maximizing the physical extent of the array and eliminating multiple main beams.

The goals of this research are to complete a computational analysis of a B-dot sensor, evaluate a cluster of closely spaced B-dot sensors, and design an array of B-dot sensor clusters on a simulated airborne HFDF platform. The B-dot sensors are simulated to determine the farfield characteristics and sensitivity of the sensor and a sensor cluster. Eight and ten-sensor elements are placed on a simulated airframe to characterize the direction finding capability of an airborne array in the 2-32 MHz band. The simulated patterns are compared to a previous HFDF design based on the sensitivity of particular array elements. Additionally, a field test is accomplished to compare the simulated B-dot sensor cluster to an actual cluster of B-dot sensors.

The B-dot sensor is inadequate for use in an HFDF array due to a lack of sensitivity, but based on initial simulations a larger B-dot sensor, designed for 700 MHz, offers equivalent sensitivity to previous research. Utilizing a cluster of sensors improves the radiation efficiency by 6 dB; therefore, with a more efficient sensor the cluster can assist in improving signal to noise ratio (SNR). The eight and ten-element arrays offer a limited direction finding capability due to less than 10 dB sidelobe reduction from the main lobe. The addition of two sensors does present sidelobe reduction; therefore, additional sensors will improve the direction finding capability of the airborne HFDF array.

Acknowledgments

I must first thank my thesis advisor Lt Col Akers. Your diligence and drive to assist me through the research and thesis writing process is the reason I was able to accomplish the work presented here. Your availability to assist with my questions and concerns made the research process an enriching learning experience for me. I only hope that my accomplishments have met and hopefully exceeded your expectations and my efforts have moved you and AFRL forward in this area of research.

I want to thank my committee members, Dr. Terzouli and Dr. Havrilla, for assistance in completing this thesis. Your insight into how to improve my research helped me to better understand the research process from theory to execution. Additionally, I would like to thank Mr. Scott Goodman. Without our two hour discussions on electromagnetic theory every week I know I wouldn't have gotten so much accomplished while still remembering the fundamentals of this research. Your approach of looking at the physics of a research problem will be an invaluable tool for me in the future.

I want to acknowledge the impact of Matthew Kroening and John Greenwell, members of the SOCHE research team. Your assistance with pouring through the massive amounts of test data was crucial to testing the detection ability of the B-dot sensor cluster. Your excitement and willingness to help in anyway will always be appreciated.

Finally, I would like to thank my wife and daughter for their unending support. Thank you for supporting me through this long journey, because without you I would not have been able to accomplish all I have in my time at AFIT. Whether it was accepting the long nights or the lack of weekends you always smiled and lifted me up when I was tired of the grind. Thank you, and I love you both.

Michael D. Archer

Table of Contents

	Page
Abstract	iv
Acknowledgments	v
Table of Contents	vi
List of Figures	ix
List of Tables	xiv
List of Acronyms	xv
 I. Problem Statement	 1
1.1 Introduction	1
1.2 Research Goals	5
1.2.1 Scope	6
1.2.2 Assumptions	6
1.3 Resource Requirements	7
1.4 Document Overview	7
 II. Background	 9
2.1 Current Research	9
2.1.1 SQUID Sensor	10
2.1.2 Structurally Integrated Monopole Feeds	11
2.1.3 Additional High Frequency Direction Finding Research	12
2.2 Theory	13
2.2.1 B-Dot Functionality	13
2.2.2 Loop Antennas	15
2.2.3 Coupling	19
2.3 Incident Signal Power	21
2.4 Computational Electromagnetics	23
2.5 Array Theory	25
2.6 Conclusion	27

	Page
III. Methodology	28
3.1 Incident Power Analysis	28
3.2 Computational Sensor Characterization	31
3.2.1 Single Sensor Design	31
3.2.2 Sensor Cluster Design	34
3.2.3 B-dot Cluster Array	36
3.3 Non-Uniform Phased Array	41
3.4 MGL-S8A B-dot Field Testing	42
3.4.1 Required Materials	43
3.4.2 Equipment Fabrication	43
3.4.3 Impedance Analysis	43
3.4.4 Test Layout	45
3.4.5 Signal Collection	45
3.4.6 Signal Analysis	46
3.5 Comparison of B-dot Sensor to BerrieHill Structurally Integrated Monopole Feeds	47
3.6 Conclusion	47
IV. Analysis and Results	49
4.1 Single Sensor Characterization	49
4.2 Sensor Cluster Characterization	51
4.3 Eight-Element High Frequency Direction Finding Array Characterization	55
4.4 Ten-Element High Frequency Direction Finding Array Comparison	61
4.5 Non-Uniform Phase Analysis	67
4.6 B-dot Test Analysis	68
4.7 BerrieHill Structurally Integrated Monopole Comparison	73
4.8 Conclusion	78
V. Conclusions and Recommendations	80
5.1 Conclusions	80
5.2 Recommendations and Future Work	82
Appendix A: Pattern Cuts of Eight-Element Direction Finding Array	86
Appendix B: Comparison of Eight and Ten-Element Direction Finding Arrays	93
Appendix C: Sidelobe Level for Eight-Element Arrays	101

	Page
Appendix D: Sidelobe Level for Ten-Element Arrays	104
Appendix E: BerrieHill and MGL-S8A B-dot Sensor Comparison	107
Appendix F: Analysis of B-dot Test Data Using 100 msec Integration Time	109
Appendix G: Specifications Sheet For URS B-dot Sensor	112
Appendix H: Comparison of MGL-S8A Air Gap and FR-4 Gap	113
Appendix I: Boeing 707 General Specifications	114

List of Figures

Figure	Page
1.1 Rivet Joint RC-135 aircraft [1]	2
1.2 MGL-S8A B-dot sensor [2]	2
2.1 High Frequency Active Auroral Research Program array [3]	9
2.2 Simulated structurally integrated (SI) monopole feed locations for high frequency direction finding (HFDF) array at 4 MHz [4]	11
2.3 MGL-S8A B-dot sensor diagram [2]	14
2.4 Loop antenna geometry [5]	17
2.5 Self coupling of incident plane wave on single loop antenna	19
2.6 Mutual coupling between two closely spaced loops	20
2.7 Field definition at each location on a Yee Cell	24
2.8 Phase relationship for incident plane wave on a linear array	26
3.1 B-dot sensor design in CST Microwave Studio	31
3.2 Comparison of 4 sensor cluster of B-dot approximated loop vs. single approximated loop	34
3.3 Field strength of closely spaced equivalent loop based on 0 dBm incident signal	35
3.4 Simulated four sensor cluster	36
3.5 Airborne HFDF B-dot sensor cluster array locations and simulated RC-135 . .	37
3.6 Plane cuts of HFDF array factor at 32 MHz	38
3.7 Plane cuts of HFDF array factor at 17 MHz	39
3.8 Plane cuts of HFDF array factor at 10 MHz	40
3.9 Additional simulated sensor location for reduction in HFDF array sidelobes. . .	41
3.10 18" X 18" ground plane mount for doughnut ground plane	44
3.11 Doughnut ground plane used for B-dot cluster test.	44

Figure	Page
3.12 Common locations for HFDF array for BerrieHill SI monopole feeds and B-dot Sensors	48
4.1 Radiation pattern of a single B-dot sensor at 2 MHz simulated in CST Microwave Studio with an infinite PEC ground plane.	50
4.2 Radiation pattern of a single B-dot sensor at 32 MHz simulated in CST Microwave Studio with an infinite PEC ground plane.	50
4.3 Radiation efficiency of single loop versus B-dot sensor from 2-32 MHz.	51
4.4 Radiation pattern of a B-dot sensor cluster at 2 MHz simulated in CST Microwave Studio with an infinite PEC ground plane.	52
4.5 Radiation pattern of B-dot sensor cluster at 32 MHz simulated in CST Microwave Studio with an infinite PEC ground plane.	52
4.6 Radiation resistance of a four-single loop cluster versus B-dot sensor cluster from 2-32 MHz.	53
4.7 Radiation resistance of single B-dot sensor versus B-dot sensor cluster from 2-32 MHz.	54
4.8 3D detection coverage of 8 sensor simulated array.	54
4.9 Normalized radiation pattern of an eight-cluster HFDF array at 2 MHz simulated in CST Microwave Studio	55
4.10 Normalized radiation pattern of an eight-cluster HFDF array at 16 MHz simulated in CST Microwave Studio	56
4.11 Normalized radiation pattern of an eight-cluster HFDF array at 32 MHz simulated in CST Microwave Studio	56
4.12 XZ plane cut of the directivity of an eight-cluster HFDF array for 2,7,12,17,22,27,32 MHz normalized to 2 MHz	58
4.13 YZ plane cut of an eight-cluster HFDF array for 2,7,12,17,22,27,32 MHz . . .	59

Figure	Page
4.14 Waterline cut of an eight-cluster HFDF array for 2,7,12,17,22,27,32 MHz . . .	60
4.15 Normalized radiation pattern of a ten-cluster HFDF array at 2 MHz simulated in CST Microwave Studio	62
4.16 Normalized radiation pattern of a ten-cluster HFDF array at 16 MHz simulated in CST Microwave Studio	62
4.17 Normalized radiation pattern of a ten-cluster HFDF array at 32 MHz simulated in CST Microwave Studio	63
4.18 Comparison of normalized waterline, XZ, and YZ plane cuts for ten vs eight- cluster array at 2 MHz	63
4.19 Comparison of normalized waterline, XZ, and YZ plane cuts for ten vs eight- cluster array at 16 MHz	64
4.20 Comparison of normalized waterline, XZ, and YZ plane cuts for ten vs eight- cluster array at 32 MHz	65
4.21 Fast Fourier transform of 20-second collection of Dipole, B-dot sensor cluster, and noise from 2-32 MHz	69
4.22 Correlation of 20-second collection of noise to B-dot cluster, noise to dipole, dipole to B-dot cluster and noise to noise	70
4.23 Fast Fourier transform of 20-second collection with 1.25-second integration time of dipole, B-dot sensor cluster, and noise from 2-32 MHz	71
4.24 Correlation of 20-second collection with 1.25-second integration time of noise to B-dot cluster, noise to dipole, dipole to B-dot cluster, and noise to noise . . .	73
4.25 fig: XZ and YZ plane cuts for the theta and phi component of the electric field at 4 MHz of the SI monopole at location one versus B-dot sensor at location one.	74
4.26 XZ and YZ plane cuts for the theta and phi component of the electric field at 11 MHz of the SI monopole at location two versus B-dot sensor at location one.	75

Figure	Page
4.27 Comparison of MGL-S8A B-dot sensor to MGL-5 and MGL-4 variations . . .	77
4.28 Comparison of radiation efficiency of MGL-S8A and MGL-5 B-dot sensors. . .	78
5.1 Example of HFDF array system analysis	83
A.1 Waterline cut of an eight-cluster HFDF array for 2-16 MHz normalized to 2 MHz	87
A.2 Waterline cut of an eight-cluster HFDF array for 17-32 MHz normalized to 2 MHz	88
A.3 XZ plane cut of an eight-cluster HFDF array for 2-16 MHz normalized to 2 MHz	89
A.4 XZ plane cut of an eight-cluster HFDF array for 17-32 MHz normalized to 2 MHz	90
A.5 YZ plane cut of an eight-cluster HFDF array for 2-16 MHz normalized to 2 MHz	91
A.6 YZ plane cut of an eight-cluster HFDF array for 17-32 MHz normalized to 2 MHz	92
B.1 Comparison of normalized waterline, XZ, and YZ plane cuts for ten vs eight- cluster array from 2-6 MHz	94
B.2 Comparison of normalized waterline, XZ, and YZ plane cuts for ten vs eight- cluster array from 7-11 MHz	95
B.3 Comparison of normalized waterline, XZ, and YZ plane cuts for ten vs eight- cluster array from 12-16 MHz	96
B.4 Comparison of normalized waterline, XZ, and YZ plane cuts for ten vs eight- cluster array from 17-21 MHz	97
B.5 Comparison of normalized waterline, XZ, and YZ plane cuts for ten vs eight- cluster array from 22-26 MHz	98
B.6 Comparison of normalized waterline, XZ, and YZ plane cuts for ten vs eight- cluster array from 27-31 MHz	99

Figure	Page
B.7 Comparison of waterline, XZ, and YZ plane cuts for ten vs eight-cluster array at 32 MHz	100
E.1 XZ and YZ plane cuts for the theta and phi component of the electric field at 4 MHz of the SI monopole at location two versus B-dot sensor at location two. .	107
E.2 XZ and YZ plane cuts for the theta and phi component of the electric field at 11 MHz of the SI monopole at location two versus B-dot sensor at location two.	108
F.1 Fast Fourier transform of 20 second collection with 100 msec integration time of dipole, B-dot sensor cluster, and noise from 2-32 MHz	110
F.2 Correlation of 20 second collection with 100 msec integration time of noise to B-dot cluster, noise to dipole, dipole to B-dot cluster, and noise to noise	111
G.1 URS Corporation Specification Sheet for B-dot Sensor Variants	112
H.1 Plot of radiation efficiency results for simulation of an air gap MGL-S8A and an FR-4 filled gap.	113
I.1 Specification sheet for Boeing 707.	115

List of Tables

Table	Page
1.1 Operational characteristics for the primary high frequency signals of interest . .	4
3.1 MGL-S8A measured power out with 6.5 nT input and 10 ms coherent integration time [2]	30
3.2 Range at which 6.5 nT signal levels are reached based on transmitter signals of interest and laboratory test integration time	30
3.3 MGL-S8A B-dot sensor CST design dimensions	31
3.4 Local mesh properties for B-dot sensor characterization	33
3.5 Sensor field test runcard	46
4.1 Average and integrated side lobe level in dB for a sample of frequencies from 2-32 MHz of the eight and ten-element arrays.	66
4.2 Average of the difference between the BerrieHill monopole feeds and the MGL-S8A B-dot sensor electric field components at two common simulated locations for 4 and 11 MHz.	76
C.1 Average and integrated sidelobe level in dB for 2-19 MHz of the eight element array.	102
C.2 Average and integrated sidelobe level in dB for 20-32 MHz of the eight element array.	103
D.1 Average and integrated sidelobe level in dB for 2-19 MHz of the ten element array.	105
D.2 Average and integrated sidelobe level in dB for 20-32 MHz of the ten element array.	106

List of Acronyms

Acronym	Definition
AFRL	Air Force Research Laboratory
AFIT	Air Force Institute of Technology
HFDF	high frequency direction finding
HF	high frequency
DF	direction finding
HF-GCS	High Frequency Global Communications System
FCC	Federal Communications Commission
RF	radio frequency
SPAWAR	Space and Naval Warfare Systems Command
PEC	perfect electric conductor
dB	decibel
EM	electromagnetic
SI	structurally integrated
AOA	angle of arrival
SQUID	superconductive quantum interference device
UAV	unmanned aerial vehicles
MUSIC	Multiple Signal Classification
FDTD	finite difference time domain
PML	perfectly matched layer
AF	array factor
FFT	fast fourier transform
GPU	graphics processing unit
SNR	signal to noise ratio

Acronym	Definition
NF	noise figure
LORE	Low Observables Radar and Electromagnetics
VSWR	voltage standing wave ratio
LNA	low noise amplifier

HIGH FREQUENCY MAGNETIC FIELD DIRECTION FINDING USING MGL-S8A B-DOT SENSORS

I. Problem Statement

IN order to begin research, the topic and execution process must be defined clearly. This chapter will outline the topic of high frequency direction finding (HFDF) including the shortfalls and possible application of an airborne HFDF capability. It will explain the reasons for utilizing the MGL-S8A B-dot sensor for DF compared to conventional antennas. The primary signals of interest in the HF band, 2-32 MHz, will be presented for the purpose of defining possible HFDF sources. Finally, the research goals, scope, assumptions, and required equipment are outlined.

1.1 Introduction

The research effort this thesis presents is a continuation of previous exploration into HFDF at the Air Force Institute of Technology (AFIT) with sponsorship from Air Force Research Laboratory (AFRL) and Space and Naval Warfare Systems Command (SPAWAR). The overall goal of this research is to design a sensor array that can be included on a large body aircraft, such as an Rivet Joint RC-135 airframe, that is capable of performing direction finding operations in the HF band. HF is considered to be 2-32 MHz. Figure 1.1 shows a representative aircraft type for an airborne HFDF system.

This research will focus on evaluating the MGL-S8A B-dot sensor sensitivity in the HF band and the its usefulness in an airborne DF array. The B-dot sensor is shown in Figure 1.2. The MGL-S8A is a half-loop magnetic field sensor that detects the level of the changing magnetic field. The research investigates the use of a four sensor array



Figure 1.1: Rivet Joint RC-135 aircraft [1]



Figure 1.2: MGL-S8A B-dot sensor [2]

cluster to achieve greater signal detection capability. The array is then simulated on a rudimentary aircraft design based on the dimensions of a RC-135. The array layout is based on maximizing directivity and eliminating any possible grating lobes. A non-linear array approach is used in order to minimize sidelobe levels. Though the proposed array design uses the sensor clusters at each simulated location, in order to minimize simulation time a single sensor is used to represent the overall effect of the array. Simulations are evaluated to understand the effectiveness of the airborne array for direction finding in the HF band. Direction finding is the capability to determine angle-of-arrival of a

received signal of interest based the relative phase difference between individual array elements. Though research in improvement of DF algorithms, methods, and arrays has been accomplished, DF capabilities in the HF band are much more difficult due to the wavelength of resonant antennas and the spacing required for adequate phase difference between individual elements. Direction finding requires azimuthal resolution. Spatial extent is required to gain azimuthal resolution within an array design due to the phase differences among individual elements. The differences in phase when the sensors are summed together creates the ability to define angle-of-arrival differentiation due to constructive and destructive interference between individual elements. Additionally, reduction in mutual coupling between sensors is important because the received signal from a sensor must only be based on the incident field and not a combination of the incident field and the reradiated field of nearby sensors or received data will lead to inaccurate field strength levels. For these reasons, aircraft based HFDF is difficult.

In the current saturated telecommunications environment, the Federal Communications Commission (FCC) is requiring all systems that use radio frequency (RF) spectrum to limit bandwidth and power levels in order to maximize the amount of systems that can use the RF spectrum without causing interference. For this reason, the US military is maximizing its capability in frequency ranges that are not typically used. Systems, such as the High Frequency Global Communications System (HF-GCS), used for long distance communications, have existed for years but have not been used due to satellite and higher frequency communications solutions [6]. Expansion of military capability in the 2-32 MHz range, with the use of a functional airborne DF array, could allow for direction finding to be accomplished based on transmissions from the HF-GCS communications towers all over the world, reducing the military reliance on higher frequencies. Additionally, international broadcast stations, Standard Time and Frequency and emergency distress beacons operate in this frequency band. High frequency propagation and power levels allow for much longer

propagation ranges which could give long range navigation ability to an aircraft-based DF array.

This system could also identify signals of interest which would allow for further investigation into transmission by foreign military organizations. Table 1.1 is a list of signals that may be of interest to HF direction finding systems and the signals' associated power levels. The driving force behind continued research in the expansion of this

Table 1.1: Operational characteristics for the primary high frequency signals of interest

Transmitter Type	Frequency	Power
International Broadcast	6.2, 13.57, 21.45 MHz	25, 100, 500 kW
Standard Time and Frequency	10, 15, 20 MHz	10 kW
International Distress	4.2, 8.4, 16.8 MHz	160 W
HF-GCS	6.739, 11.175, 13.2 MHz	1, 4, 10 kW

technology is based upon utilization of all signals across the RF spectrum gains the military the greatest strategic advantage.

Previous research in B-dot sensor characterization by Hardin [2] provides the basis for continued investigation into HFDF. Hardin's research determined if the B-Dot sensor, designed for 5 GHz, could be viable for signal detection within the HF band. From these results it was determined that the B-dot sensor was sensitive enough to detect signals on the order of nano-Tesla in a laboratory environment. Additional research by Corbin [7] evaluated SI antennas designed by BerrieHill Corporation to evaluate the feasibility of HFDF using structurally integrated (SI) monopole feeds. Finally, SPAWAR is developing a cooled sensor that improves the sensitivity of a small sensor at long wavelengths [2].

1.2 Research Goals

This research will analyze expected operational signal levels for HF transmitter systems listed in Table 1.1. The operational signal characterization will determine the background for a better understanding of the signal level requirement for direction finding on an airborne platform. A comparison of Hardin's laboratory measurements to the expected field strength levels for an operational application provides insight into the validity of continued research in the use of B-dot sensors for HFDF. [2].

Computer simulation is completed on a single B-dot sensor and cluster of B-dot sensors. Initial simulations are based on an infinite perfect electric conductor (PEC) boundary eliminating the effect of finite metal seen in the airborne array application. Because the aircraft is not large with respect to wavelength the diffraction effects are impactful due to the traveling waves constructive and destructive interaction that effects the omni-directional pattern of the sensor. If the aircraft was large with respect to wavelength the amplitude of the traveling wave is reduced to a point of not effecting the pattern. If diffraction effects are not large enough to change the pattern it is equivalent to the sensor simulated over an infinite PEC ground plane. This will validate the construction of the B-dot sensors in CST Microwave Studio and validate the effect of a six decibel (dB) increase in radiation efficiency for the four sensor cluster. To understand the capability of the airborne array, the electromagnetic (EM) response the sensors is simulated at various locations on the aircraft to establish an initial baseline for an HFDF airborne array. As discussed earlier, due to the size of the aircraft with respect to wavelength the assumption that each individual antenna pattern is identical no matter where it is place on the aircraft is not valid; therefore, all radiation patterns must be simulated in the presence of the airframe in order to adequately determine the directionality of the airborne array.

To validate computer simulations, a field test is completed. Testing is done based on the use of a truth antenna that has better resonance at HF frequencies compared to the

output of the four B-dot sensor cluster. The ability to detect ambient signals is established through the use of integration and correlation between truth, the B-dot sensor, and noise.

Analysis of BerrieHill SI antenna data is done to determine if the B-dot sensor is an improvement over the SI antennas [4]. Improvements are evaluated based on individual radiation efficiency of co-located elements on the simulated airframe.

1.2.1 Scope.

This research will explore the incorporation of B-dot sensors in an airborne high frequency direction finding array through the use of sensor clusters along with an analysis of the location of the sensors throughout the aircraft. The detailed scope of this thesis is shown below:

1. HF frequency of 2-32 MHz presented for HFDF application,
2. Operation conditions for evaluation are ideal; areas such as multipath and atmospheric losses are not considered,
3. Evaluation of individual array cluster is limited to four sensors, and
4. Overall aircraft system is evaluated using farfield pattern of single sensor.

1.2.2 Assumptions.

This information is presented with the goal of showing the feasibility of the B-dot sensor in airborne HFDF. With HFDF feasibility in mind all outcomes presented are based on the following assumptions:

1. Propagation is in free, unbounded space,
2. Sensors are illuminated by a plane wave (farfield),
3. Current distributions on antennas are uniform,
4. Aircraft orientation is level flight; dynamic flight profiles and changes in incident radiation angles are not examined.

1.3 Resource Requirements

The required resources for completion of the listed thesis objectives include:

1. MATLAB software for array and test data analysis,
2. CST Microwave Studio for electromagnetic evaluation of sensor,
3. High frequency four-port receiver,
4. Doughnut ground plane and tripod,
5. MGL-S8A B-dot sensors (4),
6. Associated lengths low-loss coaxial cable,
7. Signal summers (four port),
8. Radiation patterns from BerrieHill SI antennas.

1.4 Document Overview

This thesis presents a complete analysis of B-dot feasibility for airborne high frequency direction finding. Analysis consists of theoretical explanation of the sensor operation, computational evaluation of sensor capabilities, and a field test evaluation to validate sensor performance. Chapter II outlines the current research areas for HFDF, a theoretical background of B-dot sensor operation, relevant theory to determine expected detection ranges based on previous research by Hardin [2], and a discussion on array theory and how it applies to this research. Chapter III discusses the evaluation of the computational design in CST Microwave Studio, an explanation of the farfield sensor capability, a description of simulated data from farfield array design, a presentation of farfield data collected on SI antennas by BerrieHill Corporation, [4], and a justification for field test process and procedures. Chapter IV contains a comparison of simulated and field test results to determine B-dot operation and array feasibility for HFDF. Additionally,

it presents a comparison of B-dot functionality to that of BerrieHill SI antennas. Finally, Chapter V is a discussion of the viability of B-dot sensors for HFDF and a recommendation for continued research in HFDF.

II. Background

In analyzing the effect and usefulness of this research venture, a thorough understanding of the current research environment is needed. This chapter outlines current research in HFDF and high frequency array design. Additionally, a presentation of the governing theory behind the research methods is shown to clarify the assumptions and steps taken to achieve research goals.

2.1 Current Research

Research in HFDF focuses primarily on naval applications [8]. HFDF is feasible due to the spatial extent of large naval vessels [9]. Additional element spacing allows for adequate phase difference between elements which is more easily achieved due to a larger area over which the array can be defined. Additionally, ships do not have the functional concerns, such as aerodynamic heating, that occur when large antennas are placed on the surface of an aircraft. Large arrays as the one shown in Figure 2.1, are designed for 3-30 MHz [8]. Though this array covers acres and could still not be achieved on a naval vessel,



Figure 2.1: High Frequency Active Auroral Research Program array [3]

a larger sample of this array's capability could be incorporated on naval vessel compared to an aircraft. Previous research has investigated the possibility of reducing the size of high frequency (HF) arrays in order to include them on aircraft, but it is considered to be impossible because the aircraft would give up aerodynamic stability and radar observability

[10]. Additionally, an aircraft would have to be designed solely for the purpose of HFDF due to the size and number of sensors required and the interaction between each sensor and the additional systems on the aircraft which limits aircraft functionality. These observations have focused research in the direction of using non-traditional array design to reduce size. The primary methods are focused on maximizing sensor capabilities using electrically small antennas. Electrically small antennas are limited due to the poor radiation efficiency; therefore, maximizing the efficiency is paramount. Two primary methods have been researched to achieve an efficient isotropic detection capability for HFDF, structurally integrated monopole feeds and superconductive quantum interference device (SQUID) sensors. SI feeds and SQUID sensor research efforts are the primary basis for continued research in determining the feasibility of the MGL-S8A B-dot sensor for HFDF. The B-dot sensor also offers additional characteristics such as reduced cost and non-invasive integration that make the sensor an improvement for HFDF application, if the sensor can detect signals in the HF frequency band.

2.1.1 SQUID Sensor.

SPAWAR is designing a SQUID sensor that utilizes loops to detect the magnetic field [11]. The SQUID sensor is a cryogenic cooled semiconductor material that has the capability to detect signals at 150 pT. Extreme magnetic field sensitivity with limited size makes the sensor a perfect application for an airborne HFDF array, but due to the constraints of cooling the sensor it makes current applications difficult because current temperatures are below the temperature of liquid nitrogen (77° K) [12]. SPAWAR is attempting to achieve high sensitivity at a temperature level that makes it possible to incorporate the SQUID sensors on-board aircraft platforms. Research is ongoing as to how to achieve 150 pT detection at or above 77° K to use this technology on space-limited aircraft such as unmanned aerial vehicles (UAV) [12].

2.1.2 Structurally Integrated Monopole Feeds.

BerrieHill Corporation, with funding from AFRL, researched the use of 10” monopole antennas placed strategically across an aircraft for the application of HFDF. Due to the poor radiation efficiency of the monopoles at HF and the resonance of the aircraft structure, the monopoles are considered feed points for the aircraft and the aircraft is the radiating structure. The monopoles are considered feed points for the aircraft and the aircraft is the radiating structure. The monopole feeds are strategically placed throughout the aircraft at the highest current concentration for a given mode at a given frequency. Monopole placement shown in Figure 2.2 is based on an optimization at 4 MHz. The optimization locates each of

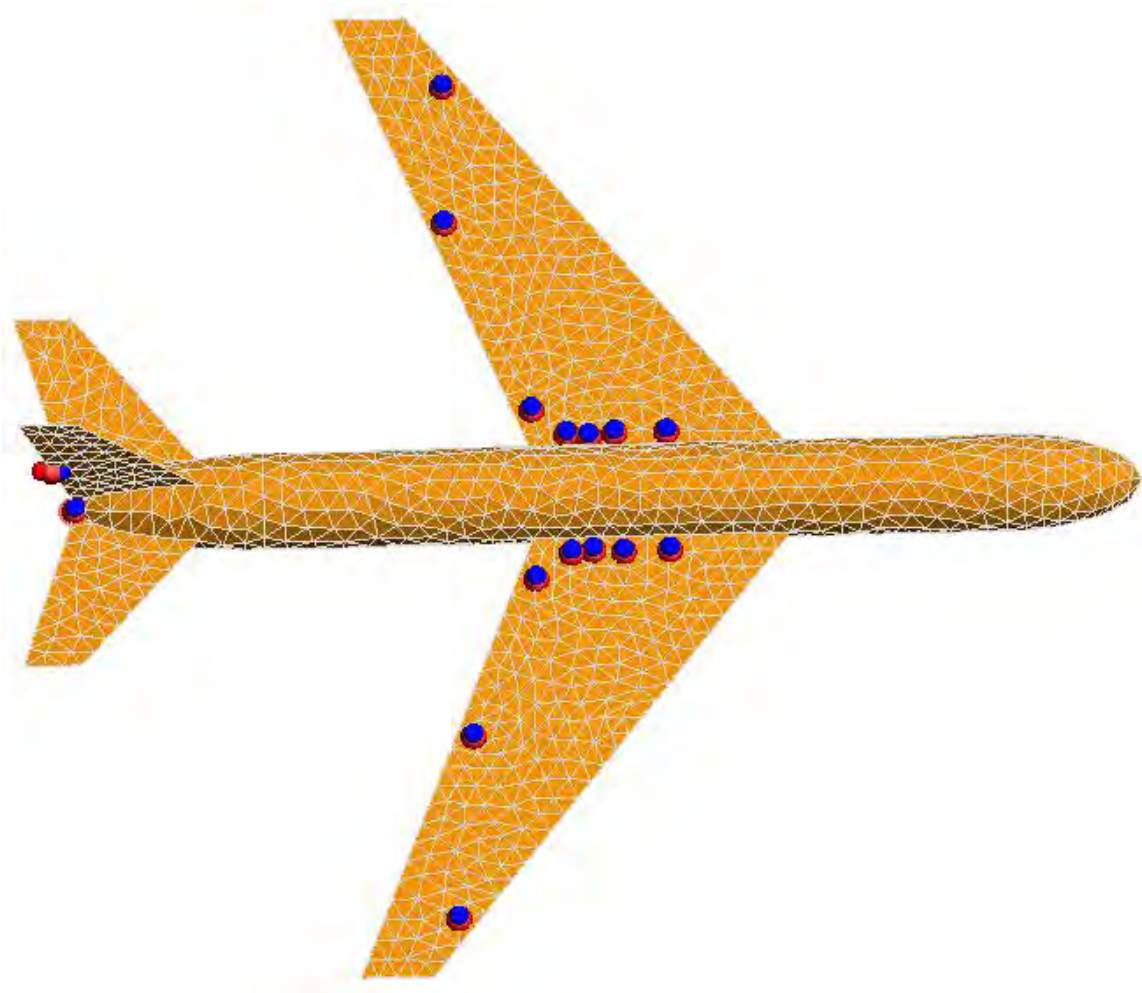


Figure 2.2: Simulated SI monopole feed locations for HFDF array at 4 MHz [4]

the 16 monopoles in order to excite one of the 16 modes that define the farfield at 4 MHz. Optimization of feed locations for the individual modes was also completed at 11 MHz. In determining the best location at each frequency within the HF band the radiation efficiency of the antennas is maximized. This approach does not take into account typical direction finding concepts, such as maximizing the extent of the array on the aircraft or placing the sensors at distances where the phase information can contribute to the determining angle of arrival (AOA).

2.1.3 Additional High Frequency Direction Finding Research.

Along with sensor optimization, methods of direction finding have been investigated by the Air Force Institute of Technology (AFIT) [7], but research is limited because traditional methods are not effective due to individual element spacing. Phased array processing requires distance between each of the independent elements in order to attain the phase information required for azimuthal resolution. Variants on the Multiple Signal Classification (MUSIC) method have been analyzed using half-wave elements and spacing of less than one wavelength [13]. The effectiveness of MUSIC research cannot be directly applied because the B-dot sensor is not equivalent to a half wavelength array element at HF frequencies. Additional research in direction finding techniques must be accomplished in order to better understand the effects of close spacing in direction finding arrays.

Research into analysis and optimization of atmospheric propagation conditions has been investigated as a way to achieve an improved HFDF capability. Ionospheric mapping allows for the optimization of propagation conditions which maximizes HFDF array performance [14]. The addition of propagation optimization into the frequency sweeping in signal collection could make direction finding and the use of typical direction finding methods possible in an operational airborne system, but due to the constantly changing atmospheric conditions the optimization hardware would require constant atmospheric updates and recalculations of optimum frequencies of propagation.

The research background in high frequency direction finding is limited due to the size and complexity of the array designs. A theoretical understanding of the electromagnetic interactions within an array is needed in order to optimize element spacing and polarization to make airborne direction finding possible.

2.2 Theory

An understanding of MGL-S8A B-dot sensor, an understanding of loop antenna functionality, a review of self and mutual coupling effects, and a background into array theory are required for completion of this research. The approximations and assumptions made later in this research will be explained through an analysis of loop antennas and the coupling between individual loops that makes direction finding techniques difficult in the HF band.

2.2.1 *B-Dot Functionality.*

MGL-S8A B-Dot Sensor was designed in 1975 and is a multi-gap loop half cylinder on a ground plane. It is designed to operate at frequencies at or above 5 GHz. The sensor functions under the same principles as a single loop antenna [2]. Figure 2.3 illustrates the design of the MGL-S8A B-dot sensor.

The MGL-S8A sensor detects the magnetic field by measuring two voltages from the multi-gap design. Combining the two measurements causes an averaging of the two gap voltages, improves frequency response, and assists in cancelling the electric field component of the EM wave. The effective area is also half that of the physical size of the sensor due to the half cylinder design [2].

The sensor measures the derivative of time varying magnetic flux density (B). The magnetic flux density is

$$B(t) = B_o \sin(\omega t). \quad (2.1)$$

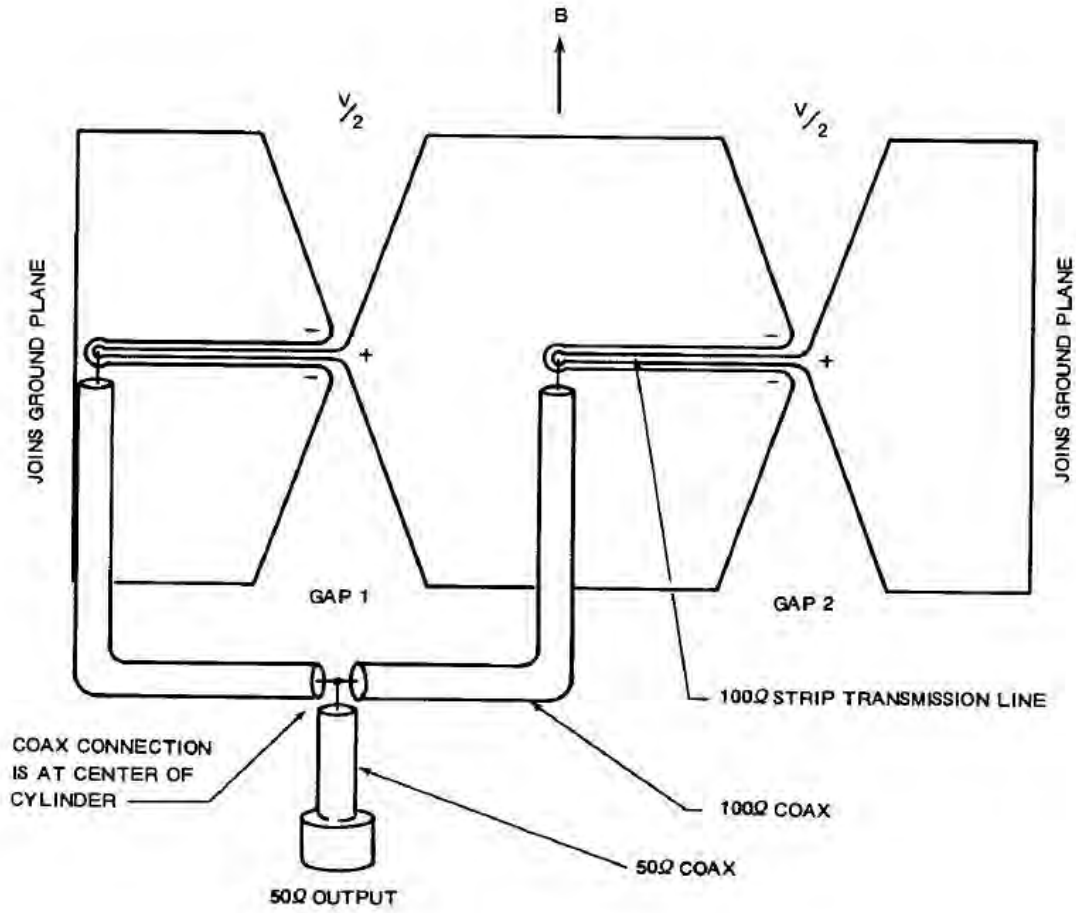


Figure 2.3: MGL-S8A B-dot sensor diagram [2]

The voltage developed across the sensor can be related to the flux density by

$$V(t) = \frac{dB}{dt} * A_{eff} \quad (2.2)$$

where, the A_{eff} is the effective area of the loop sensor. Measuring and summing the voltages across the multi-gap design reduces the noise level by 3 dB due to the random nature of noise [2]. The MGL-S8A B-dot sensor is an improvement on a basic antenna design, the loop antenna. To gain an understanding of the physical design and the method of field measurement, the sensor is characterized by a loop of equivalent size. Loop characterization simplifies electromagnetic field descriptions without losing insight into

the sensor behavior. The definition of basic loop functionality is required for comparison and validation of the B-dot sensor model.

2.2.2 Loop Antennas.

The MGL-S8A B-dot sensor can be described by an electrically small loop; therefore, an understanding of the function and field description of a small loop is required. Any discussion of electromagnetics must first start with the definition of Maxwell's equations, the basis for EM field study. The magnetic field is defined by Maxwell's equations, (2.3) and (2.4), and understanding the interaction between the magnetic and electric field is crucial to determining loop functionality. The equation below is the time harmonic representation of Maxwell's equations [15].

$$\nabla \times \vec{E} = -\vec{\mathfrak{M}}_i - j\omega\vec{B} \quad (2.3)$$

$$\nabla \times \vec{H} = \vec{J}_i + \vec{J}_c + j\omega\vec{D} \quad (2.4)$$

where,

- \vec{E} - electric field intensity (V/m),
- \vec{H} - magnetic field intensity (A/m),
- $\vec{\mathfrak{M}}_i$ - magnetic current density (V/m^2),
- \vec{B} - magnetic flux density ($Tesla$),
- \vec{D} - electric flux density (C/m^2),
- \vec{J}_i - source electric current density (A/m^2),
- \vec{J}_c - conduction current density (A/m^2),
- ω - angular frequency (rad/sec).

The assumptions for this representation of Maxwell's equation are that the propagation must be linear, homogeneous, and isotropic. The research presented meets the listed assumptions because the fields are propagating in free space. Due to free space propagation, the conduction current density is equal to zero. The electric and magnetic fields are defined in this analysis as plane waves. In order to achieve plane wave illumination the distance to the source must be at least 10 wavelengths. At HF, plane wave assumptions are considered valid at slant ranges of 1500 meters [15]. Plane waves are defined by

$$\vec{H} = H_o e^{jk\vec{r}} \quad (2.5)$$

$$k = \omega \sqrt{\epsilon\mu} \quad (2.6)$$

where,

- k - phase constant,
- H_o - amplitude of the magnetic field,
- \vec{r} - direction of propagation,
- ω - angular frequency - rad/sec,
- ϵ_o - permittivity of free space,
- μ_o - permeability of free space.

Based on the previously stated assumption of plane wave illumination and the definition of Maxwell's equations, an understanding of loop antenna functionality can be explained. For the case of a receive antenna the current along the wire, \vec{J}_i , is defined by the incident magnetic field. The curling electric field produced implies, by equation (2.3), that a loop antenna measures the magnetic field. In this way, the loop antenna functions as a magnetic dipole. The development of the equations defining an electric dipole, found in

[15], will directly follow the loop antenna development for the magnetic field. The solution for the single loop antenna is defined based on Figure 2.4.

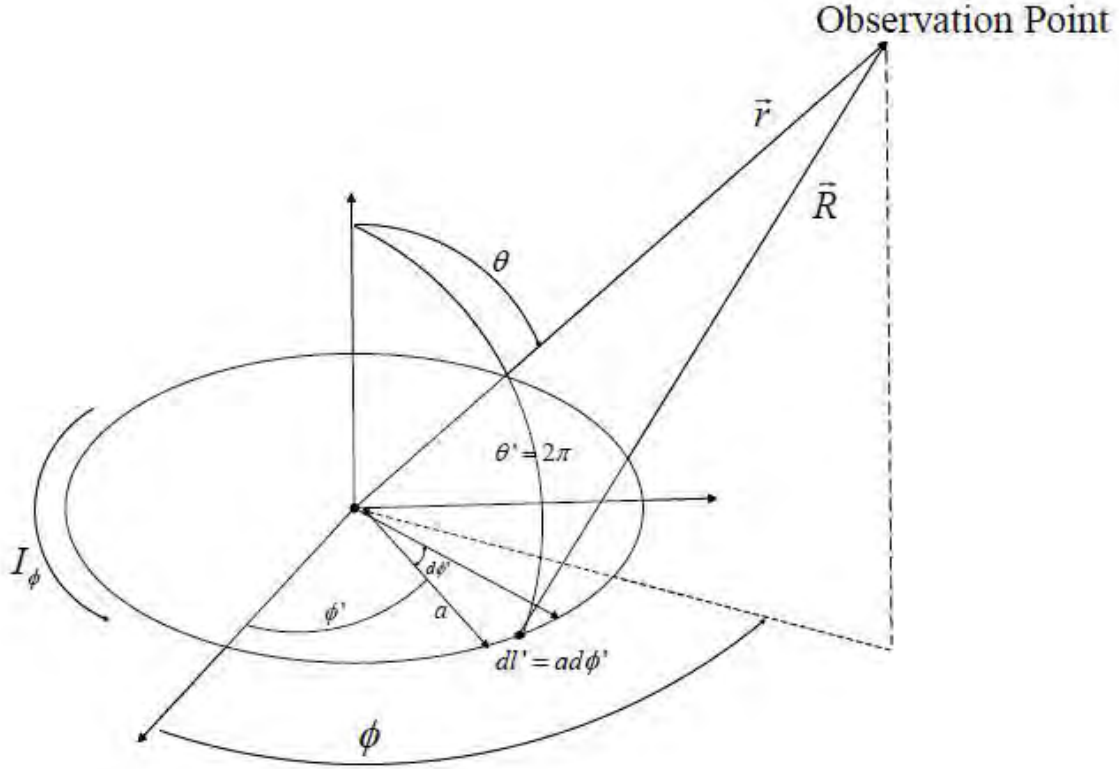


Figure 2.4: Loop antenna geometry [5]

The three assumptions made in defining the solution for a single loop antenna are that the loop is small with respect to wavelength, the diameter of the wire is much smaller than the circumference of the loop, and the current induced by the incident electric field is constant across the wire. The complete derivation of the fields can be found in Balanis [5].

The individual fields for a loop antenna are

$$\vec{H} = \hat{r} j \frac{ka^2 I_0 \cos \theta}{2r^2} \left[1 + \frac{1}{jkr} \right] e^{-jkr} - \hat{\theta} j \frac{(ka)^2 I_0 \cos \theta}{4r} \left[1 + \frac{1}{jkr} - \frac{1}{(kr)^2} \right] e^{-jkr} \quad (2.7)$$

$$\vec{E} = \hat{\phi} \eta \frac{(ka)^2 I_0 \sin \theta}{4r} \left[1 + \frac{1}{jkr} \right] e^{-jkr}. \quad (2.8)$$

where, I_0 is the amplitude of the current induced by the incident field. The field definition above is necessary to understand how the sensors interact at different distances and how an array of sensors will function in the farfield. A description of mutual coupling based on the described field is needed for array analysis [5].

In addition to understanding the field descriptions, the radiation efficiency of the loop antenna allows for initial insight into the expected functionality of the B-dot sensor at HF frequencies. Radiation efficiency evaluates conduction and dielectric losses within a radiating structure [5]. The efficiency quantifies how well an antenna radiates at a given frequency based on its physical design. Radiation efficiency only takes into account conduction and dielectric losses (antenna losses only) not reflection due to a mismatch between the antenna and the transmission line. Since a direct comparison is done based on the radiating structure, reflections will not be considered. Radiation efficiency is defined by the loop antenna loss resistance,

$$R_L = \frac{a}{b} \sqrt{\frac{\omega\mu_0}{2\sigma}} \quad (2.9)$$

where,

- R_L - loss resistance (ohms),
- a - radius of loop (m),
- b - radius of wire (m),
- σ - conductivity of wire (S/m),

and the radiation resistance,

$$R_r = \eta \frac{\pi}{6} (k^2 a^2)^2 \quad (2.10)$$

where R_r is radiation resistance and η is intrinsic impedance [5]. Utilizing the radiation resistance and the loss resistance the radiation efficiency, e_{cd} , can be found by

$$e_{cd} = \frac{R_r}{R_L + R_r}. \quad (2.11)$$

In comparing the radiation efficiency of the loop and the sensor the simulations can be validated and the mutual coupling between adjacent elements can be determined. With the fields and radiation characteristics of the loop antenna defined, self and mutual coupling can be analyzed for consideration in the sensor cluster design.

2.2.3 Coupling.

Coupling is the interaction between a radiating element, the incident field, and adjacent radiators. Self coupling is the relationship of the incident field to the re-radiated fields of the antenna. To understand the effects of mutual coupling, self coupling must be considered. Figure 2.5 shows the theoretical relationship between an incident plane wave on a loop antenna and the re-radiated field by the loop.

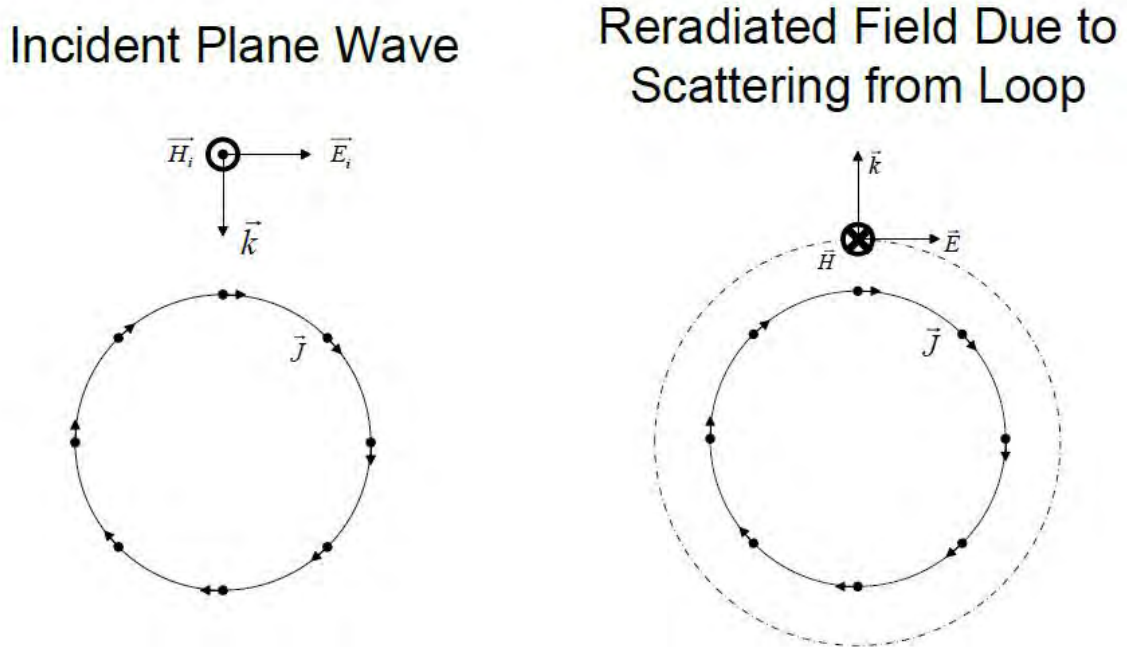


Figure 2.5: Self coupling of incident plane wave on single loop antenna

Figure 2.5 shows the radiated field based on the induced current within the loop by the incident plane wave. It can be seen that the radiated field has an opposing field direction to

in incident field, which implies any closely located loops will have two field components to consider, the incident field and the reradiated field from the scattering of closely spaced elements (mutual coupling).

Mutual coupling is shown in Figure 2.6 Mutual coupling is the interaction

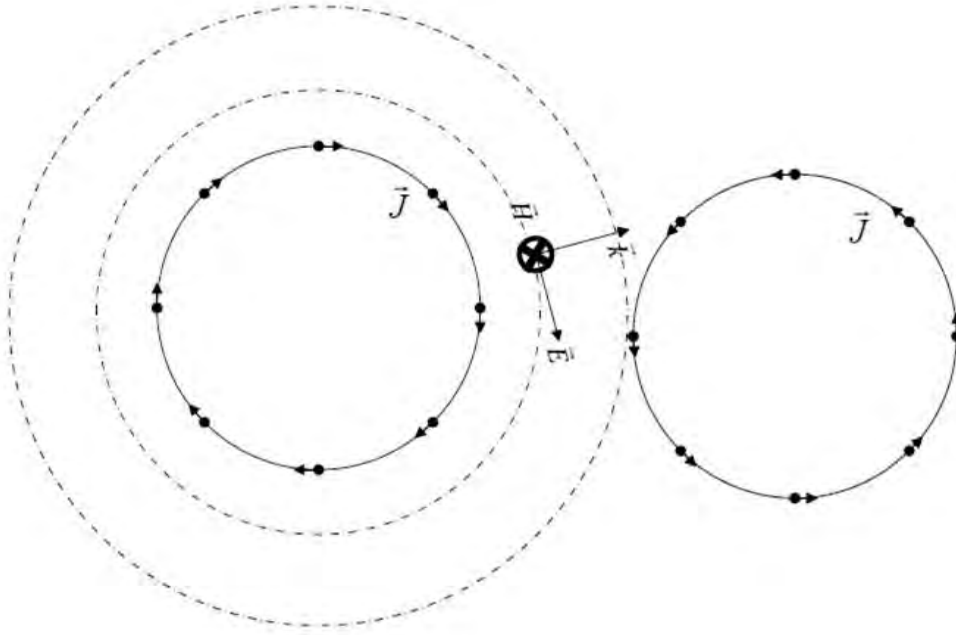


Figure 2.6: Mutual coupling between two closely spaced loops

between closely spaced radiators. To completely define the capability of an array, the electromagnetic fields caused by the incident wave on each of the antennas must be considered though mutual coupling analysis. Additionally, the effects from the excitation of all other antennas on each individual element must be quantified. Array spacing on an aircraft for HFDF is on the order of less than a wavelength at lower frequencies in the high frequency band; therefore, establishing an understanding of how the individual B-dot clusters interact with each other is crucial to determining the validity of the direction finding design. Figure 2.6 describes the excitation of an adjacent loop by the re-radiated field of a loop excited by a plane wave. The current induced on the loop is opposing the current

induced by the incident field. This can cause a reduction in field strength in the two loops. To validate the best design for the four-sensor cluster, mutual coupling must be considered to limit reductions in field strength. The magnitude of the re-radiated field is dependent on the radiation efficiency of the antenna. The incident field must be received and re-radiated by the loop. The process of coupling lowers the signal level by the square of the radiation efficiency. Due to the fact that the B-dot sensor is considered an electrically small antenna, the efficiency will be much less than one; therefore, it is expected that the effect of mutual coupling will be negligible. Radiation efficiency is applied to the positioning of the sensors within the B-dot cluster in later chapters.

2.3 Incident Signal Power

Previous research in airborne HFDF has been in characterizing a useful sensor that can provide adequate response and be easily incorporated into an operational aircraft [2, 4]. As previously stated, research in B-dot characterization was completed in a laboratory setting, and an analysis of appropriate signal levels was not accomplished for the laboratory test. Hardin's testing was performed using a transverse electromagnetic (TEM) cell for characterization of the sensor from 2-32 MHz [2]. The TEM cell is a rectangular transmission line that propagates TEM modes. It operates from 0-1 GHz and is matched to a 50-ohm input at 1.25:1 voltage standing wave ratio (VSWR) or less. The B-dot sensor testing was completed at 6.5 nT signal strength across a frequency range of 2-32 MHz [2].

In order to understand the fields at the aircraft, the transmit power must be related to the power received at the antenna. Equation (2.12) is link equation that defines the signal power density at a given antenna range [16].

$$S = \frac{P_t G}{4\pi R^2} \quad (2.12)$$

where,

- P_t - transmitter site power

- G - gain of antenna
- R - range to site

Power density can be compared to magnetic flux density through the use of Poynting's vector. Poynting's vector defines the power density in an electromagnetic signal based on the magnetic and electric field intensities as shown in equation (2.13) [15].

$$\vec{S} = \vec{E} \times \vec{H} \quad (2.13)$$

where \vec{S} is signal power in W/m^2 . Equations (2.14) through (2.16) relate the magnetic flux density (Tesla) to the power density of the transmitted signal based on free space intrinsic impedance, the permeability of free space, and the effective area of the antenna or sensor [2, 5].

$$|S| = |H|^2 \eta_0 \quad (2.14)$$

$$\vec{B} = \vec{H} \mu_0 \quad (2.15)$$

$$|S| = \frac{|B|^2}{\mu_0^2} \eta_0 \quad (2.16)$$

As stated earlier, the sensor is electrically small and therefore inefficient in the HF band. For this reason additional signal processing may be required. Utilizing the Bartlett method, [17], the data can be separated into subsamples of the overall collection time, N/M where, N is the number of subsamples and M is the number of collections. In this case the number of samples will only be one; therefore, the power levels will be multiplied by M subsamples which can be defined by integration time [17]. For example, if a collection lasts 20 seconds and an integration time of 100 msecs is number of subsamples is $M = 20/.1$, or 200. The Bartlett method changes the power density equation for a single sample to,

$$S = \frac{MP_t G}{4\pi R^2} \quad (2.17)$$

where,

$$M = \frac{IntegrationTime}{CollectionTime}. \quad (2.18)$$

Utilizing a reduced integration time improves the power levels by a factor of M. Power level analysis can determine the validity of previous work and will prove in Chapter III of this thesis if signal levels in the laboratory were representative of signal levels that will be seen for an airborne array application.

2.4 Computational Electromagnetics

In order to simulate the radiation characteristics of the B-dot sensor, B-dot sensor cluster, and aircraft array, computational electromagnetics are used. CST Microwave Studio uses a 3D finite difference time domain (FDTD) method for transient solver calculations. To better understand the function of CST a description of the FDTD is presented.

FDTD methods define the computational space based on a grid, known as Yee cell [18]. The fields are defined at each point along the 3D grid at a specific point in time. Figure 2.7 is a representation of how the fields are defined within a Yee cell at a given snapshot in time. Observing maxwell's equations,

$$\nabla \times \vec{E} = -\mu \frac{\partial \vec{H}}{\partial t} \quad (2.19)$$

$$\nabla \times \vec{H} = \epsilon \frac{\partial \vec{E}}{\partial t}, \quad (2.20)$$

and the field definition in Figure 2.7, it can be seen that six coupled partial differential equations are developed by observing each of the independent directions of the magnetic and electric field. In taking the difference in the electric field from one location on the grid to the next and setting that equal to the magnetic field over the time difference between the two locations the difference equation is established. Solving for the magnetic field at the next step in time is done based on the past field definition of E_x , E_z , and H_x . The calculation of future fields is known as the update equation. In applying the difference equation for all vector directions of the electric and magnetic field provide the update equation for \vec{E} and \vec{H} . Once the fields at that point are defined the process begins again based on the

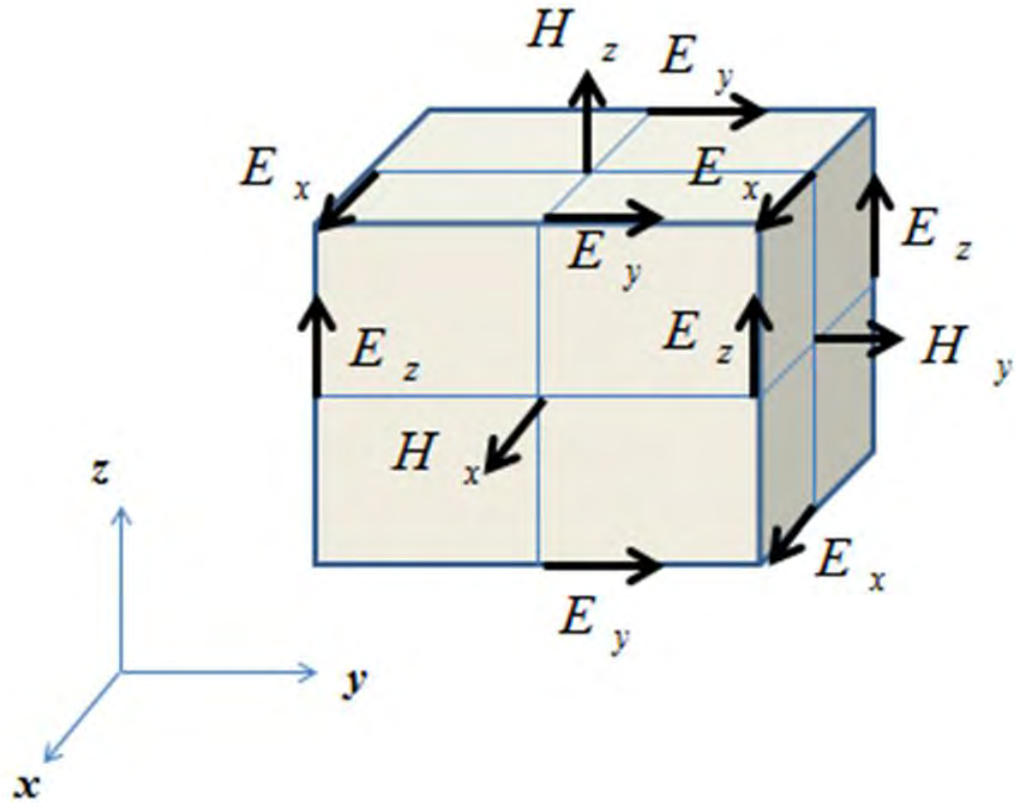


Figure 2.7: Field definition at each location on a Yee Cell

previously calculation field definitions. Refer to [18] for a full description of FDTD field computation. The size of each grid step is determined by how detailed the object parts need to be defined. For example, in order to capture a curved surface, such as a half loop, the grid points defining the surface must be close together, or the approximation will not capture the exact curvature. In order to capture the continuous curve with discrete points in space an appropriate amount of detail is required in the mesh. For example, if the simulated object is one inch in length and the mesh step is greater than one inch, that feature will not be defined in the computational space.

The final step for defining an FDTD problem is the boundary conditions of the Yee cell. The boundary condition defined for all CST simulations is a perfectly matched

layer (PML) boundary. A PML boundary is used to eliminate as many reflections as possible at all incident angles at the Yee cell boundary. This will reduce computation errors based on the reflection caused by a finite computational space. For example, in defining an antenna pattern the fields radiate in free space, which is considered infinite. When the problem is bounded through FDTD the boundary condition must emulate free space or the field definition will be impacted by the bounded calculation. The boundary is based solely on absorption of the fields; therefore, it is crucial that the material properties of the medium within the Yee cell match the properties of the boundary [18]. Within CST, the constitutive parameters of the Yee cell are considered, and the boundary is automatically calculated to minimize any possible reflections.

2.5 Array Theory

To understand the effects of multiple sensor clusters used in an airborne HFDF array, basic array theory and its application to this research is required. Consider a linear array of isotropic radiators summed to one array output. When the array is illuminated by a plane wave, the phase of in incident wave in respect to the phase front of the wave is different for each individual element as shown in Figure 2.8. The amount of phase difference is based on the element spacing, d , shown in Figure 2.8 [16]. Due to the phase difference in the incident signal on the array the signals will not coherently sum and will now cause amplitude variations based on the direction of the incident wave. For direction finding applications a narrow beamwidth is required to define the exact AOA of a transmitting signal. Beamwidth for a linear array is defined by,

$$\theta = \frac{\lambda}{L} \quad (2.21)$$

where,

- λ - wavelength,

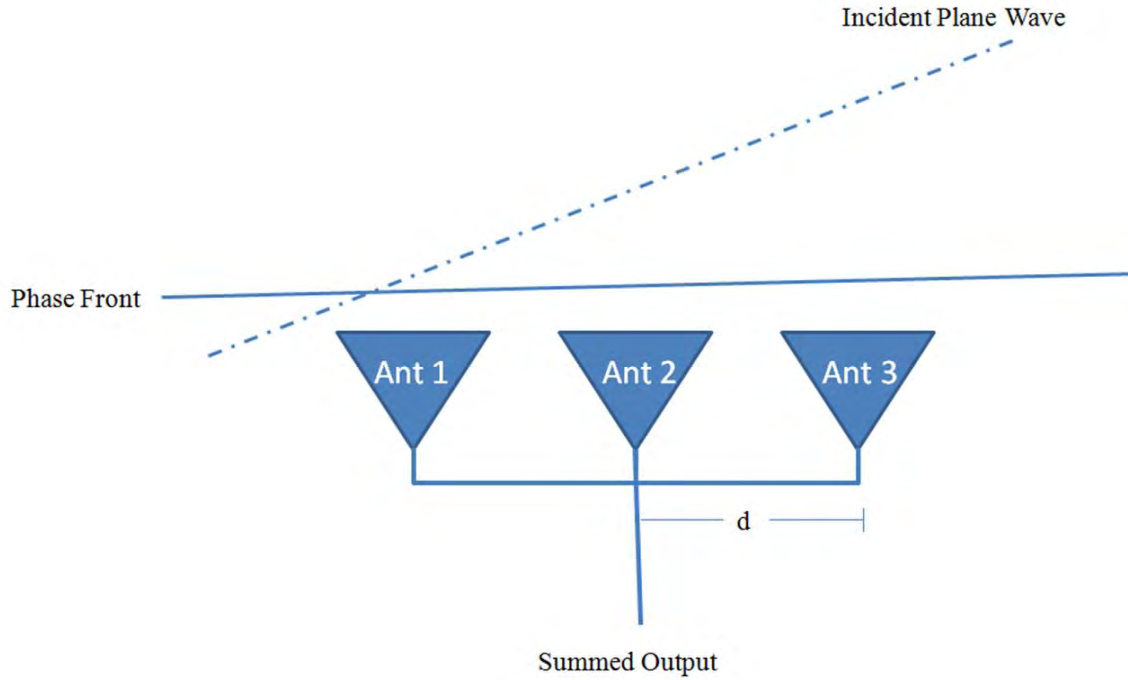


Figure 2.8: Phase relationship for incident plane wave on a linear array

- L - maximum extent of array [16].

Based on equation (2.21), the larger the array the more narrow the beamwidth. For HFDF applications this immediately becomes a concern because of the long wavelength; therefore, maximizing the extent of the airborne array will be paramount to achieving a direction finding capability. In addition to beamwidth, elimination of grating lobes (additional main lobes) is important to creating functional direction finding (DF) array. Grating lobes occur when minimum spacing between individual elements is greater than $\frac{\lambda}{2}$ away from the next adjacent element [16]. Considerations for beamwidth and grating lobe reduction must be included in the airborne HFDF design.

Basic linear array concepts can be applied to the HFDF array, but in many ways this array is different. The array will function much more as a planar array of non-uniform spacing and therefore the exact estimation of the pattern is not as easily accomplished.

Additionally, array theory makes the assumption that all array elements are isotropic radiators; therefore, the effect of the array design defines the operation of the array, as shown by,

$$AF = \sum_{n=1}^N e^{j(n-1)(\vec{k} \cdot \vec{r} + \beta)} \quad (2.22)$$

where,

- \vec{k} - vector from the array origin to an observation point,
- \vec{r} - vector from the array origin an individual element,
- β - phase excitation [5].

The array factor (AF) is defined by a summation of the phase difference between the elements and any additional phase applied to the individual elements. Due to the electrically small radiators, it is expected that the individual elements will function as isotropic radiators. Based on the long wavelengths in the HF band the effects of diffraction, caused by a finite ground plane, on the individual element patterns will require evaluation of each of the elements on a representative aircraft; therefore, the array factor will only give an approximation to the actual array pattern. To define an initial array for HFDF, the element factors of the individual elements must be summed to characterize the array pattern.

2.6 Conclusion

The governing theory and an analysis current research been presented for the development of this research effort. Though HFDF has seen limited investigation, based on results by Hardin continued research is warranted [2]. With the basis of coupling, B-dot functionality, array design, computational electromagnetic methods and array design, determining the radiation efficiency and array capabilities of a B-dot sensor based direction finding system can be accomplished.

III. Methodology

In order to define the capabilities and functionality of the MGL-S8A B-dot sensor for use in an airborne HFDF array an understanding of the sensor sensitivity in the HF frequency band must be determined. To show that previous research is representative of operational situations a signal analysis is accomplished. Evaluating the sensor radiation is completed through the use of CST Microwave Studio to create the simulated response of the individual sensor, sensor cluster, and the interactions of multiple sensors on the airframe that defines the array pattern. Additionally, an outdoor sensor cluster detection test is shown for comparison to simulation. Finally, a comparison of the B-dot sensor to the structurally integrated monopole design is completed to determine if the B-dot sensor is an improvement over the monopole feed design.

3.1 Incident Power Analysis

Magnetic field strength versus aircraft range is compared to Captain Ryan Hardin's characterization of a B-Dot magnetic field sensor in order verify that the laboratory test results represent an operational scenario [2]. Only data from the zero-degree orientation, shown in Figure 3.7 in Hardin's research, is discussed due to maximized signal returns from the sensor; however, additional sensor characterization data on 45 and 90-degree orientations can be found in Hardin's research [2]. The HF frequency band is allocated by the Federal Communications Commission (FCC) and international organizations. The federal and international licensing makes it possible to pinpoint possible signals of interest in the 2-32 MHz band. In order to understand the magnetic flux density, four of the major signal sources within the 2-32 MHz band are analyzed. Table 1.1 provides the list of signals used in determining field strength levels. All stations are federally or internationally

licensed [9, 19–21]. This mathematical analysis makes some assumptions that are required to validate the results. All assumptions are listed below:

- A single data collection is completed. This does not consider possible coherent processing of multiple collections from each transmitter.
- Atmospheric losses are ignored. Due to the free space propagation presented in an airborne direction finding scenario this assumption does not greatly reduce the accuracy of the solution.
- All transmitter sites are considered to be isotropic radiators with a gain of one. In addition, FCC power levels are outlined as effective radiated power which takes into account antenna gain.

Four major transmitter types were analyzed using equations (2.12) and (2.16) to determine the signal strength in Tesla with varying range based on signal type. The ranges calculated are slant ranges.

The four previously listed signals of interest represent a wide frequency and power sample from HF transmitters. Table 3.1 shows the test results for the B-dot sensor using the TEM cell [2]. Based on Hardin's findings, it can be seen that an incident field of 6.5 nT produces an adequate signal to noise ratio in order to distinguish the signal from existing noise. The issue with the results shown is that for an operational receiver -114 dBm noise floor is approximately 7 dB lower than expected receiver performance, therefore the SNR is higher than what would be expected for an operational application. In addition, the SNR is based on a 45 second collection averaged by a 10 ms coherent integration time [2].

The mathematical analysis determines that the ranges for a single detection are practically zero; therefore, pulse integration is required in order to achieve a relevant detection range. Integration of the collected signal can be done in order to reduce the

Table 3.1: MGL-S8A measured power out with 6.5 nT input and 10 ms coherent integration time [2]

Freq (MHz)	Power Out (dBm)	Noise (dBm)	SNR (dB)
4	-99.84	-114.96	15.12
7	-95.48	-114.96	19.48
15	-89.57	-114.96	25.39
21	-86.53	-114.96	28.43

noise floor and increase SNR and detection range [17]. Applying the same integration as used in the laboratory test the detection ranges are shown in Table 3.2.

Table 3.2: Range at which 6.5 nT signal levels are reached based on transmitter signals of interest and laboratory test integration time

Transmitter Type	Frequency (MHz)	Range (km) at 6.5nT
International Broadcast 500 kW	6.2	133.3
International Broadcast 100 kW	13.57	59.6
International Broadcast 25 kW	21.45	29.8
HF-GCS 4 kW	11.175	11.9
Standard Time and Frequency 10 kW	5	18.8
International Distress 160 W	16.8	2.4

As the data show, this process would work best on a continuous transmission signal, such as the standard time and frequency or broadcast station based on the assumptions that common signals cannot change over the collection time. The analysis also shows though relevant detection ranges can be achieved the previous characterization might have been more complete if lower signal levels were used. The results of the HF signal analysis limits the DF possibilities of this system to high power continuous transmissions in order to achieve detectable power levels at the aircraft.

3.2 Computational Sensor Characterization

3.2.1 Single Sensor Design.

The MGL-S8A B-dot sensor is designed in CST Microwave Studio in order to understand the sensor effectiveness in the 2-32 MHz band. Prodyn has provided expected radiation efficiency for the sensor but their characterization is accomplished at 5 GHz. Figure 3.1 is the design of the B-dot sensor in CST Microwave Studio. The

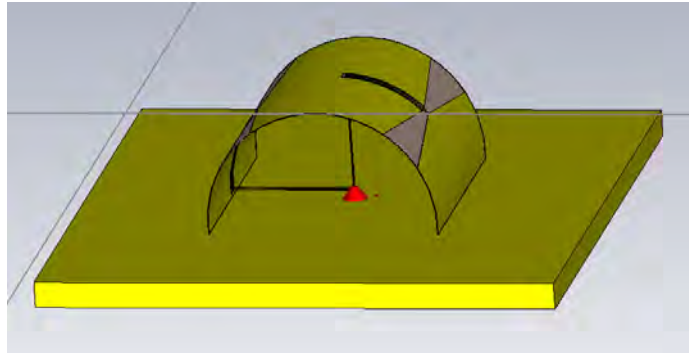


Figure 3.1: B-dot sensor design in CST Microwave Studio

sensor is designed using the sensor specifications listed in Table 3.3. The above

Table 3.3: MGL-S8A B-dot sensor CST design dimensions

Half Loop Radius	3.6 mm
Length of Loop	7.2 mm
Half Loop Material Thickness	.00356 mm
Gap Spacing	.21 - 1.71 mm
Ground Plane Size	25.4 x 25.4 mm
Ground Plane Thickness	.0127 mm

specifications are based on the original sensor design by the Air Force Weapons Laboratory [22]. CST Microwave Studio has the capability to design systems with the specific constitutive parameters of the metals used in the sensor design. Simulation of actual design

specifications leads to a more accurate estimation of actual performance versus theoretical approximation. Copper is used in simulation of the loop and a silicon dielectric material is used for the gap design.

In order to determine the radiation efficiency of the sensor, an impulse signal is introduced into a $50\ \Omega$ port on the sensor and the radiation pattern is determined from 2-32 MHz with steps of 1 MHz. The $50\ \Omega$ port is used to simulate the SMA connector on the sensor. The impulse signal is a Gaussian excitation from 0-32 MHz. Though it is not required to analyze the sensor below 2 MHz, simulation times are reduced by using a Gaussian pulse compared to Gaussian pulse combined with a sine wave required for 2-32 MHz excitation.

To accurately evaluate the sensor performance in the farfield, the simulations must be designed to evaluate the sensor with the correct boundaries and constitutive parameters surrounding the sensor. To measure the farfield, open boundary conditions are used in all directions around the sensor excluding at the base of the sensor. The open boundary condition has space added between the sensor and the boundary in order to measure the farfield because the monitors must be placed at a distance far enough away to be considered in the farfield. Due to the long wavelengths, the large boundary box increases the computational space of the analysis. The bottom of the sensor is simulated with an electric field boundary in order to simulate an infinite PEC ground plane. The electric field boundary condition is used for initial characterization of the sensor, full understanding of the sensor's farfield in an airborne HFDF application requires the aircraft to be simulated as the ground plane because it cannot be assumed to be infinite at HF wavelengths.

Quantifying the effects of the impulse response requires the use of a hexahedral mesh to evaluate the radiation across the surface of the sensor. The mesh defines the spatial step for evaluating the model which effects the farfield of the signal excitation on a small facet of the antenna utilizing the FDTD method discussed in chapter 2. Due to the small curvature

of the sensor and small conducting wires, the mesh must be concentrated over the detailed areas of the sensor to accurately define the electromagnetic response. Computational runtime increases exponentially with number of mesh cells; therefore, optimization of the mesh cells used to define the model is required. Local mesh grids are applied to the sensor that allow for minimized meshing over larger flat areas on the sensor. Based on the fact that the boundary box is large (minimum of 38 m across) and the mesh is defined across the entire boundary, much of the computation is a calculation of the field interactions in free space. The local mesh design for this simulation is defined in Table 3.4.

Table 3.4: Local mesh properties for B-dot sensor characterization

Part of Sensor	Δx	Δy	Δz
Ground Plane	2 mm	2 mm	.2 mm
Loop	.05 mm	.05 mm	.07 mm
Gap Dielectric	.1 mm	.1 mm	.1 mm
Transmission Line	.02 mm	.05 mm	.05 mm
Transmission Dielectric	.02 mm	.05 mm	.05 mm

With the above mesh grid design, CST Microwave Studio can now compute the radiation efficiency of the single sensor. With the above settings a total of 6.7 million mesh cells are produced for this analysis. Due to the long computation time for this number of mesh cells using a Tesla 2070 graphics processing unit (GPU) allows for efficient parallel processing. With the use of the GPU the expected computation time is 96 hours. Simulations without a GPU could take up to 2 weeks for a single simulation. Based on the single sensor the four-sensor cluster can now be designed.

3.2.2 Sensor Cluster Design.

To define the sensor cluster an analysis of the radiation efficiency for a simple loop antenna is used to consider coupling and compare a single sensor to multiple sensors for improved radiation efficiency in the HF band.

The radiation efficiency of a loop defines how well the sensor will function in the HF frequency band. The specifications listed in Table 3.3 are applied to equations (2.9), (2.10) and (2.11). Figure 3.2 is a comparison of four B-dot approximated loops versus a single approximated loop. As expected the increase from a single sensor to four-sensors

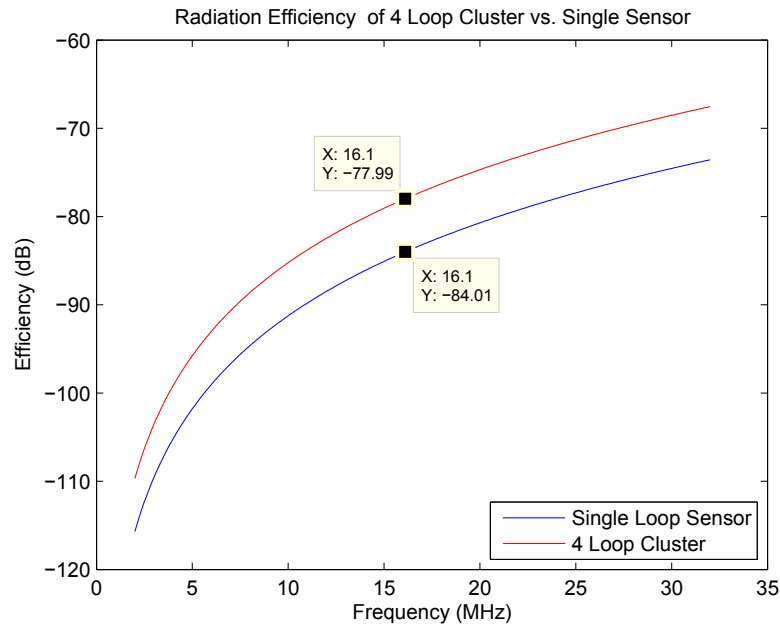


Figure 3.2: Comparison of 4 sensor cluster of B-dot approximated loop vs. single approximated loop

should be 6 dB due to the effect of the summation of the four signals of equal phase. Four sensors increase the power four times while still utilizing a small area on the aircraft. The cluster design is built on the assumption that the phase of the incident wave on each of the individual sensors is equal. Due to the long wavelength this phase assumption is valid

and will be shown in the four-sensor simulation. Though adding additional sensors would continue to increase overall efficiency the cost of each sensor cluster would rise making the sensor not useful for a low cost option. In addition to phase considerations the mutual coupling between each of the loops must be minimal in order to attain a 6 dB increase using a four-sensor cluster.

Mutual coupling is related to the radiation efficiency of each of the individual loops and how the loops are configured in the sensor cluster. Figure 3.3 is a plot of the effect of a reradiated field from a closely located sensor assuming the incident field is at 0 dBm. The

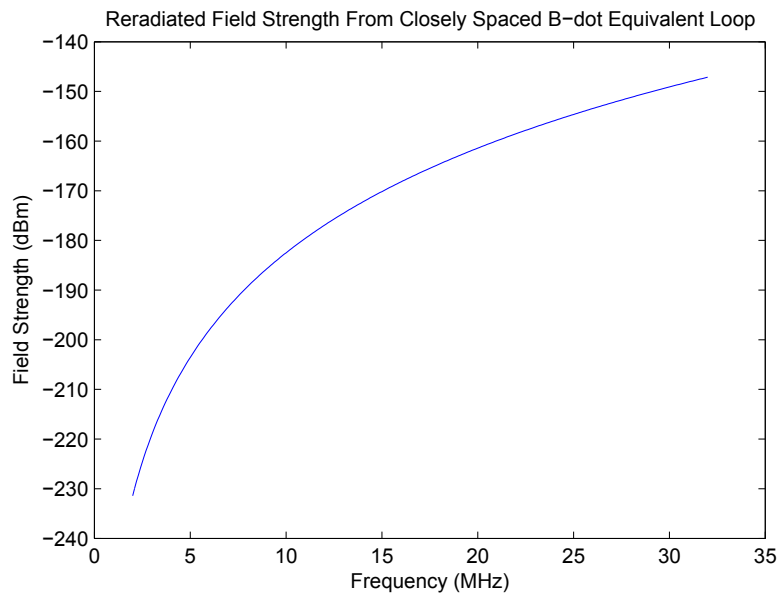


Figure 3.3: Field strength of closely spaced equivalent loop based on 0 dBm incident signal

minimum difference between the reradiated field and the incident field is 147 dB; therefore, the coupling between the sensors does not have to be considered when deciding the layout of the four-sensor cluster. Based on reduction in phase difference and minimizing the impact of mounting the sensors on the aircraft, the sensor cluster design shown in Figure 3.4 is used.



Figure 3.4: Simulated four sensor cluster

Simulation for initial characterization of the sensor cluster has the same boundary conditions and mesh grid definition. To simulate a summation of the sensors each sensor is excited independently and the combined farfield is measured. Based on the equation used by CST Microwave Studio defining radiation efficiency, equation (3.1), it is expected that if the simulation matches the assumptions of limited phase difference and insignificant coupling the radiation efficiency should increase by 6 dB.

$$e_{rad} = \frac{PowerOut}{PowerIn} \quad (3.1)$$

where, *PowerOut* is the combined radiated power and *PowerIn* is the excitation power for each sensor. Based on the use of four excitations the expected runtime is now 384 hours or 16 days; therefore, parallel processing is crucial to achieving results within a reasonable time.

3.2.3 *B-dot Cluster Array.*

Due to the inability to treat the aircraft as an infinite ground plane, a simulated RC-135 is designed in CST and sensors are placed throughout the aircraft in order to evaluate an initial airborne array capability. The RC-135 design is based on the specifications provided

in Appendix ?? [23]. The Boeing 707 specification sheet is utilized because the Boeing 707 airframe is used in the 135 variants [24]. Though classical phased array processing does not hold due to the effects of diffraction, observing the expected shape of the array factor gives insight into the expected performance of the sensors simulated on the aircraft.

As a starting point for an array design a total of eight sensor clusters will be used on the simulated aircraft. The placement of these clusters are based on elimination of grating lobes and maximizing the extent of the array in order to minimize beamwidth over a large frequency band. Figure 3.5 is the simulated airborne array design. A simplistic model

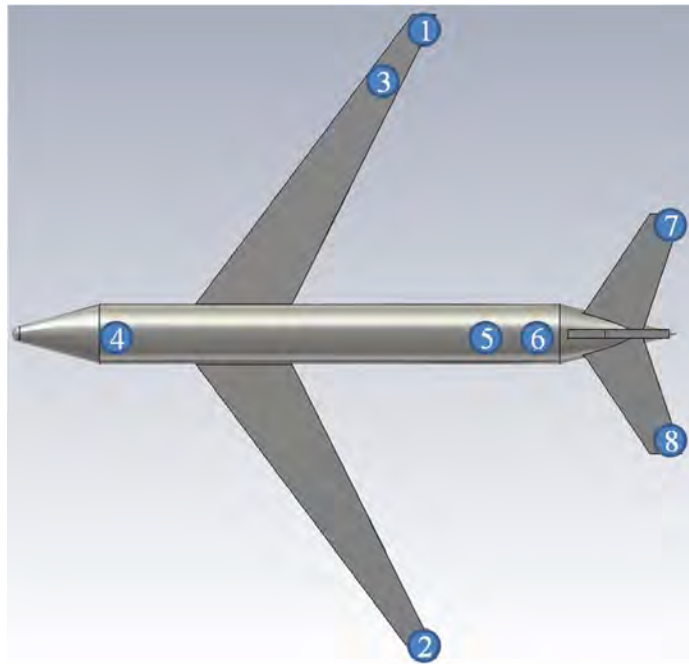


Figure 3.5: Airborne HFDF B-dot sensor cluster array locations and simulated RC-135

is used for the RC-135 due to the increased simulation time of using a detailed model. This model still captures the effects of diffraction and array spacing while minimizing computational time spent on the meshing of the model.

Observing the approximate array functionality can be done by looking at the array factor of the design presented in Figure 3.5. The array factor only shows the expected

shaping based on the phase information in the array element spacing but the effects of the individual patterns are not understood; therefore, the actual array pattern is not defined by the array factor. It can also serve as a sanity check for the CST output. Utilizing Equation (2.22) the array factor is calculated from 2-32 MHz based on the 3D geometry of the simulated RC-135. Figure 3.6 shows the XZ and YZ planar cuts of the array factor. It

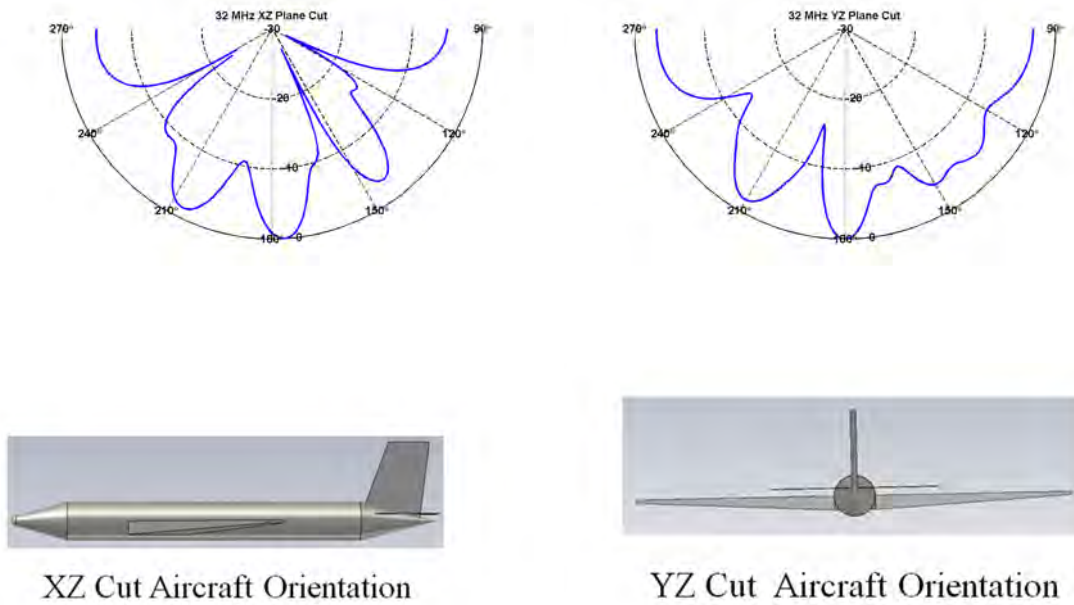


Figure 3.6: Plane cuts of HFDF array factor at 32 MHz

is observed that significant shaping can be accomplished at this frequency and with some reduction in sidelobe levels the directionality of the main be is vastly improved. Choosing a lower frequency and observing the overall shape will glean additional information on the bandwidth of the array. Figure 3.7 shows a much broader main beam with high sidelobe levels. This is less optimum for DF application but does show enough phase difference exists that an improvement is seen over an isotropic radiator. Analyzing the array factor at 10 MHz shows the loss of any significant shaping due to the array factor, Figure 3.8.

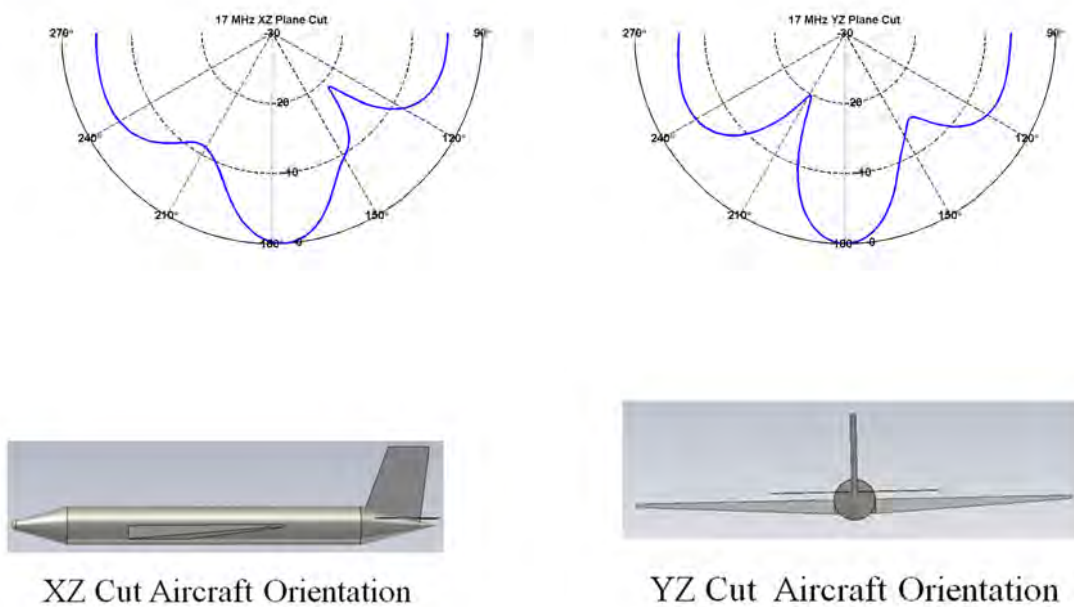


Figure 3.7: Plane cuts of HFDF array factor at 17 MHz

This implies that when analyzing the farfield for the array simulated in CST is expected that little to no shaping effect will be present at or below 10 MHz due to limited phase differences.

Based on the general understanding of the functionality of the HFDF array the individual sensors must be simulated in CST Microwave Studio. Utilizing the parallel processing capability eight individual sensor simulation are run concurrently on the RC-135 model as shown in Figure 3.5 to define the farfield pattern of the entire array. Only single sensors are used even though the actual design requires the use of sensor clusters in order to reduce simulation time. Using a single sensor is valid because the cluster is only used to increase sensitivity it will not add additional phase information because of the close spacing. Eight individual simulations are run because simulation of all sensors in one model is not possible due to memory constraints of the GPU. The output of each of the eight patterns will then be summed together in order to define the farfield of the entire

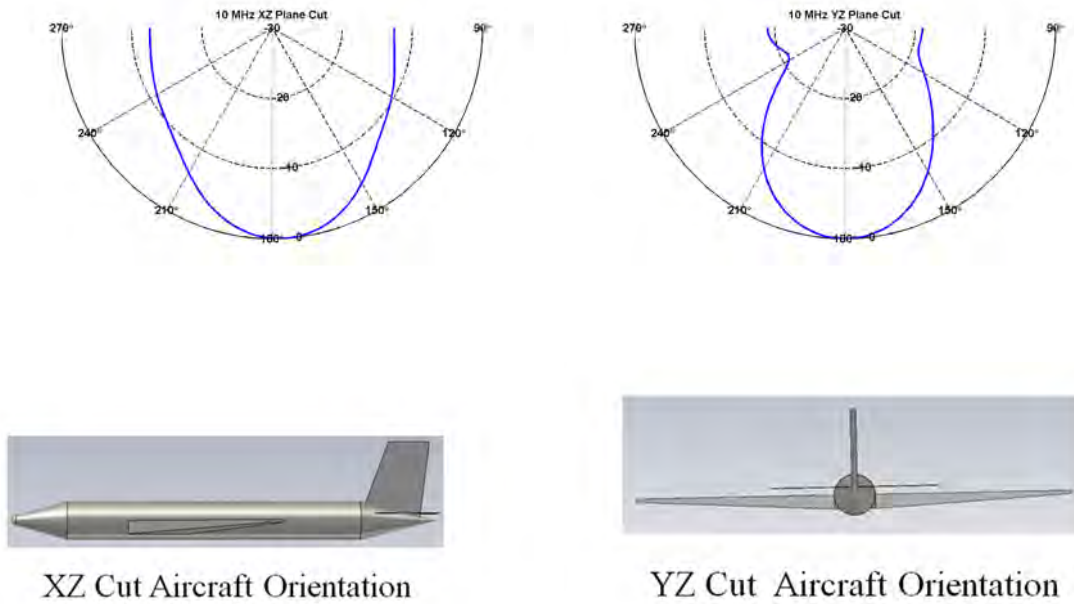


Figure 3.8: Plane cuts of HFDF array factor at 10 MHz

array. This summation is a valid representation of the array, because all simulations are done using the RC-135 with the same global coordinate system.

With the function of the eight sensor array quantified, two additional sensors will be added to reduce the sidelobe levels of the HFDF array. The two additional sensors locations are determined by the array research accomplished by BerrieHill [4]. The SI monopoles are placed based on the highest concentration of current for a given mode. In order to attain the most efficiency possible out of the B-dot sensors placing additional sensors in locations on the aircraft that have already been defined as high areas of field strength will allow for the most improvement of array functionality. The location is chosen by also factoring in the phase difference between each of the sensors. Based on these two considerations the locations of the additional sensors are shown in Figure 3.9. Using these sensor locations add phase difference in two dimensions of the array that can reduce sidelobe contributions, especially at higher frequencies [25].

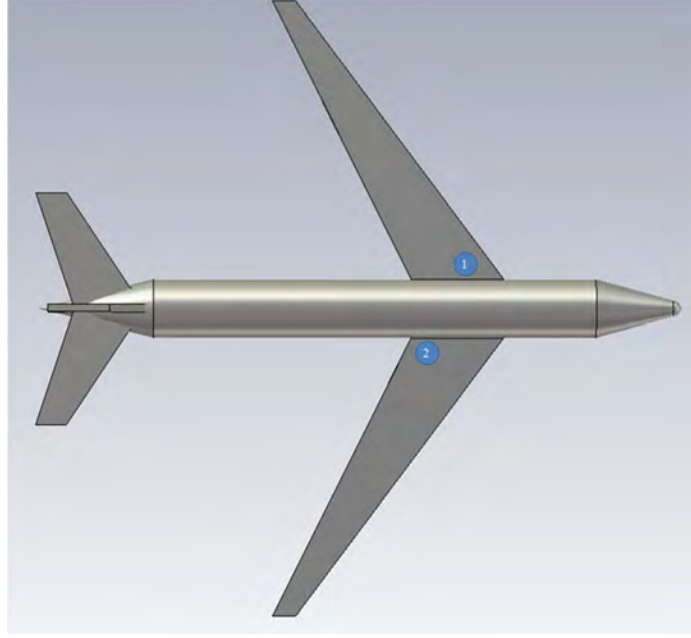


Figure 3.9: Additional simulated sensor location for reduction in HFDF array sidelobes.

3.3 Non-Uniform Phased Array

To fully analyze the direction finding capability of the eight and ten-element arrays in MATLAB the addition of applying varying phase shifts to each element allows for the steering of the main beam of the array to a specified azimuth and elevation. This capability is possible within CST Microwave Studio but requires the simulation of the entire array which is not achievable due to limited GPU memory in the computers provided in the AFIT Low Observables Radar and Electromagnetics (LORE) computing lab. In order to achieve varying phases on each element of the array the field definitions for each sensor must be shifted within CST and then imported into MATLAB. After importing the into MATLAB the physical phase shift is defined by,

$$E.F.e^{-j\vec{k}\cdot\vec{r}+\beta} \quad (3.2)$$

where \vec{r} points from the origin of the global coordinate system to each sensor location, β is the phase added to that sensor and E.F. is the element factor which is the pattern at

that sensor location. To determine the direction finding ability in a given direction the dot product must be defined to maximize the beam in a specified direction. Evaluating the dot product for a given scan angle produces,

$$E.F.[x_n \sin(\phi - \phi_s) \sin(\theta - \theta_s) + y_n \sin(\phi - \phi_s) \sin(\theta - \theta_s) + z_n \cos(\theta - \theta_s)] \quad (3.3)$$

where,

- θ_s - steering angle in θ ,
- ϕ_s - steering angle in ϕ ,
- x_n - x location of sensor number n,
- y_n - y location of sensor number n,
- z_n - z location of sensor number n.

Equation (3.3) is a combination of the analysis of performed by [16] and [5] to incorporate beam steering into 3D field analysis. Applying this equation to each element location and then summing the fields defines the array with the main beam steered to angle (ϕ_s, θ_s) . With the beam steered the pattern can be correlated to other directions to establish the direction finding capability at the specified azimuth and elevation.

3.4 MGL-S8A B-dot Field Testing

To validate all previous computational evaluations of the B-dot sensor cluster a field test is completed based on sensing the electromagnetic environment with the B-dot cluster compared to detections with a VHF vertical antenna. To compare the equal polarizations, the loops will be placed with the B-field polarization horizontal and the VHF antenna vertical. The cross polarization of the sensor and truth antenna is due to the fact that the VHF antenna is accomplishing electric field sensing of vertical polarization therefore the magnetic field is horizontal.

3.4.1 Required Materials.

Accomplishment of field test requires the following items:

- 3286S HF receiver
- hardware key
- receiver power cable
- Buddipole (VHF vertical)
- four 2.5 ft SMA cables
- four-port power combine
- doughnut ground plane
- sensor ground plane plate
- two marine batteries
- saw horses
- tie wraps.
- laptop for operation of Agilent 3286S
- firewire cable
- four 50 Ω loads
- Buddipole RG-8 coax
- one 10 ft. SMA cable
- equipment cart
- four MGL-S8A B-dot sensors
- power inverter
- four SMA barrel connectors
- magnetic tape

3.4.2 Equipment Fabrication.

To adequately field test the B-dot sensor cluster a ground plane is fabricated for mounting the sensors to the pre-existing doughnut ground plane. Figure 3.10 depicts the ground plane mount fabricated for field test. The ground plane is fabricated out of 0.0625 inch aluminum and attached to the doughnut ground plane using metallic tape in order to reduce diffraction effects caused by the ground plane. Holes in the ground plane are cut for female SMA connectors on B-dot sensors. The doughnut ground plane without the mounting plate is shown in Figure 3.11.

3.4.3 Impedance Analysis.

To understand the expected results of the field test the system noise, cabling, and loss need to be analyzed across the entire frequency range. The four port summer and five 50 Ω cables are connected to a signal generator and then run into a digital oscilloscope in order

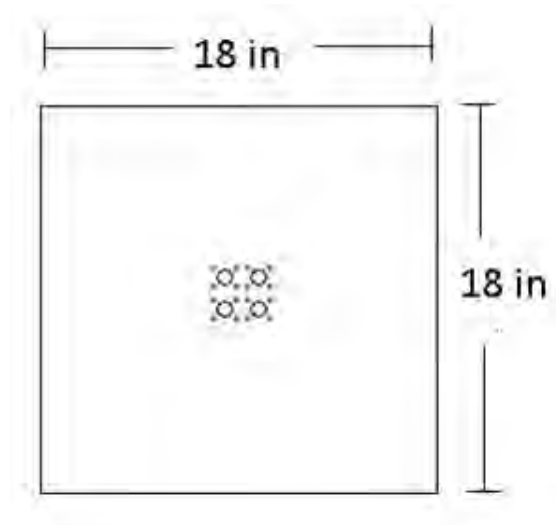


Figure 3.10: 18" X 18" ground plane mount for doughnut ground plane



Figure 3.11: Doughnut ground plane used for B-dot cluster test.

to show the loss with relation to frequency. Based on the insertion loss of the summer and the loss of the coax cables, the expected signal loss is less than 3 dB.

3.4.4 Test Layout.

The data collection is completed by placing the doughnut ground plane on two plastic saw horses. Plastic saw horses allow for reduction in interference between ground plane and mounting system. Though this detection height is not optimum, it is required for signal collection due to the cumbersome ground plane. The output of the summer is connected to channel 1 of the receiver. The VHF vertical antenna is a VHF Buddipole. The Versitac vertical variant of the Buddipole is used to tune the antenna to 50 MHz with a near isotropic radiation pattern. The vertical antenna is connected to Channel 2 of the receiver with a 50 ft RG-8 50 Ω cable. Both channels are collected simultaneously. The noise characterization is completed in a single set of collections with sensors and Buddipole disconnected and the cables terminated for noise to determine cabling and internal receiver noise levels. The laptop is connected to the receiver via a firewire cable for receiver control. The receiver threshold margin is set to zero dBm in order to collect all received signals. Due to the inefficiency of the B-dot sensor, the margin is not set higher to reduce data size therefore data analysis is difficult due to the amount of data collected.

3.4.5 Signal Collection.

To cover 2-32 MHz frequency range four collections must be completed with a receiver bandwidth of 8 MHz. A 20-second collection is taken for all data in order to evaluate expected intermittent signals. A collection is taken to establish a noise baseline to validate signal to noise ratio. The noise data is collected in the exact configuration as the sensor and VHF vertical antenna, because the signals observed from the B-dot sensor cluster may be due to the cabling and summer because of the poor radiation efficiency of the B-dot sensors at HF frequencies. Each of the four cables are terminated with 50 Ω loads. Table 3.5 is a list of all completed collections.

Table 3.5: Sensor field test runcard

Run	Center Frequency	Ground Plane Orientation	Collection Type
1	6 MHz	Horizontal	Noise
2	14 MHz	Horizontal	Noise
3	22 MHz	Horizontal	Noise
4	30 MHz	Horizontal	Noise
5	6 MHz	Horizontal	Sensors and Truth
6	14 MHz	Horizontal	Sensors and Truth
7	22 MHz	Horizontal	Sensors and Truth
8	30 MHz	Horizontal	Sensors and Truth

3.4.6 *Signal Analysis.*

To determine if signals were received by the B-dot sensor cluster, correlation is used to find common signals in the vertical antenna and the B-dot sensor cluster collection. Correlation is accomplished between all data collections, noise, B-dot sensor, and vertical antenna. The correlation validates that the common signals found in the B-dot and vertical antenna. Correlations are not based on the noise from the receiver during the collection. The correlation will be done by taking the fast fourier transform (FFT) of the collected data and then doing an element-by-element multiply of the two signals that are being correlated.

Due to the inefficiencies of the sensors it is expected that collection integration will be required in order to reduce the noise floor. Sixteen integrations of the data will be accomplished by separating the data into 16 collections, an integration time of 1.25 seconds, taking a separate FFT of each collection and then doing an element-by-element multiplication of the each collection in the frequency domain. A correlation is then be accomplished on the integrated data collection to determine if integration improved detection of signals for the B-dot sensor. Based on an analysis of the dominant signals

within the integrated and non-integrated frequency spectrum and correlation, the ability to detect signals in the HF band is determined.

3.5 Comparison of B-dot Sensor to BerrieHill Structurally Integrated Monopole Feeds

The B-dot sensor performance in an airborne array is now understood; therefore, it must be compared to the performance of other research areas in airborne HF direction finding. The structurally integrated monopole design is one of the most current research areas in this topic. In order to verify that this sensor is an improvement on the current research capabilities a comparison of the magnitude of the electric field in the farfield is accomplished.

Observing Figure 2.2 it can be seen that 2 of the sensor simulations are located in proximity of the simulated array locations shown in Figure 3.5 [4]. The approach to the design of the array by BerrieHill was accomplished differently then this research effort and due to the long wavelength and the interaction of the HF signals with the airframe only commonly located sensors can be used for this comparison. Figure 3.12 describes the common locations compared. The numbers shown in Figure 3.12 represent the comparison of the B-dot sensor to the BerrieHill SI monopole feed. Based on the comparison of the magnitude of the farfield a determination is made on whether the B-dot sensor or the BerrieHill SI monopole is best for HFDF applications.

3.6 Conclusion

The methods for evaluating the overall performance of the MGL-S8A B-dot sensor are shown. The performance is evaluated through computational and real world evaluation of the sensor. Using the B-dot sensor for an HFDF array is simulated based on the considerations of narrow beamwidth, reduction in sidelobes and elimination of grating lobes. Common sensor locations are compared to define the effectiveness of a MGL-

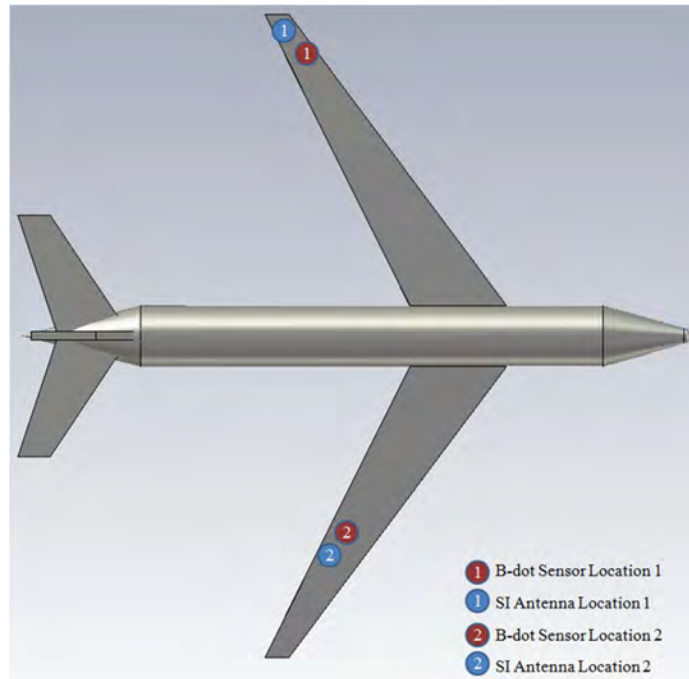


Figure 3.12: Common locations for HFDF array for BerrieHill SI monopole feeds and B-dot Sensors

S8A B-dot sensor versus the BerrieHill SI monopole feed. The results of all sensor assessments must now be analyzed and compared to determine the sensor performance and the effectiveness of the sensor system for direction finding.

IV. Analysis and Results

Chapter IV contains the results and analysis of a single MGL-S8A B-dot sensor and sensor cluster based on radiation efficiency and detection ability in the high frequency (HF) band. Additionally, the CST Microwave Studio simulation for the eight and ten-element arrays are analyzed and compared to determine the pattern improvement of the ten-element array and the directivity of each array. Finally, the BerrieHill structurally integrated (SI) monopole feeds are compared to the MGL-S8A B-dot sensor to determine if the reduced size and the increase in the ability to integrate the sensors into an airframe are worth the reduction in efficiency.

4.1 Single Sensor Characterization

The computational analysis of the B-dot sensor hinges on an accurate design of the sensor in CST Microwave Studio. To evaluate the sensor design, the fields are observed over a PEC (perfect electric conductor) ground plane. The expected radiation pattern of the B-dot sensor over a PEC ground plane is isotropic because the radiating element is much smaller than a wavelength in the HF band. Figures 4.1 and 4.2 are the simulated 3D radiation patterns of a single B-dot sensor. The patterns are isotropic with the field going zero at the ground plane as expected from electromagnetic (EM) theory.

Radiation efficiency is used to validate the sensor design is accurate. Figure 4.3 compares the radiation efficiency of a single simulated B-dot sensor to an equivalent theoretical loop. As expected, the radiation efficiency of a single loop is 8.5 dB less than the multi-gap loop B-dot sensor across all frequencies. The difference is due to the multi-gap design that accomplishes a sum of two detections to improve the detection capability of the sensor. The validation of the sensor design is shown based on the observation of the 3D fields and the radiation efficiency; therefore, the next step is to validate the assumption that

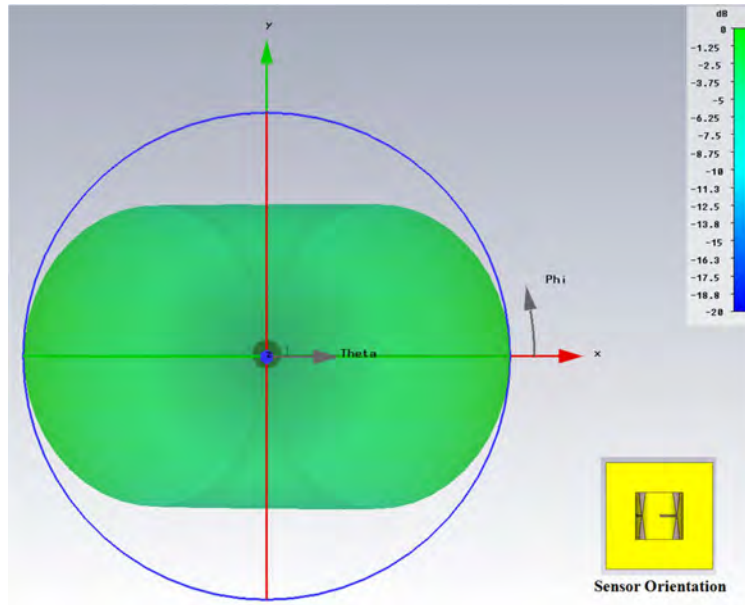


Figure 4.1: Radiation pattern of a single B-dot sensor at 2 MHz simulated in CST Microwave Studio with an infinite PEC ground plane.

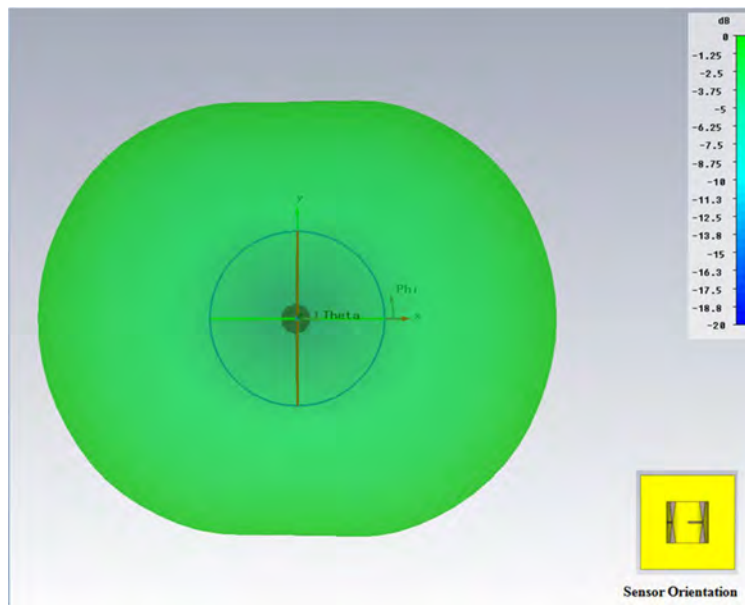


Figure 4.2: Radiation pattern of a single B-dot sensor at 32 MHz simulated in CST Microwave Studio with an infinite PEC ground plane.

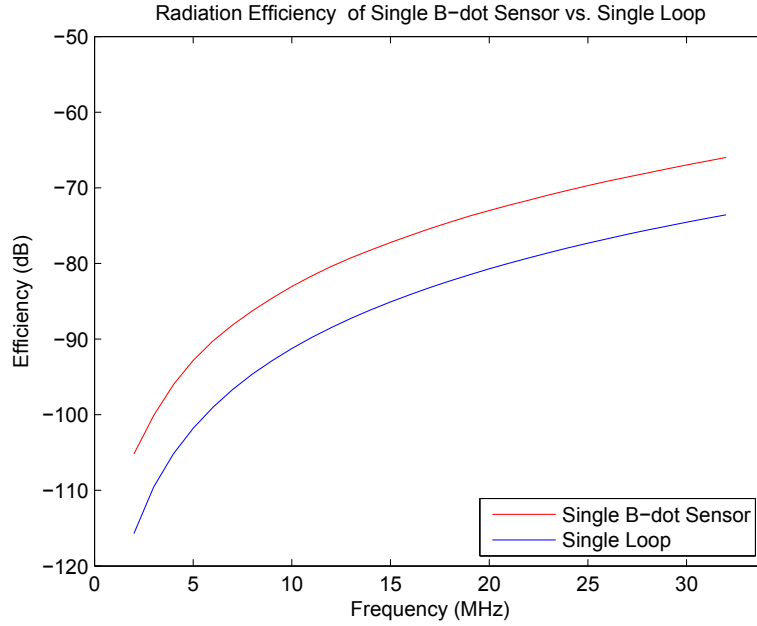


Figure 4.3: Radiation efficiency of single loop versus B-dot sensor from 2-32 MHz.

the four-sensor cluster will increase the radiation efficiency due to the coherent summation of closely spaced sensors by 6 dB.

4.2 Sensor Cluster Characterization

The goal of the sensor cluster is to increase radiation efficiency while still minimizing the impact of installation on an aircraft. Though a larger sensor would also increase radiation efficiency, the impact on the aircraft is increased because the cross section of the sensor is increased causing an impact on aircraft flight due to issues such as aerodynamic heating. In comparison a four-sensor cluster has the same vertical profile as a single MGL-S8A sensor; therefore, aircraft integration is maintained and detection capability is increased. A comparison of the 3D fields and the radiation efficiency describes the impact of the summation of four sensors. Figures 4.4 and 4.5 show that across all frequencies the isotropic pattern is still maintained based on the four sensor cluster. The four-sensor radiation efficiency confirms no additional field interactions, such as mutual coupling, are

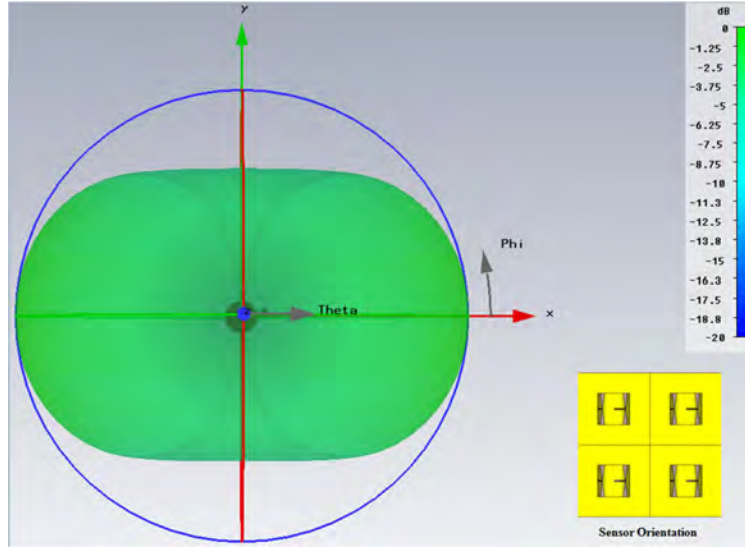


Figure 4.4: Radiation pattern of a B-dot sensor cluster at 2 MHz simulated in CST Microwave Studio with an infinite PEC ground plane.

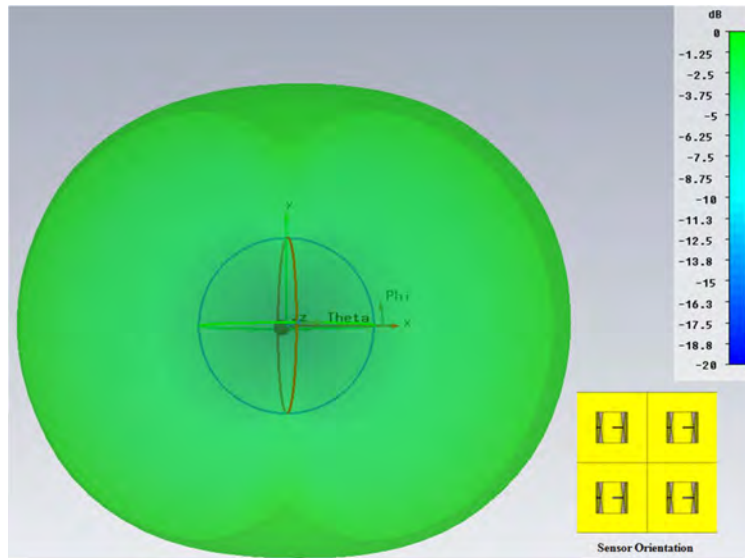


Figure 4.5: Radiation pattern of B-dot sensor cluster at 32 MHz simulated in CST Microwave Studio with an infinite PEC ground plane.

effecting the radiation pattern of the sensor cluster. With no other field interactions, the sum of the four sensors produce an increase in efficiency of 6 dB. Figure 4.6 shows the

radiation efficiency of four theoretical loops compared to the simulated four-sensor cluster.

As shown earlier by the single sensor, the expected difference is between 7.5 and 10.5

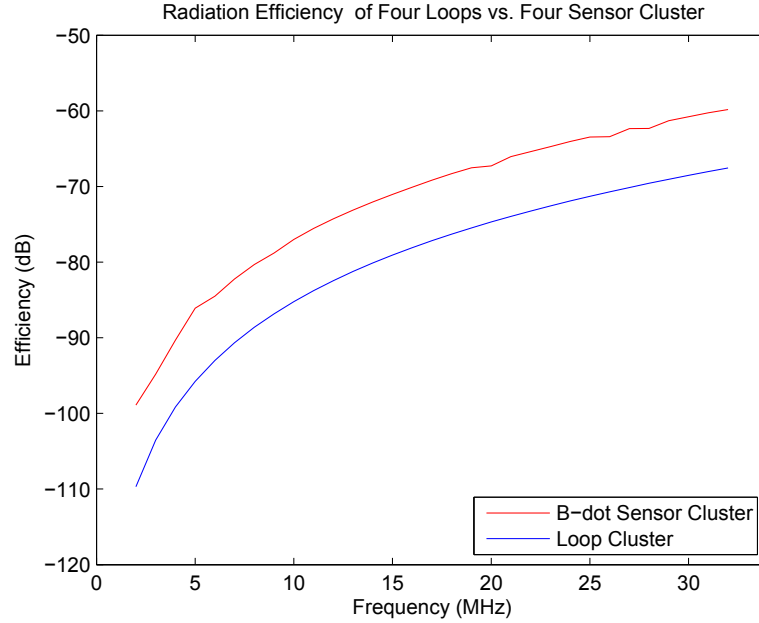


Figure 4.6: Radiation resistance of a four-single loop cluster versus B-dot sensor cluster from 2-32 MHz.

dB, which is maintained in the comparison of four single loops to the four-sensor cluster. Because the difference is maintained the interactions of the loops are not expected to affect the summation of the fields detected by each element of the sensor cluster. Figure 4.7 is the comparison of the single simulated sensor to the sensor cluster. The differences in the simulation verify that the closely spaced loops increase the radiation efficiency by 6 dB across all frequencies.

The diffraction effects from the finite aircraft ground plane perturb the isotropic pattern of the sensors. The more isotropic the pattern the better for a direction finding array because the individual sensors can detect a signal in all directions. For this reason the observation of the aircraft coverage validates that the eight-sensor array provides adequate detection capability. Figure 4.8 is the 3D plot of the coverage area of all sensors. The image in the

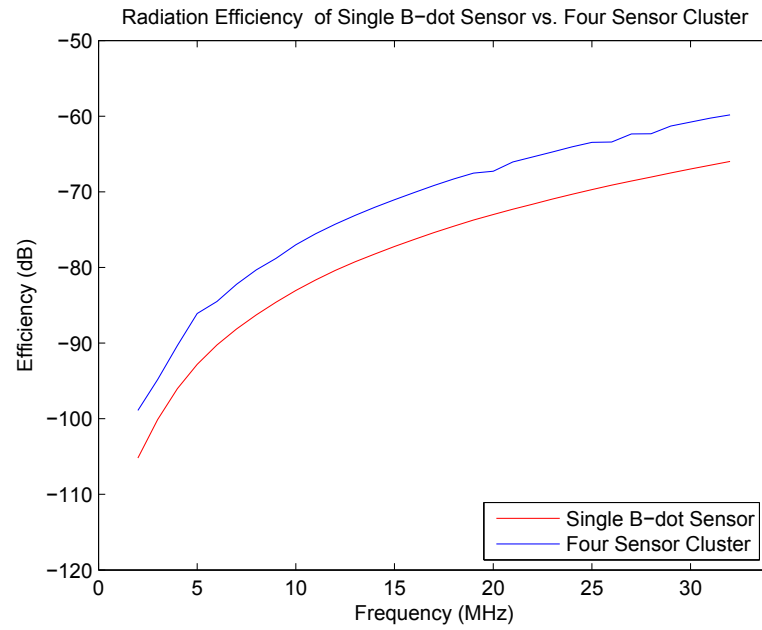


Figure 4.7: Radiation resistance of single B-dot sensor versus B-dot sensor cluster from 2-32 MHz.

middle of the pattern is used to describe the orientation of the aircraft in the 3D field. The

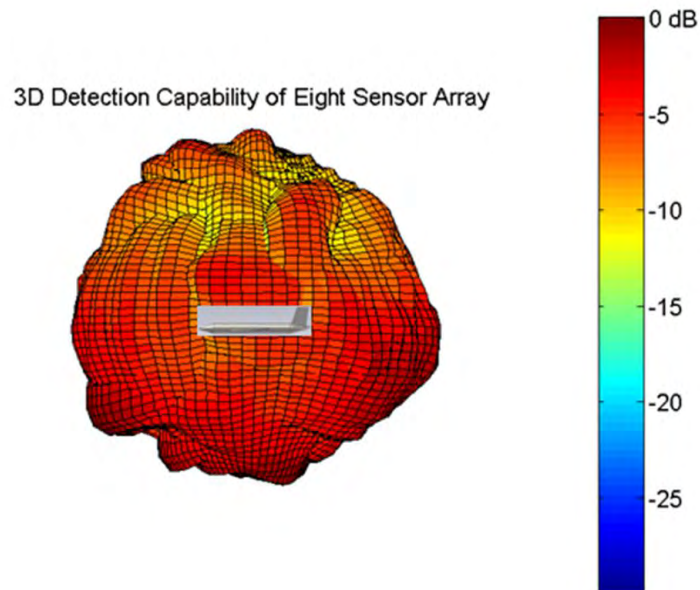


Figure 4.8: 3D detection coverage of 8 sensor simulated array.

sensor coverage has relatively equal variation below the aircraft with expected reduction above the aircraft due to the presence of the ground plane but because the ground plane is not infinite the detection levels are only 10 dB less on average than below the aircraft; therefore, detection capability is broad for the B-dot sensors even when taking into account diffraction effects. Observations of the direction finding potential are now analyzed by looking at the summed fields.

4.3 Eight-Element High Frequency Direction Finding Array Characterization

As expected, the sensor sensitivity in the HF band is limited but the sensor does offer a relatively omni-directional detection capability. Figures 4.9, 4.10, and 4.11 are the eight-element antenna patterns for a sample of frequencies in the 2-32 MHz band. The patterns are with no phase added to the individual elements.

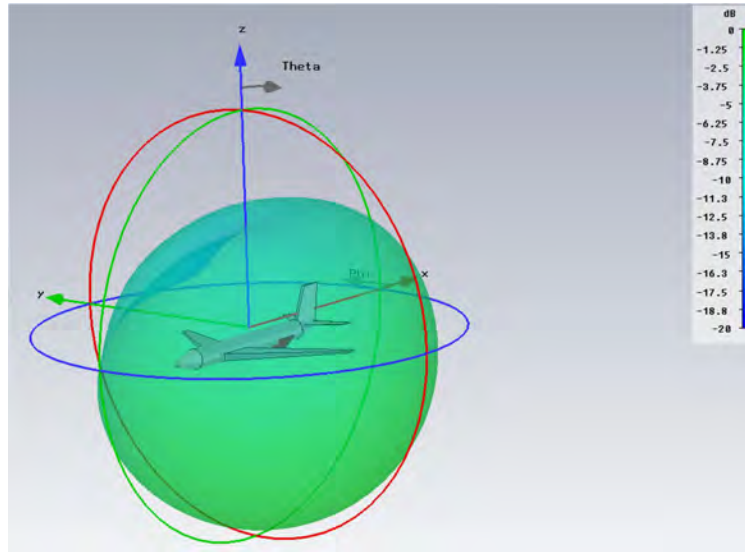


Figure 4.9: Normalized radiation pattern of an eight-cluster HFDF array at 2 MHz simulated in CST Microwave Studio

As projected by the array factor discussed in Chapter III the pattern shaping is limited at low frequencies. At 16 MHz some shaping does exist with a main lobe in the nadir

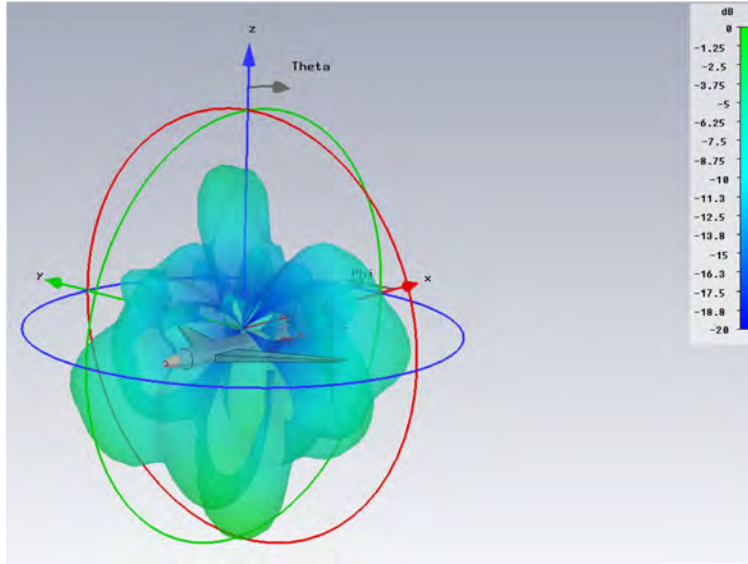


Figure 4.10: Normalized radiation pattern of an eight-cluster HFDF array at 16 MHz simulated in CST Microwave Studio

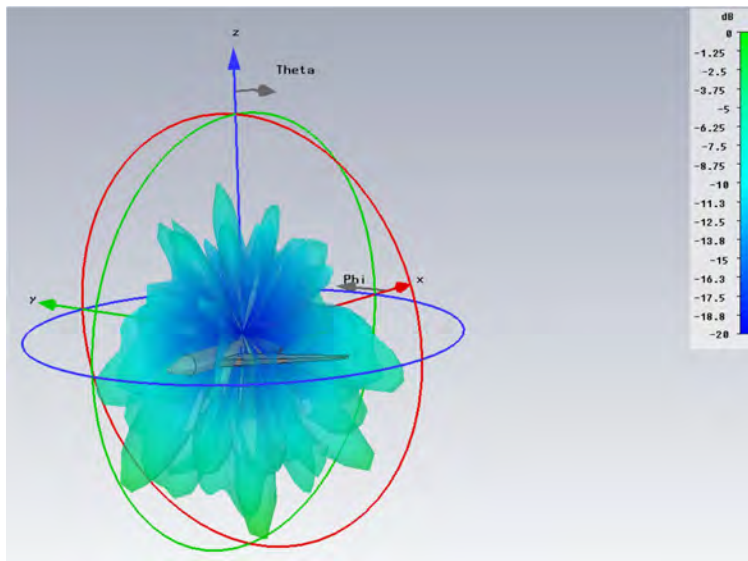


Figure 4.11: Normalized radiation pattern of an eight-cluster HFDF array at 32 MHz simulated in CST Microwave Studio

direction, as expected due to sensor orientation. The sidelobe levels are almost equivalent to the main beam based on the 20 dB dynamic range shown in all figures. The 32 MHz

pattern offers a narrow main beam but the sidelobe levels are only approximately 5 dB below the main beam. With only a 5 dB difference the direction of incident signal will not be clear when multiple signals are incident on the aircraft and when noise is added to the detection environment. Observation of 20 dB of dynamic range at 32 MHz provides the possibility to use null steering methods for direction finding. Null steering eliminates the need for reduced sidelobes. The key is the pattern must have deep nulls to distinguish when an incident signal is in a null. 3D fields are difficult to understand the effects in azimuth and elevation therefore XZ, YZ and waterline cuts serve as a descriptor for analysis of sidelobes and relative direction finding capability with no phase added to each of the elements.

Figure 4.12 is the XZ plane cut of the array with zero phase or amplitude progression. Figure 4.12 is a sampling from 2-32 MHz, Appendix A provides all patterns from 2-32 MHz with 1 MHz steps. Because of the non-uniform spacing of the array the XZ and YZ cuts are used to better understand the pattern shaping. At 2 MHz the directivity pattern, as shown previously in Figure 4.9, is nearly isotropic, which implies the extent of this array is not large enough to achieve the angular resolution necessary for direction finding. The inability to accomplish direction finding is due to pattern variations of only 2 dB below the aircraft waterline. The pattern at 22 MHz presents enough phase variation to produce nulls and a main beam. The extent along the fuselage is 3.6 meters less than that from left to right wingtip; therefore, the main beamwidth in the XZ plane at any given frequency is equal to the main beamwidth in the YZ plane 2 MHz below the observed XZ plane frequency. For example, in comparing the main beam of the XZ plane cut at 22 MHz, the comparable pattern in the YZ plane cut is at 20 MHz as shown in Appendix A. The shaping is not the same because the individual elements are not spaced the same along the fuselage as they are from wingtip-to-wingtip. Observations of the patterns of 22-32 MHz have nulls of -20 to -35 dB from the main beam. Sidelobes are only 5 dB down from the main beam in

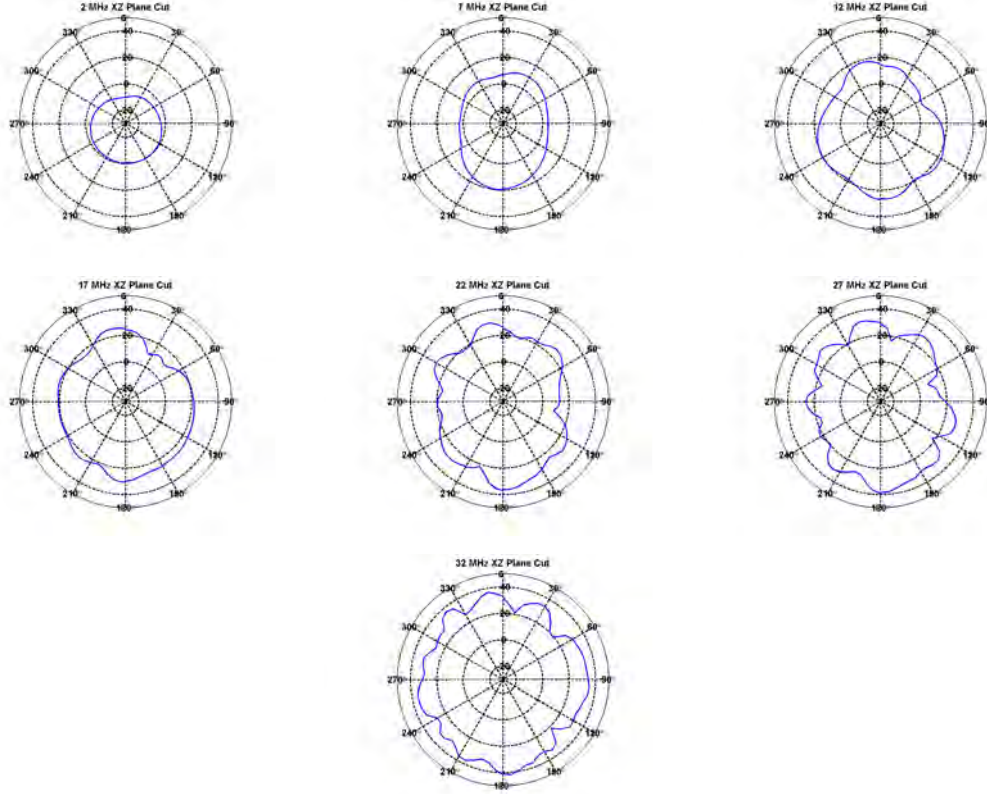


Figure 4.12: XZ plane cut of the directivity of an eight-cluster HFDF array for 2,7,12,17,22,27,32 MHz normalized to 2 MHz

the XZ cut; therefore, 30 degrees from nadir will be highly correlated with the main nadir facing lobe therefore elevation determination is difficult.

Figure 4.13 presents the YZ plane cuts at the same sampled frequencies as previously presented. The additional patterns are included in Appendix A. In the YZ direction the array shaping in elevation is greater with a main beam present at 17 MHz. As previously discussed this is due to the increased extent of the array along the YZ plane cut. Incident fields along the YZ cut can be correlated from 17-32 MHz with sidelobe levels only 3 dB below the main beam. As in the XZ cut, correlation of incident field is difficult because nadir detections are highly correlated in a 30 degree sector of the main beam. In the eight-element configuration the spatial sampling in the array is reduced from wingtip-to-wingtip

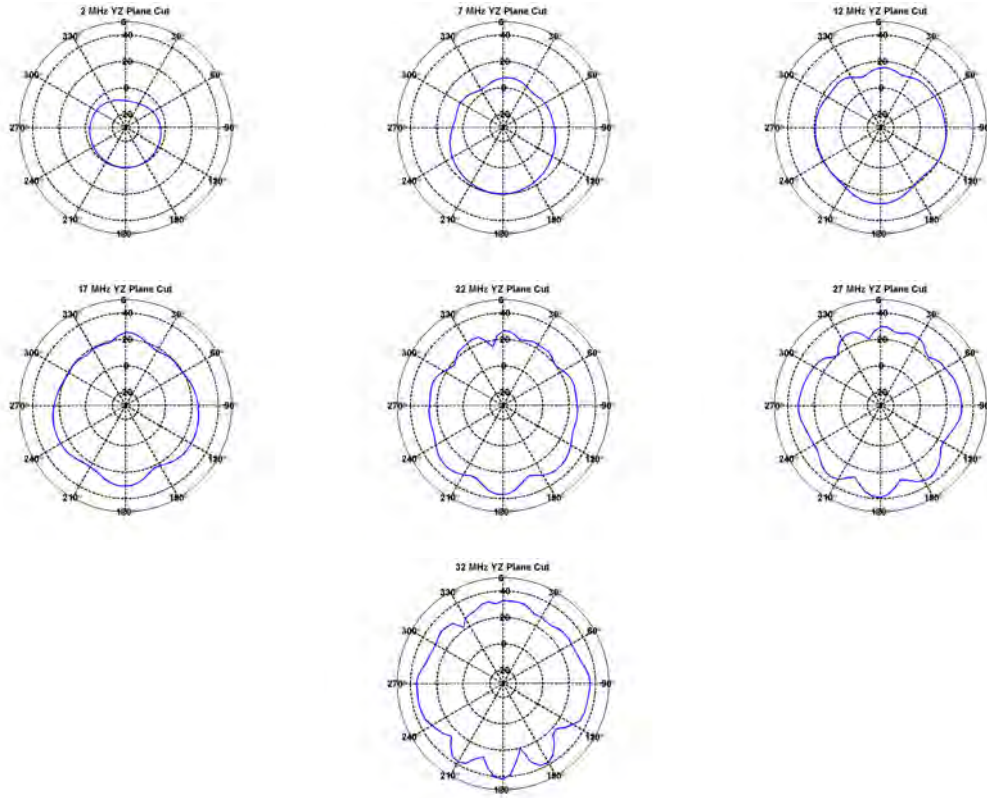


Figure 4.13: YZ plane cut of an eight-cluster HFDF array for 2,7,12,17,22,27,32 MHz

which increases the sidelobes; therefore, the sidelobes should be reduced in the XZ cut as has been previously shown by the 2 dB difference in first sidelobes between the XZ and YZ cuts. Observing the difference in the first sidelobes from the nadir beam support the usefulness of additional sensors in reducing the sidelobes and increasing null depth. The right side of the aircraft has an additional sensor and the null depth is 5 dB less than the left side of the aircraft. Based on the observations the ten-element array should offer increased null depth and reduced sidelobes.

Figure 4.14 is a sampling from 2-32 MHz of the waterline cut. Appendix B provides all other patterns from 2-32 MHz in 1 MHz steps. The waterline cut represents the azimuthal resolution of the uniform phase eight-element array. At 12 MHz the pattern shape has 10 dB reduction from the maximum value, but the nulls are broad and the

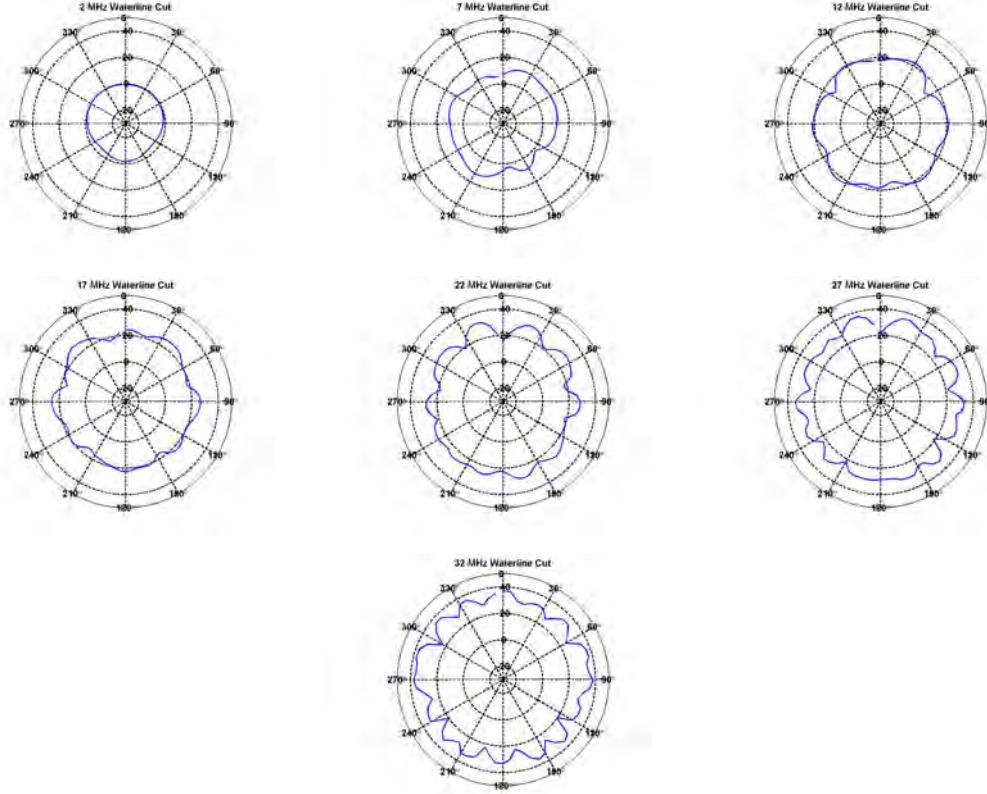


Figure 4.14: Waterline cut of an eight-cluster HFDF array for 2,7,12,17,22,27,32 MHz

individual beams are 60 degrees wide. Additionally, at 12 MHz the 90, 140, 220 and 270 degrees are highly correlated due less than 1 dB difference in these directions. At 2 MHz the pattern, as in the other cuts, is nearly isotropic making direction finding not possible with the eight-element array configuration without the use of DF algorithms. Observations of increased null depth are found above 17 MHz with -22 to -10 dB nulls. Across all frequencies the azimuthal resolution has strong correlation of multiple directions from the peaks in the patterns. Nulls provide larger differences in all directions at frequencies from 17-32 MHz, but both peak and null comparisons offer less than 10 dB differences when comparing one incident direction to another. For example, the null at 27 MHz is only 2 dB different from the null at 122 degrees. Overall, most directions are correlated with at least

a single direction across all frequencies making direction finding difficult due to a lack of ambiguity resolution.

The eight-element array analysis of the pattern of the uniform phase array proves that the array is highly correlated in azimuth and elevation in multiple directions. For this reason additional sensors will provide reduced sidelobes and increased null depth that can increase correlation with incident signals without ambiguities. The analysis of the ten-element array will be in comparing the eight to the ten-element array to show the sidelobe reduction and effects on the pattern based on the sensor added from BerrieHill research.

4.4 Ten-Element High Frequency Direction Finding Array Comparison

The ten-element array is designed to decrease sidelobes and increase null depth in the HFDF airborne array. The elements were added based on the BerrieHill research [4] utilizing SI monopole feeds in order to maximize the efficiency of the B-dot sensor. Additionally, the sensor location was chosen based on adding the most possible spatial diversity to the array in order to achieve the greatest impact on the overall array pattern. Figures 4.15, 4.16, and 4.17 are 3D farfield patterns of the ten-element array.

Observations of the farfield patterns present the greatest impact of the additional sensors at 32 MHz. The main beam is narrowed and sidelobes have reduced levels in the nadir direction. At 2 MHz the pattern still exhibits nearly isotropic characteristics. It is expected that the impact to the pattern at 2 MHz should be minimal, because the additional sensors are do not increase the spatial extent of the array; therefore, main beam shaping is non-existent. Just as in the eight-element array observations of the differences in the farfield are difficult in 3D comparisons. The use of XZ, YZ, and waterline cuts will be used to look at the changes the in two arrays. Average sidelobe level and integrated sidelobe level depict the overall effect of adding the two sensors on improvement in pattern shaping.

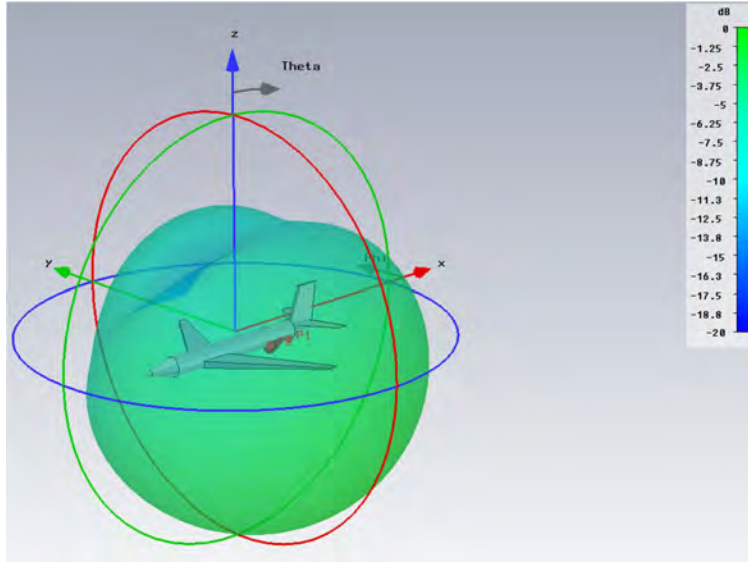


Figure 4.15: Normalized radiation pattern of a ten-cluster HFDF array at 2 MHz simulated in CST Microwave Studio

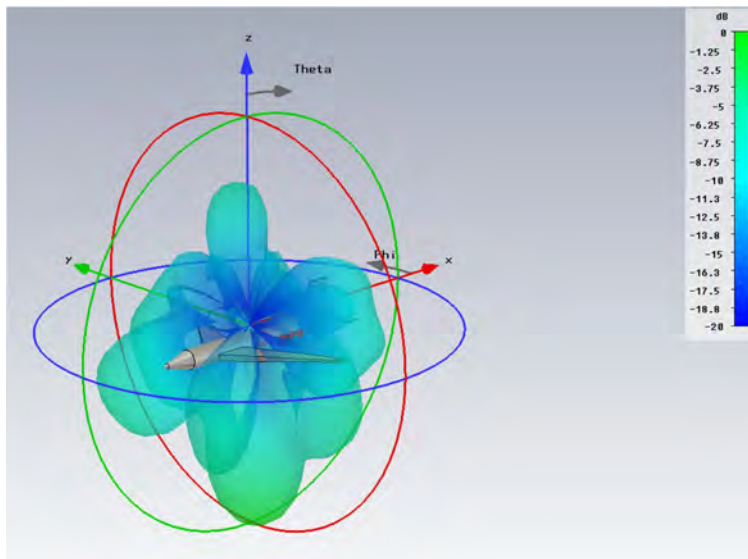


Figure 4.16: Normalized radiation pattern of a ten-cluster HFDF array at 16 MHz simulated in CST Microwave Studio

Figure 4.18 is a comparison of the eight and ten-element arrays at 2 MHz. For all comparisons between the eight and ten-element arrays the red lines represent the ten-

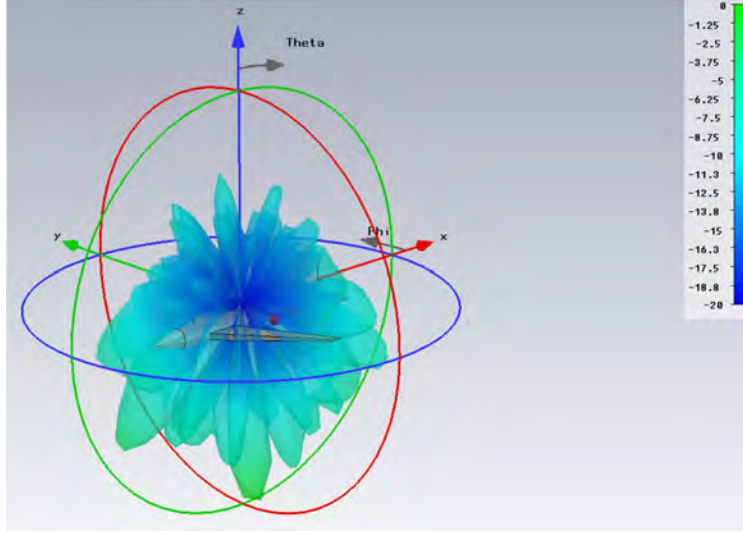


Figure 4.17: Normalized radiation pattern of a ten-cluster HFDF array at 32 MHz simulated in CST Microwave Studio

element array, while the blue lines represent the eight-element array. Additionally, all patterns are normalized to themselves for comparison of directivity. Cartesian plots are used to better observe the differences in the patterns and the sidelobe and null changes that can be difficult to decipher in polar form. The previous observations of a lack of shaping

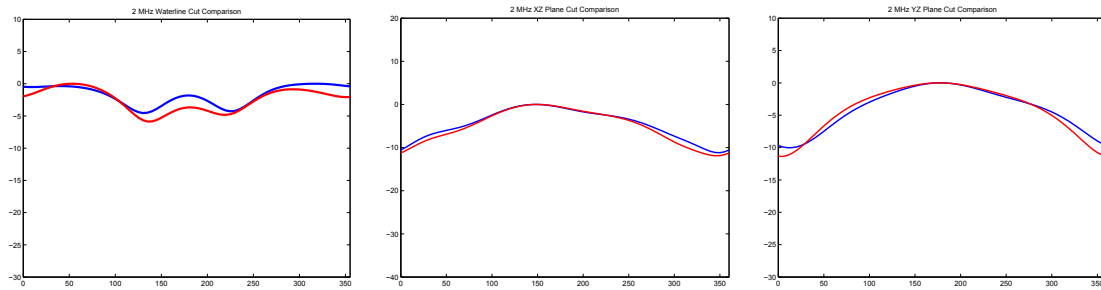


Figure 4.18: Comparison of normalized waterline, XZ, and YZ plane cuts for ten vs eight-cluster array at 2 MHz

due to limited array extent is observed in the comparison of the two arrays. The added sensors do cause a difference in the pattern but it merely shifts the farfield pattern, because additional sensors are summed into the detection capability. The YZ and XZ cuts have less

than 1 dB difference for a given incident angle. The patterns should have minimal changes because the largest spacing change in the x-direction is less than 0.1 wavelength at 2 MHz causing little to no change in azimuth patterns. The differences in the waterline cut are only in slight shape changes in comparison to the eight-element array.

Figure 4.19 is a comparison of the eight and ten-element arrays at 16 MHz. The

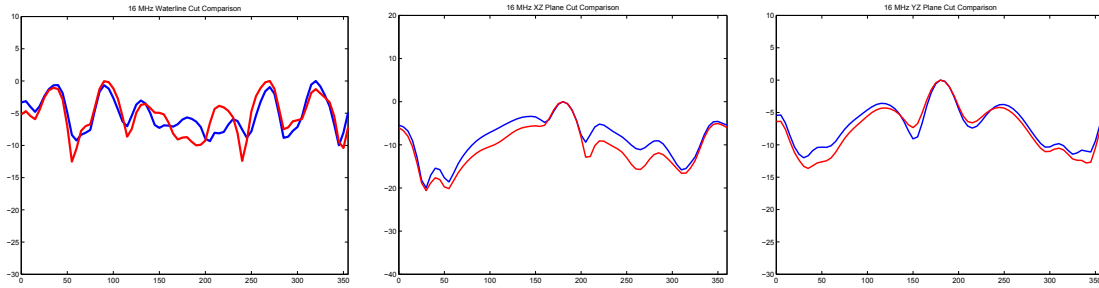


Figure 4.19: Comparison of normalized waterline, XZ, and YZ plane cuts for ten vs eight-cluster array at 16 MHz

waterline cut presents two positive factors in the direction finding array, increased null depth and reduced side lobes. The nulls at 51, 105, and 240 degrees are reduced by 5, 2, and 5 dB respectfully. Additionally, the null is reduced for each of these angles. The same problems still exist with the correlation for direction finding with the ten-element array. Signals incident at 90 and 270 degrees will be highly correlated and at 30 and 320 degrees will be highly correlated because the differences in the patterns are less than one dB. The XZ plane cut has an improvement in sidelobe level and null reduction. As discussed earlier, the impact is expected to be the greatest in this cut due to in the increased spatial diversity in the x-direction by adding the two elements. A 3 dB reduction in sidelobes is seen from 60-275 degrees. Null depth changes are negligible in this cut. Though sidelobes are reduced, when comparing the shape and depth of the nulls between the two patterns they are nearly identical. The YZ plane cut offers little change in pattern from the eight to ten-element array due to the limited spacing between elements between the wingtips. The difference in

the y-direction of the new sensors to the sensors along the fuselage is 0.08 wavelengths so the effect is less than 1 dB difference in the patterns at any given angle.

Figure 4.20 is the comparison of patterns at 32 MHz. The waterline cut at 32 MHz

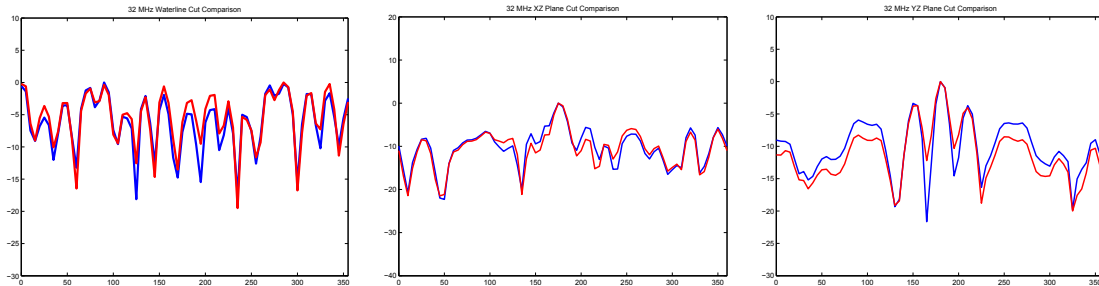


Figure 4.20: Comparison of normalized waterline, XZ, and YZ plane cuts for ten vs eight-cluster array at 32 MHz

has increased depth and narrowing of nulls at 50, 240, and 300 degrees. The common nulls at 300 and 50 degrees are expected in a linear type of array, but the null at 120 which in a linear array would be equal to the null at 240 degrees is increased in the ten-element array. This is due to the non-uniform spacing of the array which assists in eliminating these common angles in the pattern. Common angles lead to ambiguities so adding additional sensors at varying spacing will continue to reduce the ambiguity between angles. The peaks are increased at 190 and 170 degrees with a decreased null depth at these angles by 2.5 and 5 dB respectively. The XZ and YZ plane cuts show reduction in sidelobes. The greatest reduction in the XZ cut is at the first sidelobe. A reduction from -5 to -9 dB shows suppression from only adding two additional sensors. Reduction in sidelobes occur at nearly every incident angle for the YZ plane cut. At 170 and 190 degrees the nulls are increased making the ability to null out a signal off of the main beam more difficult with the ten-element array, but with the continued addition the sensors those nulls could be reduced to the previous levels. Due to the limited reduction in sidelobes and the difficulty of comparing each pattern for an overall increased effectiveness of the ten-element array

the integrated and average sidelobe level have been calculated to better determine if the sensor location is an improvement over the eight-element array.

Table 4.1 is the integrated and average sidelobe levels for 2, 16, and 32 MHz for the eight and ten-element arrays. Appendices C and D include all frequencies from 2-32 MHz at 1 MHz steps for both eight and ten-element arrays. At 2 MHz the averages show

Table 4.1: Average and integrated side lobe level in dB for a sample of frequencies from 2-32 MHz of the eight and ten-element arrays.

Eight-Element Array

Frequency (MHz)	Waterline Average	XZ Cut Average	YZ Cut Average	Integrated Waterline	Integrated XZ Cut	Integrated YZ Cut
2	-3.83	-7.07	-6.75	-72.76	-304.00	-256.62
16	-6.40	-9.16	-7.48	-351.85	-622.76	-501.39
32	-7.93	-10.75	-10.38	-412.34	-752.83	-737.27

Ten-Element Array

Frequency (MHz)	Waterline Average	XZ Cut Average	YZ Cut Average	Integrated Waterline	Integrated XZ Cut	Integrated YZ Cut
2	-4.47	-7.69	-7.35	-125.14	-346.21	-264.72
16	-6.69	-11.38	-8.13	-354.76	-773.79	-544.90
32	-7.44	-11.02	-11.62	-364.45	-771.40	-813.24

that greatest difference in the YZ plane cut, but the differences are less than a dB for all cut comparisons. The integrated sidelobe level comparison at 2 MHz presents little to no difference when all angles are considered. This is due to the lack of shaping in the pattern and limited change in the pattern due to the long wavelength. At 16 MHz the greatest difference for average and integrated sidelobe level is in the XZ plane cut. This is due to the limited phase difference at 16 MHz in the y-direction. Based on the observations at 2 and

16 MHz an argument can be made that elimination of one of the sensors will not change the pattern drastically due to the limited phase difference between the two additional sensors in the y-direction because the YZ plane cut is not affected at 16 MHz. The comparison at 32 MHz shows that the phase difference at higher frequencies is adequate enough to make both sensors relevant in the array performance due to the greatest sidelobe level change being in the YZ plane cut. Additionally, higher frequencies have reduced angular ambiguities with both sensors included in the array due to non-uniform element spacing. Overall, both sensors do assist in reducing the sidelobes at any frequency above 5 MHz based on the pattern and sidelobe level comparison in Appendix B considering effects on all pattern cuts.

4.5 Non-Uniform Phase Analysis

An analysis of the direction finding capability utilizing a non-uniform phase on the individual elements was accomplished within MATLAB. Within CST Microwave Studio the field definitions for each sensor location are shifted to the origin and exported as a text file. In MATLAB the phase shift due to the sensor spacing is added based on the same spacing utilized in the CST simulations. In addition, phase is added to individual array elements to shift the nadir beam to a specified direction in order to improve the azimuthal resolution of the array. The fields were adequately imported into MATLAB but the field definition within CST Microwave Studio is not fully understood. The physical phase shift could not be added to reproduce the summed fields with an array-centered global coordinate system that is output from CST Microwave Studio. To fully assess the direction finding capability of the eight and ten-element arrays the field definitions must be better understood to incorporate the appropriate phase shift due to the array spacing and reproduce the uniform phase array presented in this thesis. From the point of adding the physical phase shift within MATLAB, the phase for beamforming can be added to better assess the direction finding capability. Phase shifts can be added within CST Microwave Studio if all

elements are simulated in a single simulation. The only way this can be accomplished is to utilize an improved graphics processing unit (GPU) with additional memory. With the current Tesla GPU only four sensors can be simulated; therefore, the GPU memory must be larger in order to accomplish the simulation. The exact size of the GPU is unknown because with the addition of each sensor, the memory required to calculate the sensor contribution does not increase linearly due to the mutual coupling between the newly added sensor and the entire array. A single CST simulation would be the optimum way to evaluate the array because the optimization tools within CST can be used to determine the optimum phase for a given main beam direction. The simulation time is going to be greater than a month, but the simulation setup is already complete based on this research; therefore, the individual simulations can be combined into one larger simulation once the processing hardware is available.

4.6 B-dot Test Analysis

The B-dot cluster detection test is for comparison to the simulated results to validate the simulation and theory of the B-dot sensor. To analyze the 20-second collection the fast fourier transform (FFT) is taken to interpret the frequency content of the data. Figure 4.21 is the FFT of the B-dot, dipole, and noise collections. The dipole collection proves that detectable signals existed during the collection. Modulation is observed in the detection. Additionally, 20 dB peaks are observed in the signal collections around 7, 19, 24, and 27 MHz. The modulation could be inherent in the receiver because it occurs from 2-32 MHz which it is not typical for a wideband signal source in the HF frequency band. The frequency content of the 20-second collection of the B-dot cluster and noise have few differences, which could mean the sensors are too inefficient to overcome the internal noise of the receiver. Correlation allows for a comparison of B-dot to dipole to noise collections. The correlations allow for reduction in noise because of the random nature of

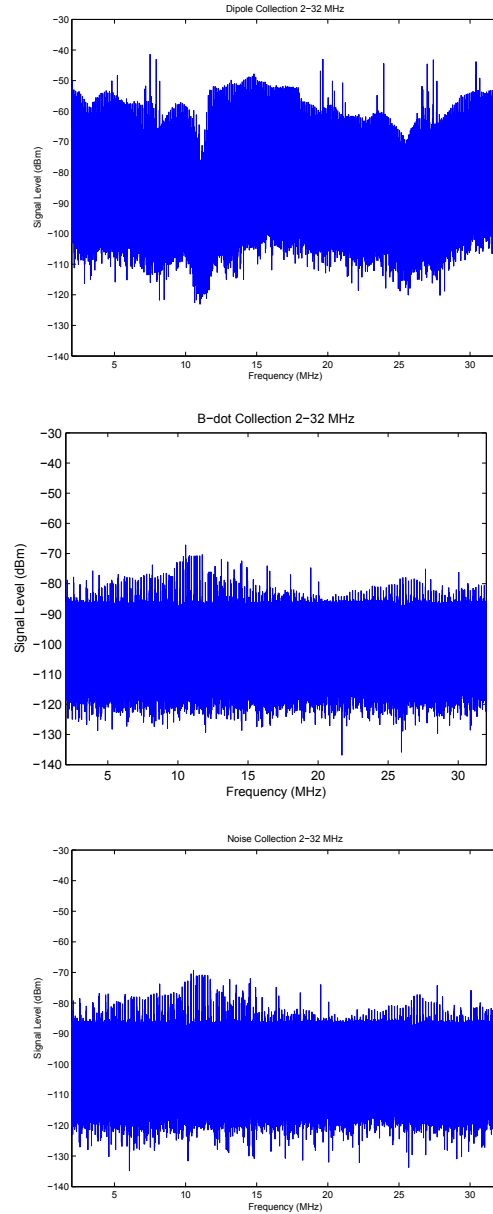


Figure 4.21: Fast Fourier transform of 20-second collection of Dipole, B-dot sensor cluster, and noise from 2-32 MHz

noise, and creates an increase in common signals in the compared detections. Figure 4.22 is a comparison of the correlation of B-dot cluster, dipole and noise.

The four correlations appear to show no discernible difference between B-dot cluster data and system noise. Comparing the dipole to noise and the dipole to B-dot correlations

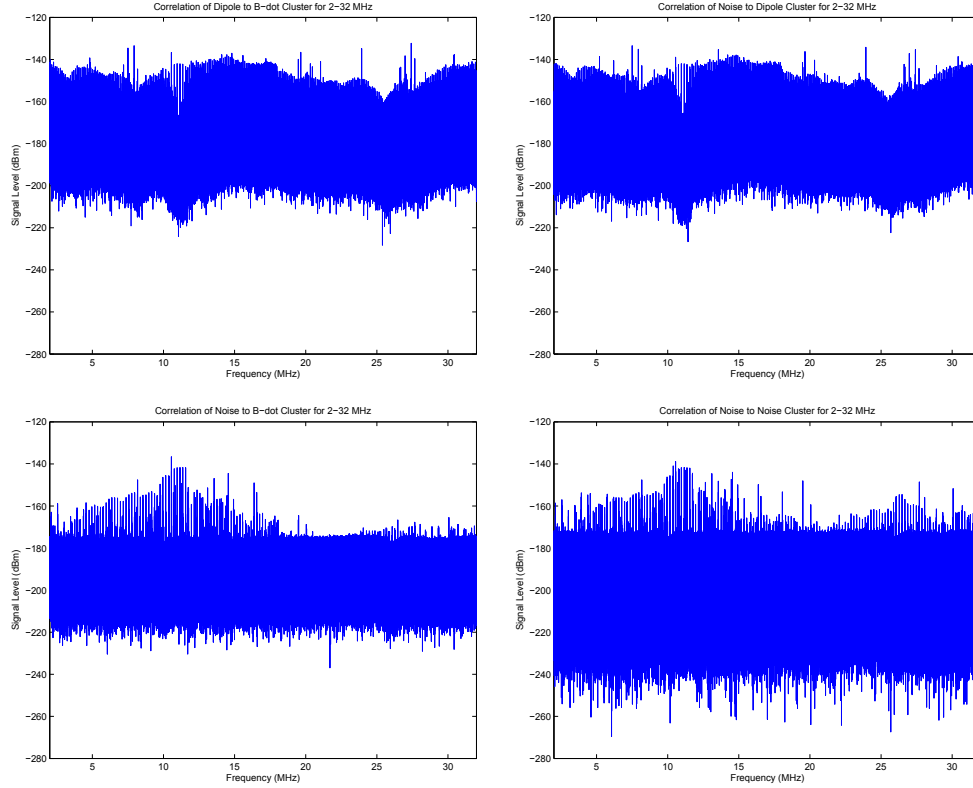


Figure 4.22: Correlation of 20-second collection of noise to B-dot cluster, noise to dipole, dipole to B-dot cluster and noise to noise

the signals take on the signal content of the dipole which means most of the B-dot sensor cluster detection content is primarily the receiver noise. The correlation of the B-dot sensor cluster to the dipole produces only common signals in the 26-32 MHz frequency range. The common signals are found at 27 MHz. To reduce the noise floor and increase the ability to separate the correlations signal integration can be used on the signals. To validate that integration can be used, the 20-second collection is separated into 1.25-second detections and compared to validate that common signals exist over the entire collection time. Based on the signal analysis a 1.25-second integration time is applied to each detection to assess the effect of integration on the detection capability of the B-dot sensor.

Figure 4.23 is the dipole, B-dot cluster, and noise spectrum utilizing a 1.25-second integration time. The dipole integrated collection validates the previous analysis that the

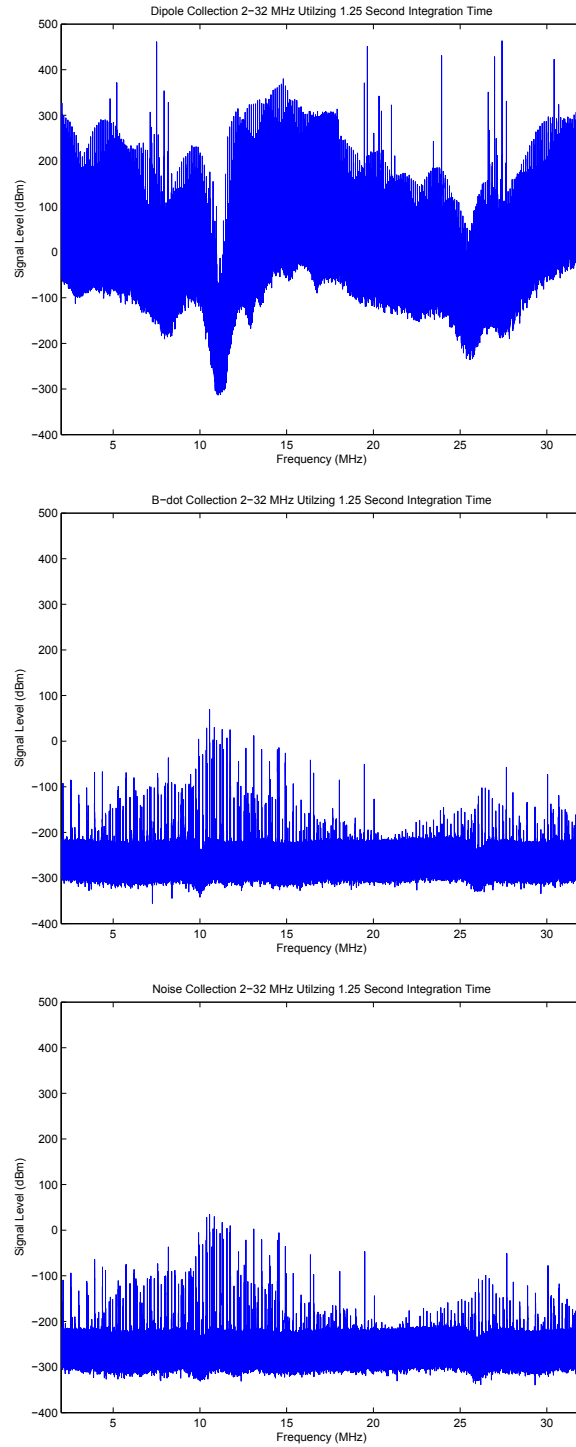


Figure 4.23: Fast Fourier transform of 20-second collection with 1.25-second integration time of dipole, B-dot sensor cluster, and noise from 2-32 MHz

likely signals that for B-dot cluster detections are at 7, 19, 24, and 27 MHz. Additionally, signals at 5.5 and 30 MHz are separated from noise by 100 and 125 dB respectfully. As expected in comparing the B-dot cluster collection to the noise collection the integrated signal detection appears to have the same signal content. Non-random signals were collected for noise and the B-dot cluster during the 20-second collection. The signals could be due to resonances in the cabling or additional noise added by the four port summer used to combine the detections of the individual B-dot sensors. Due to the 0.05 Hz frequency resolution, it can be difficult to observe signal differences without the use of correlation, so signals might appear to be the same but have slightly different frequency content.

Figure 4.24 is a comparison of all correlations utilizing a 1.25-second integration time. With the use of a 1.25-second integration no additional difference is observed in comparing B-dot to noise collections. With the additional noise reduction based on integration the noise and B-dot data correlations with the dipole contain dominant dipole signals. An analysis presented in Chapter 3 stated that a 10 msec integration time would be necessary to detect signals with the single B-dot sensor. Assuming the four-sensor cluster will require 1/4 the integrations to achieve the necessary power levels for sensor detection; therefore, it is not surprising that detection is limited. To completely analyze the data a 100 msec integration time spectrum and correlation is provided in Appendix F, but no significant differences are observed between the noise and B-dot collection. The analysis within Appendix F is only accomplished for 26-32 MHz because the most common signals were found in this frequency range. In addition to requiring a smaller integration time, the noise floor of the HF receiver is -107 dBm. Based on the total efficiency of the B-dot sensor ranging from -92 dB to -127 dB requires at a minimum a 20 dBm signal to be incident on the sensors to detect a signal above the receiver noise. The B-dot sensor cluster detection validates that improvements to the sensor are required to achieve a detection capability from 2-32 MHz.

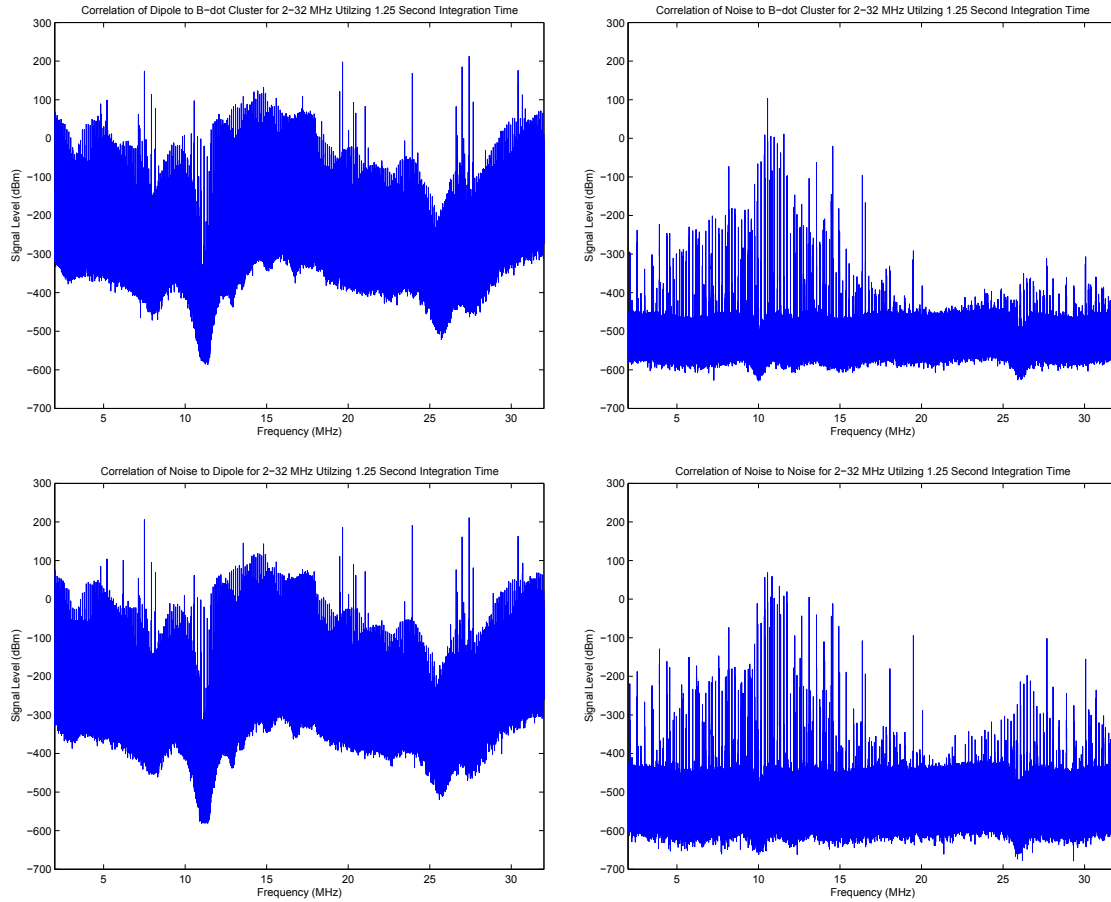


Figure 4.24: Correlation of 20-second collection with 1.25-second integration time of noise to B-dot cluster, noise to dipole, dipole to B-dot cluster, and noise to noise

4.7 BerrieHill Structurally Integrated Monopole Comparison

The previous research in HFDF has been in determining an adequate sensor for detection of signals in the HF band. HFDF research by BerrieHill Research Corporation is in the use of monopole feeds to detect the currents induced on an aircraft by an incident signal. The monopole placement is decided based on choosing the location of highest current density dependent on mode and frequency of the incident wave. The B-dot sensor and the ten-inch monopoles are compared to find which would be better served in a HFDF application. From the eight-element array design two sensor locations are common to the

BerrieHill computational analysis. Figure 4.25 is the ϕ and θ components of the electric field of the B-dot sensor and the SI monopole feeds at 4 MHz for sensor location one.

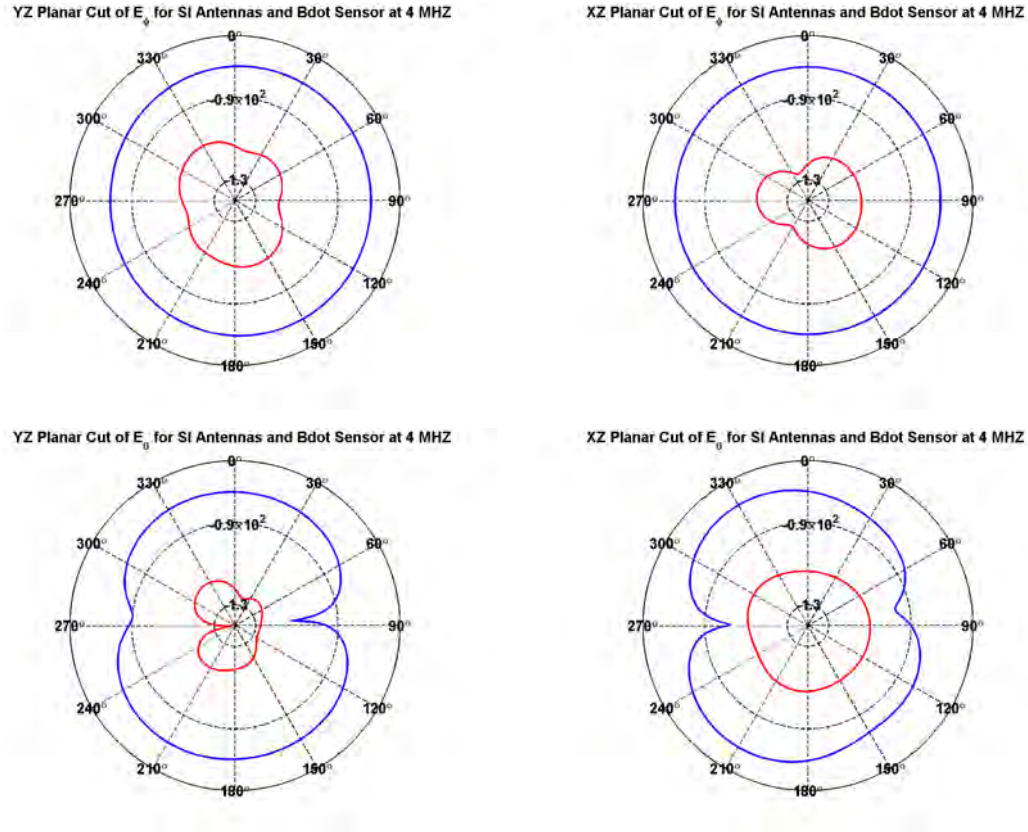


Figure 4.25: fig: XZ and YZ plane cuts for the theta and phi component of the electric field at 4 MHz of the SI monopole at location one versus B-dot sensor at location one.

Overall, the B-dot sensor sensitivity at 4 MHz is between 15 and 40 dB below the SI feeds. Both feeds offer relatively isotropic patterns that are necessary for detection in direction finding. Previous research accomplished by Corbin, [7], presents electric fields for the BerrieHill feeds at between -25 and -50 dBW but this is incorrectly represented. The described field strengths are in volts not watts therefore the field strength is lowered by a factor of two. The comparison does not vary substantially at 11 MHz as shown in Figure 4.26.

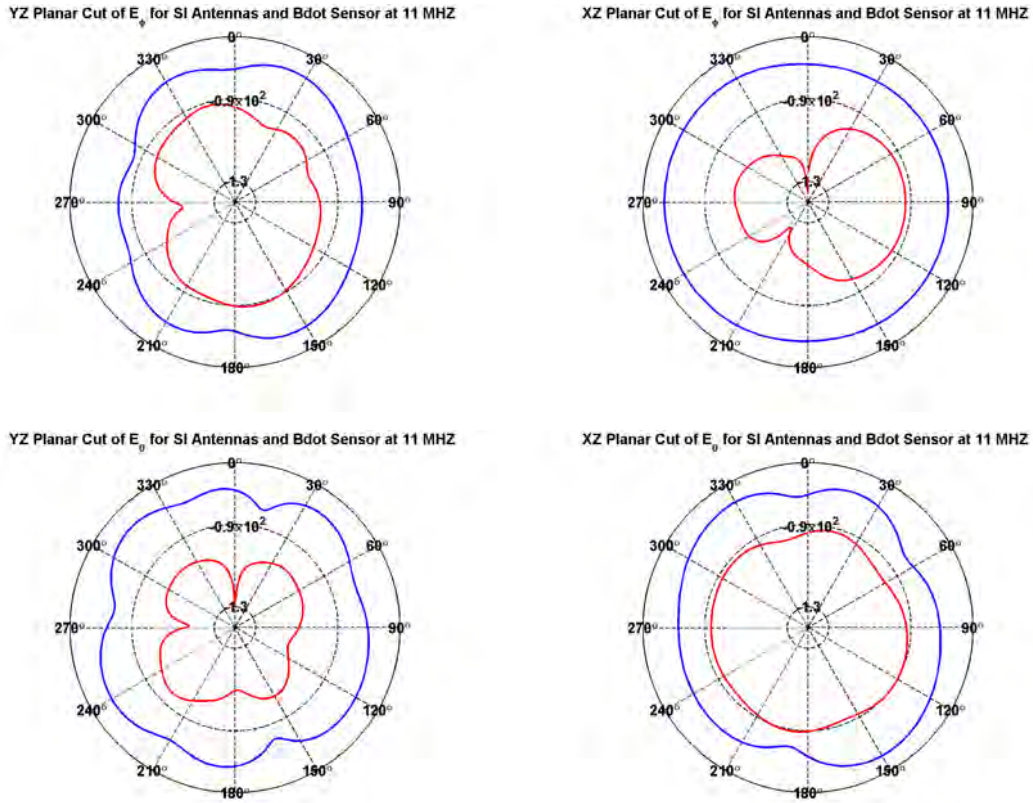


Figure 4.26: XZ and YZ plane cuts for the theta and phi component of the electric field at 11 MHz of the SI monopole at location two versus B-dot sensor at location one.

Sensor pattern shaping is relatively isotropic with a reduction in variation between the B-dot and the BerrieHill feed to only a 15-30 dB difference. The sensor two location comparison is provided in Appendix E, but the difference between the two sensors is still maintained at location two for both 4 and 11 MHz. Table 4.2 is the average difference in values between the BerrieHill SI monopole feeds and the MGL-S8A B-dot sensor are both locations. The data presented has a standard deviation of 9 dB for a 95 percent confidence interval.

Based on the standard deviation, the majority of the differences fall around 30 dB which implies the B-dot sensor is an inadequate sensor in comparison, but the feasibility of the B-dot sensor for application on an aircraft, especially on the wingtips make it still

Table 4.2: Average of the difference between the BerrieHill monopole feeds and the MGL-S8A B-dot sensor electric field components at two common simulated locations for 4 and 11 MHz.

	Left Wing Theta Difference	Left Wing Phi Difference	Right Wing Theta Difference	Left Wing Phi Difference
YZ Cut	31	20.29	21.70	17.11
XZ Cut	18.04	33.05	17.77	18.89
YZ Cut	42.95	36.71	32.48	30.32
XZ Cut	31.05	42.43	21.80	32.54

a valuable comparison. The monopole design based on a 10-inch monopole could cause problems with flight worthiness due to aerodynamic heating and issues with airflow over the wings. A larger B-dot sensor has improved radiation characteristics in the HF band. Figure 4.27 is a plot of the radiation efficiency of a simple loop with an equivalent radius for the MGL-S8A, the MGL-5 and MGL-4 B-dot sensors. The MGL-5 and MGL-4 are sensors with increased radius by 4.5 and 9.4 times larger than the MGL-S8A sensor respectfully as shown by the URS specification sheet in Appendix G [26]. Based on the previous comparison of the simple loop to the simulated B-dot sensor it can expected that the two variants will increase the radiation efficiency by 20-30 dB. The largest B-dot sensor has an overall height of 5 inches and also has an aerodynamic profile that makes it more applicable on an aircraft wingtip while achieving equal performance. The MGL-5 sensor offers an expected 20 dB increase with only 2.48 inches tall and is only 10 X 13 inch ground plane. The ground plane is ten times larger than the MGL-S8A B-dot sensor which must be considered for integration into an aircraft. The MGL-4 ground plane is 16 X 25 inches which makes it difficult to integrate into an aircraft. The MGL-5 is the best sensor to achieve equal performance to the BerrieHill SI monopoles based on increased radiation efficiency and aircraft integration.

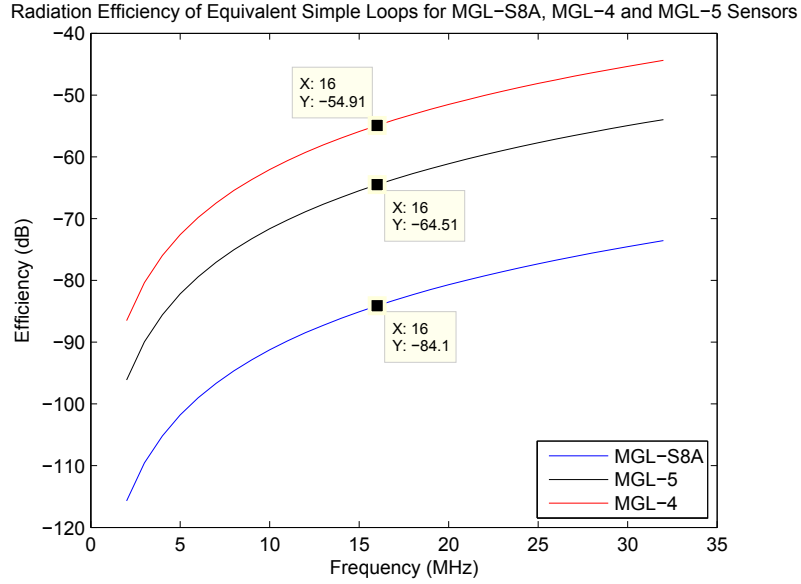


Figure 4.27: Comparison of MGL-S8A B-dot sensor to MGL-5 and MGL-4 variations

To validate the expected performance of the MGL-5, an approximate sensor is designed in CST Microwave Studio as an initial simulation design. This sensor is designed based on the increased radius defined by the differences in height from the B-dot sensor specifications sheet provided by URS Corporation [26]. All B-dot sensor variations are available from URS Corporation and Prodyne Technologies but the URS specifications sheet is used for this comparison. Due to time limitations and a lack of exact specifications, the design is based on an equivalent design to the MGL-S8A B-dot sensor with a radius 4.5 times larger than the MGL-S8A. Due to design issues in CST the gaps are also designed using air gaps instead of FR-4 filled gaps. To validate the difference between air filled and FR-4 filled gaps a simulation of the MGL-S8A was accomplished with air gaps. The average difference for the two simulations is 0.285 dB with a standard deviation of 0.325 dB. Appendix H includes the plot of the radiation efficiency of the air gap and FR-4 simulations versus frequency. Overall, it can be observed that the difference in simulations is negligible; therefore, the air gap should not affect the simulation of the

MGL-5 sensor. Due to possible design differences between the MGL-5 and the MGL-S8A, a design description needs to be used to create a sensor model in CST Microwave Studio to validate the MGL-5 simulation presented in this research. Figure 4.28 is a comparison of the radiation efficiency of the MGL-S8A to the MGL-5 B-dot sensors. The MGL-5 B-dot

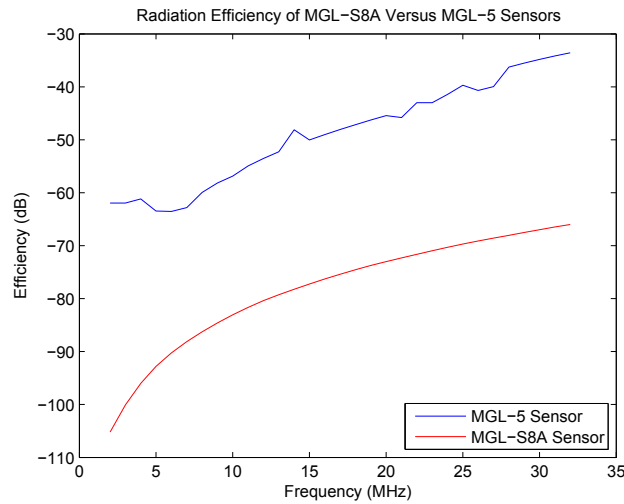


Figure 4.28: Comparison of radiation efficiency of MGL-S8A and MGL-5 B-dot sensors.

sensor simulation does have an issue with simulation accuracy from 2-6 MHz. Overall, the sensor follows the expected curve for a loop sensor from 6-32 MHz. The MGL-5 is an improvement of 25-32 dB from 6-32 MHz. Based on this sensor simulation the sensor should be equivalent on average to the 10-inch monopole feeds for an airborne HFDF array.

4.8 Conclusion

This chapter outlined the results of the airborne HFDF array research effort. The determination was made that the effectiveness of the MGL-S8A B-dot sensor was not adequate for the HF application but possibly the use of a larger sensor will provide equal sensing performance to the SI monopole feeds researched by BerrieHill. Additionally, an analysis of the effectiveness of the ten and eight-element arrays for direction finding were

established. Though the uniform phased array provided reduced direction finding ability due to the large sidelobes additional research into steering the array could offer improved direction finding performance. Chapter V details the findings of this research effort and offers some areas of future research in creation of an airborne HFDF array.

V. Conclusions and Recommendations

The goal of this research effort was to evaluate the usefulness an MGL-S8A B-dot sensor for use in a high frequency direction finding (HFDF) array. The detection capability of the sensor along with the ability of an eight and ten-sensor array to accomplish direction finding were the primary focuses of this research. Additionally, the previous research by BerrieHill Corporation, [4], is evaluated to compare the structurally integrated monopole design to the B-dot sensor in terms of detection capability. The additional elements added to create the ten-element array were placed based on research by BerrieHill in order to maximize sensor detection capability and maximize phase difference between adjacent element. All analysis and comparisons are accomplished based on simulations of the sensors and aircraft fuselage in CST Microwave Studio. In addition to the simulations, a field test was completed to validate the simulations of the cluster of B-dot sensors by detecting high frequency (HF) transmissions with a cluster of four B-dot sensors and an HF receiver. The test included the use of a very high frequency (VHF) dipole as truth and the noise data was collected in order to perform a correlation between the detections of noise, the dipole, and the B-dot cluster.

5.1 Conclusions

The MGL-S8A B-dot sensor, design for frequencies greater than 5 GHz, is not adequate for direction finding applications in the HF frequency band. Though it does offer the relatively isotropic pattern even with diffraction considerations of the aircraft ground plane, the sensor is still 30 dB less effective than the BerrieHill structurally integrated monopole design. The B-dot sensor design is valid for application to airborne HF direction finding. The MGL-5 B-dot sensor is designed for frequencies above 700 MHz and offers an increase in effectiveness over the MGL-S8A with only a two-inch vertical profile. Based

on a theoretical loop comparison and a representative air gap B-dot sensor designed in CST Microwave Studio the MGL-5 sensor will be equivalent to the BerrieHill monopole with an eight-inch reduction in vertical profile which is important for aerodynamic considerations for integration on an airborne platform.

The four-sensor B-dot cluster proved to increase the radiation efficiency by 6 dB. Due to the poor radiation efficiency of the B-dot sensor the 6 dB improvement does not offer an increase that makes the MGL-S8A cluster adequate for signal detection. Based on the use of the MGL-5 B-dot sensor the 6 dB increase of using a sensor cluster will improve the detection ability reducing sensitivity requirements of the HF receiver but the sensor must first be more efficient. A four sensor cluster using the MGL-5 sensor could offer a substantial increase in detection capability due to the increased efficiency of the individual sensor. Integration considerations must be considered because the four sensor cluster would occupy a 20 X 26 inch area on the aircraft body.

A goal of this research is to establish the direction finding capability of the airborne HFDF array. The eight and ten-element direction finding capability is limited due to the lack of sidelobe reduction from the mainlobe. The addition of two sensors does show that including additional sensors will reduce side lobes and improve the null depth for distinguishing between two different directions of incident signals. Previous research by Corbin and BerrieHill Research Corporation shows that with a reduction in phase difference between elements that direction finding is possible with eight elements within ± 2 degrees [4, 7]. Based on additional phase difference added to with the presented eight and ten-element designs are an improvement in pattern capability; therefore, applying the direction finding algorithms presented by Corbin and BerrieHill the direction finding capability will be improved [4, 7].

One of the research goals was to validate the operation of the B-dot sensor cluster by accomplishing a detection test with an HF receiver. Based on the simulation results

and the expected efficiency of the sensor it was expected that the sensor would require a strong signal to detect in an open air application. Though the sensor detections could not be distinguished from the noise of the receiver, it did validate that an improved sensor is required to detect signals in the HF band. The method of signal processing presented in this thesis is useful for future sensor characterization and analysis. Additionally, the use of a low noise amplifier (LNA) must be considered when testing any inefficient sensor. The LNA will increase the signal strength up to 20 dB with a low noise figure maximizing the detection ability of a sensor. Increasing signal strength is important the key to detecting signals for direction finding is increasing the signal to noise ratio (SNR) [27].

5.2 Recommendations and Future Work

Based on the inefficiencies of the MGL-S8A B-dot sensor in the HF band and the initial analysis of the MGL-5 B-dot sensor future work in characterization of the MGL-5 sensor is required. The process for determining the effectiveness of the MGL-5 sensor is provided based on the research presented in this thesis and from previous work by Hardin [2]. The accuracy of the simulated B-dot MGL-5 sensor can be improved with the specifications from URS Corporation. The effectiveness of the sensor is expected to be increased because of impedance matching and feed design. The presented feed design is only based on the research of the Air Force Weapons Laboratory (AFWL) and because the MGL-5 is an variation on the AFWL design the feeds might be improved and the gap design could improve the efficiency of the sensor. Additionally, the MGL-5 is designed with air gaps instead of dielectric gaps which will change efficiency in the characterization. With a complete characterization of the MGL-5 the improvement in efficiency can be validated and additional system analysis can be accomplished based on the Berriehill SI monopole, the B-dot Sensor, and the SQUID sensor.

The research presented here is based on a single orientation of the B-dot sensor. Previous research by BerrieHill Research Corp. was done with varying orientation of

SI monopoles. Applying the B-dot sensor analysis with varying orientations can offer variations in detection based on the type of transmitting antennas. Adding sensors to the current design utilizing varying orientations can change the pattern and the detection ability of the array. Additionally, if the individual sensor signal levels are observed the polarization of the emitter can be determined. Switching detection polarizations will also offer an increased ability to detect multiple signal types and detect signals based on a changing flight profile.

The key to moving this research forward is an effort in looking at the entire system. The analysis must be based in determining the effects of each component within the DF array and the integration of all components. The sensor locations have been chosen to maximize the efficiency of the inefficient sensors based on the efficiency defined in this research and by BerrieHill. To serve as an example of a basic system design is shown in Figure 5.1. The LNA is defined by noise figure (NF) and amplifier gain. Applying

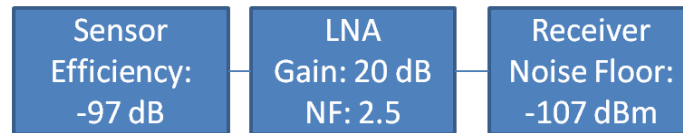


Figure 5.1: Example of HFDF array system analysis

the signal analysis completed in the thesis to a system as shown here the definition of what sensor efficiency is required for adequate signal to noise ratio (SNR). As an example, utilizing the expected total efficiency of the MGL-5 B-dot sensor of -97 dB, at 2 MHz, the required incident signal for an SNR of 10 is -20.2 dBm which corresponds to a range of 198 km for 10 kW effective radiated power [28]. The total efficiency is based on an expect 30 dB increase in efficiency for the MGL-5 B-dot sensor. Going beyond this analysis should look at cable losses, individual sensor losses, and receiver noise based each sensor location.

In addition to analyzing the sensor efficiency requirement, understanding what sensors can be used in different locations on the aircraft assists in improving the detection ability of the array. The B-dot sensor is not expected to be the only sensor used in the HFDF array. The array can be designed with a sensor suite consisting of superconductive quantum interference device (SQUID), SI integrated monopoles, and B-dot sensors. Multiple considerations lead to the use of a particular sensor. For example, the SQUID sensors require cryogenic equipment and cannot be placed on the wing tips. Analysis of the sensor layout takes into account maximizing the detection capability of each array element based on aircraft integration, system losses, and flight stability. The array capability defined by the locations in the research by BerrieHill, Corbin and presented in this thesis can be used to determine the best locations for sensors to define a functional HFDF array.

To fully determine the direction finding capability of the direction finding array a simulation of all array elements must be completed in CST Microwave Studio. CST Design Studio has a built in optimizer that can utilize results from CST Microwave Studio to achieve post processing optimization of the computational analysis within CST Design Studio. Based on defining the phase on each element with variable the optimizer can be set to vary all phases of the array to optimize for a given direction at a particular frequency. The phase definition for maximizing a given direction defines the steering vector for a given direction. Optimizing for a sampling of directions will define the ability for a signal processing algorithm to accomplish direction finding based on the eight and ten-element arrays. To achieve the simulations a larger GPU must be used. The Tesla M2090 GPU offers an additional 64 processors compared to the Tesla 2070 used in this research effort, but only has 6 GB of memory. The ability to double the memory is not currently available in the Tesla GPU line. To achieve double the processing power adding a second upgraded M2090 GPU. CST can utilize multiple GPUs for processing, but is limited to 2 GPUs for processing. The AFIT Low Observables Radar and Electromagnetics LORE

computing lab has multiple GPU workstations which could be used in parallel to process larger projects but would require coordination with Sonnet Software, the makers of CST, to better understand the ability of CST to use parallel computing.

The research presented in this thesis along with the efforts of BerrieHill, Corbin, and Hardin offer each a small portion of the goal of designing an airborne HFDF array. These research efforts must be combined to apply signal processing and direction finding (DF) algorithms to an array design. Corbin utilized the patterns of the SI monopoles to apply direction finding algorithms based on a set SNR [7]. Corbin's research assumes that the sensors can achieve at a minimum a 10 dB SNR [7]. By combining the sensor locations shown in this research and by BerrieHill and the efficiencies of the sensors to DF algorithms in order to better understand the angular resolution of the current array designs. Based on the angle of arrival accuracy of the current sensors the current shortfalls in the current research can be determined. It can also be decided if the capability is adequate enough to move forward with an application to aircraft testing.

Appendix A: Pattern Cuts of Eight-Element Direction Finding Array

THIS appendix includes the waterline, XZ, and YZ pattern cuts for the eight-element high frequency array normalized to 2 MHz.

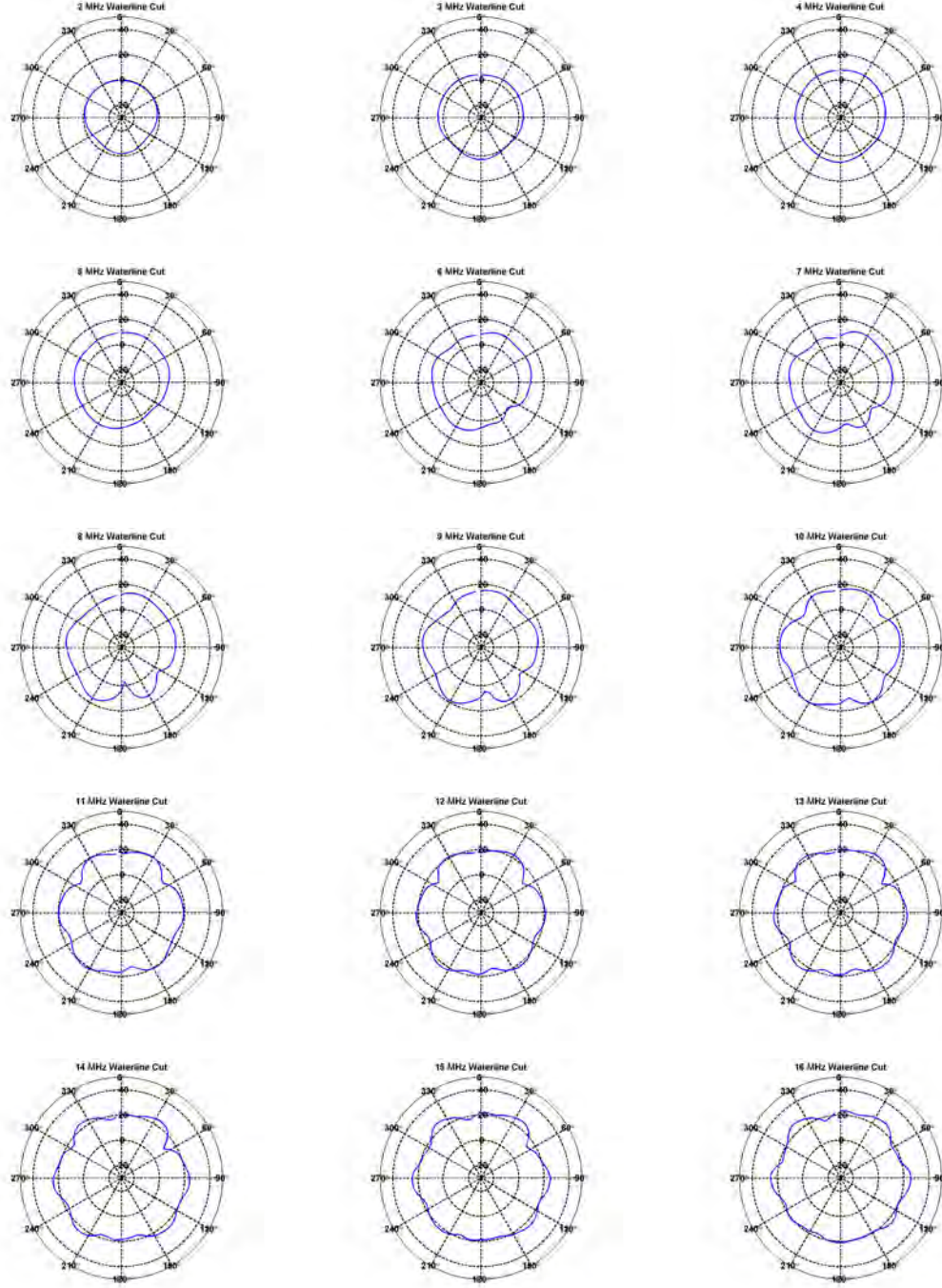


Figure A.1: Waterline cut of an eight-cluster HFDF array for 2-16 MHz normalized to 2 MHz

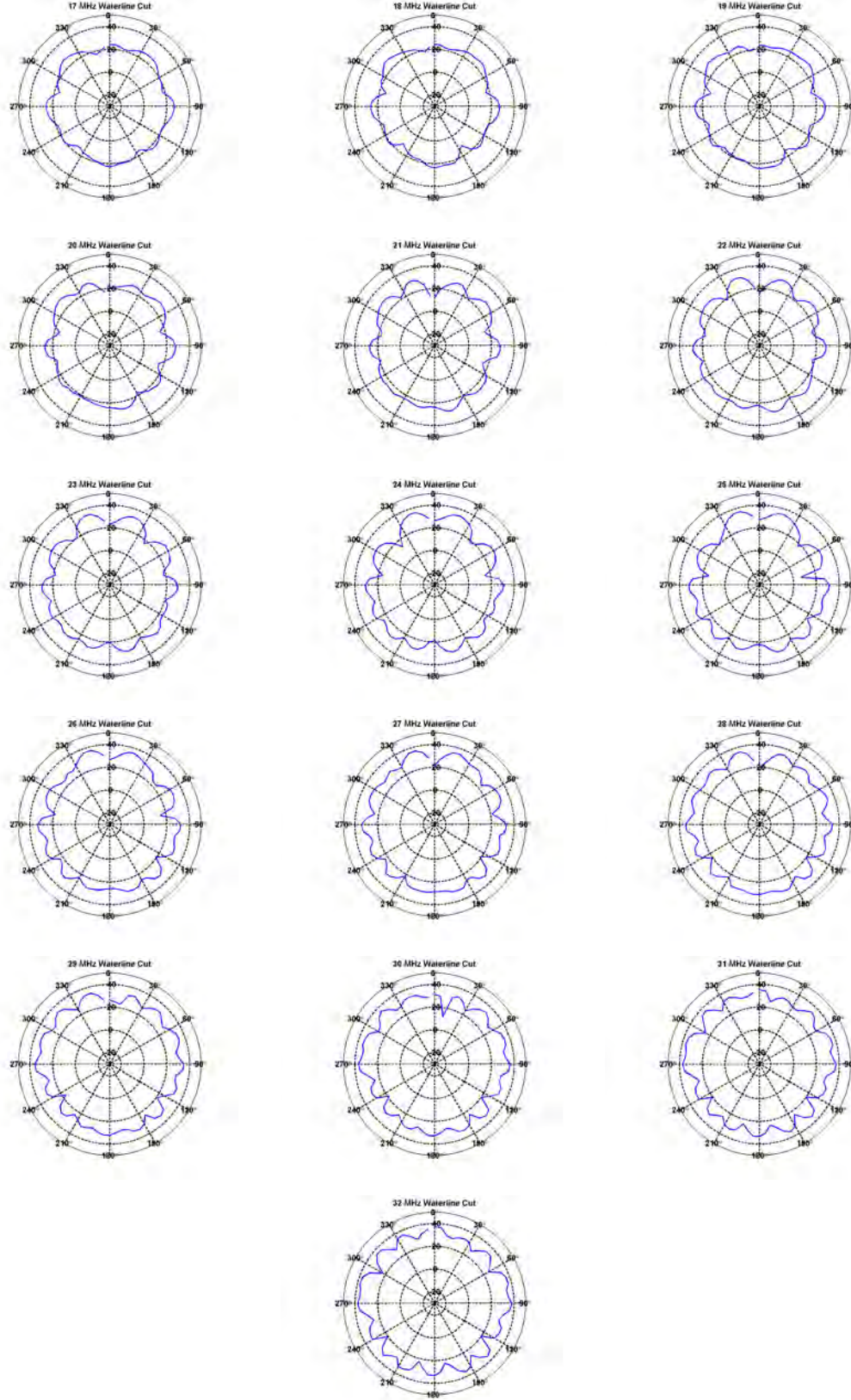


Figure A.2: Waterline cut of an eight-cluster HFDF array for 17-32 MHz normalized to 2 MHz

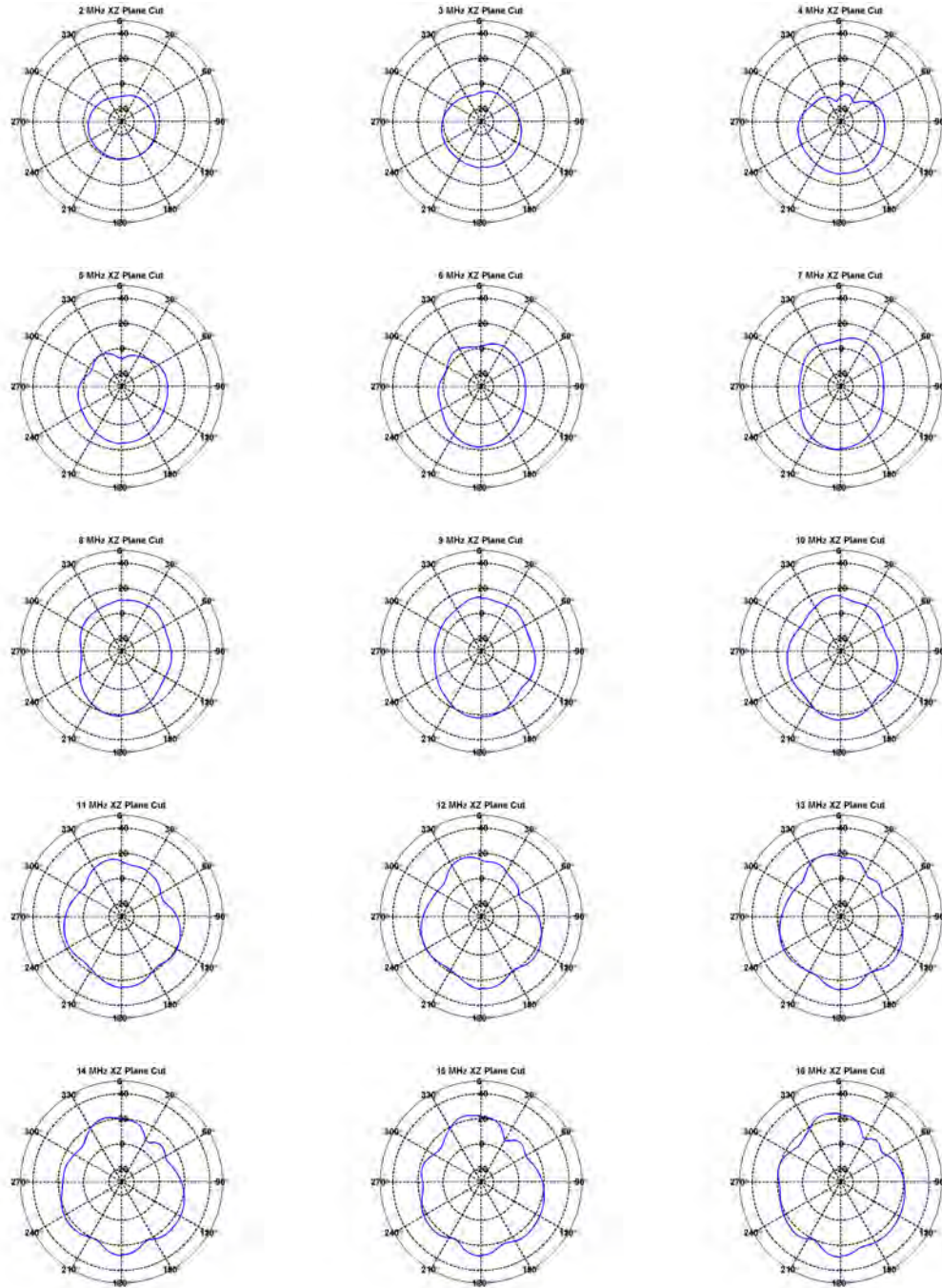


Figure A.3: XZ plane cut of an eight-cluster HFDF array for 2-16 MHz normalized to 2 MHz

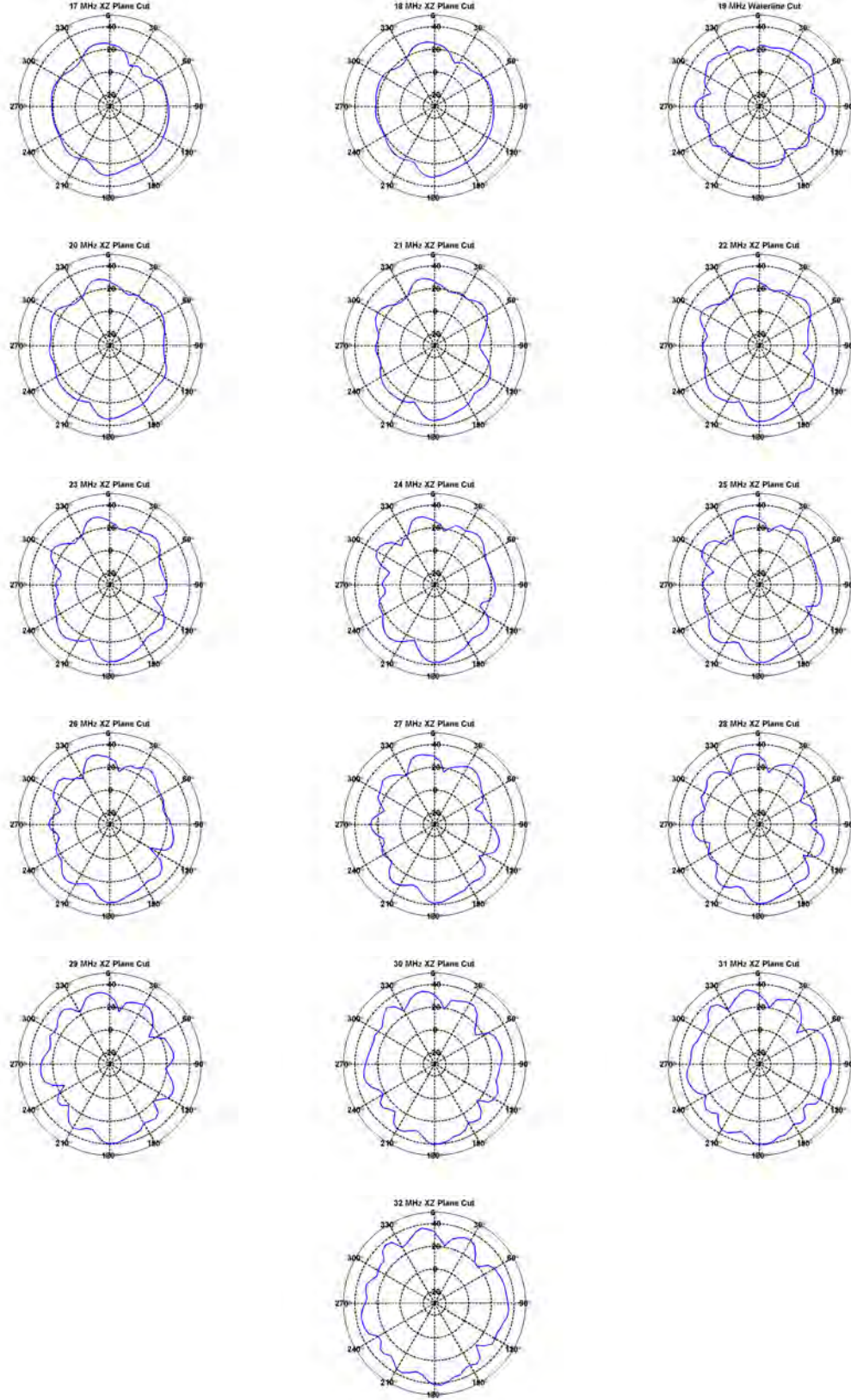


Figure A.4: XZ plane cut of an eight-cluster HFDF array for 17-32 MHz normalized to 2 MHz

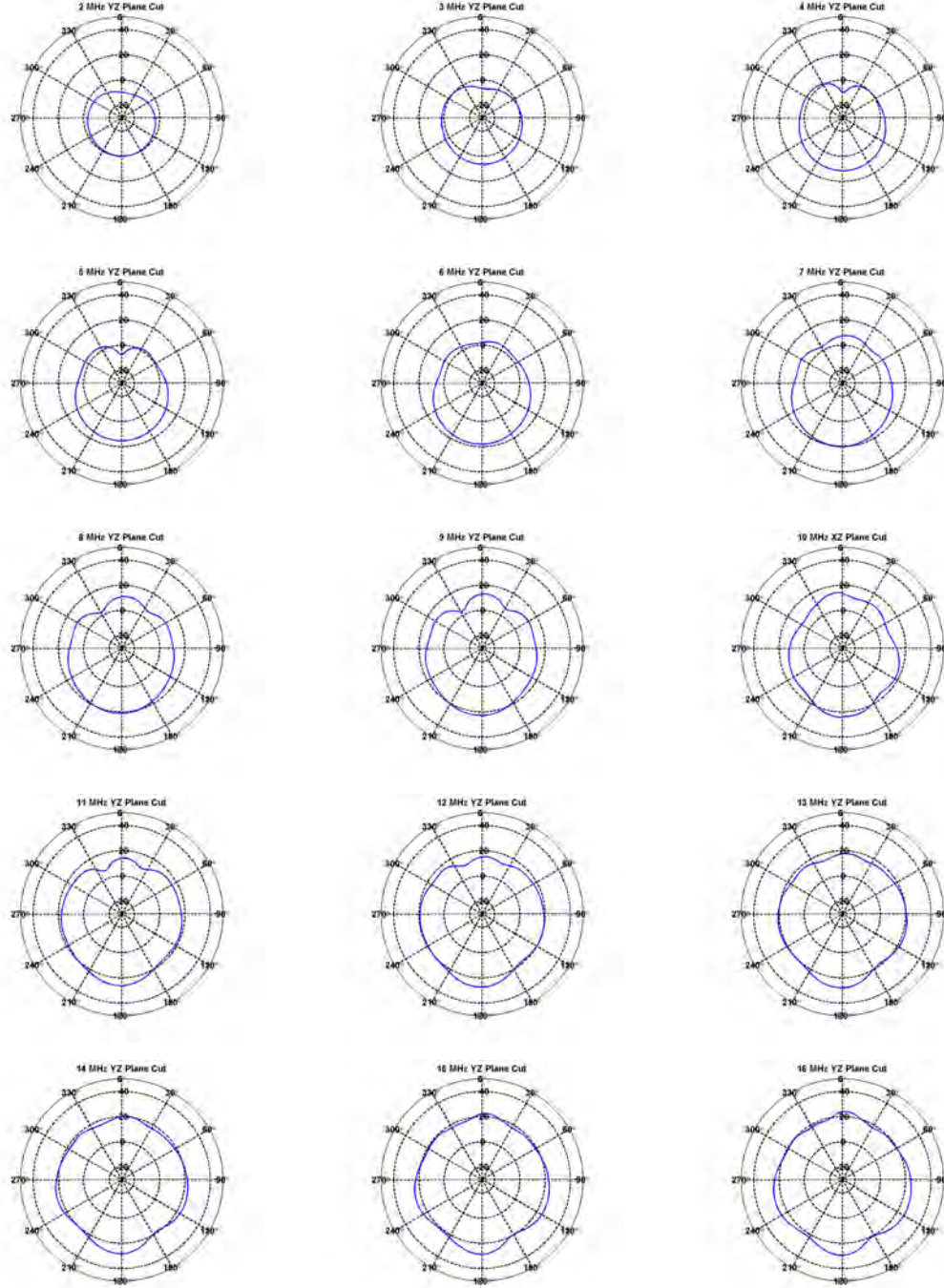


Figure A.5: YZ plane cut of an eight-cluster HFDF array for 2-16 MHz normalized to 2 MHz

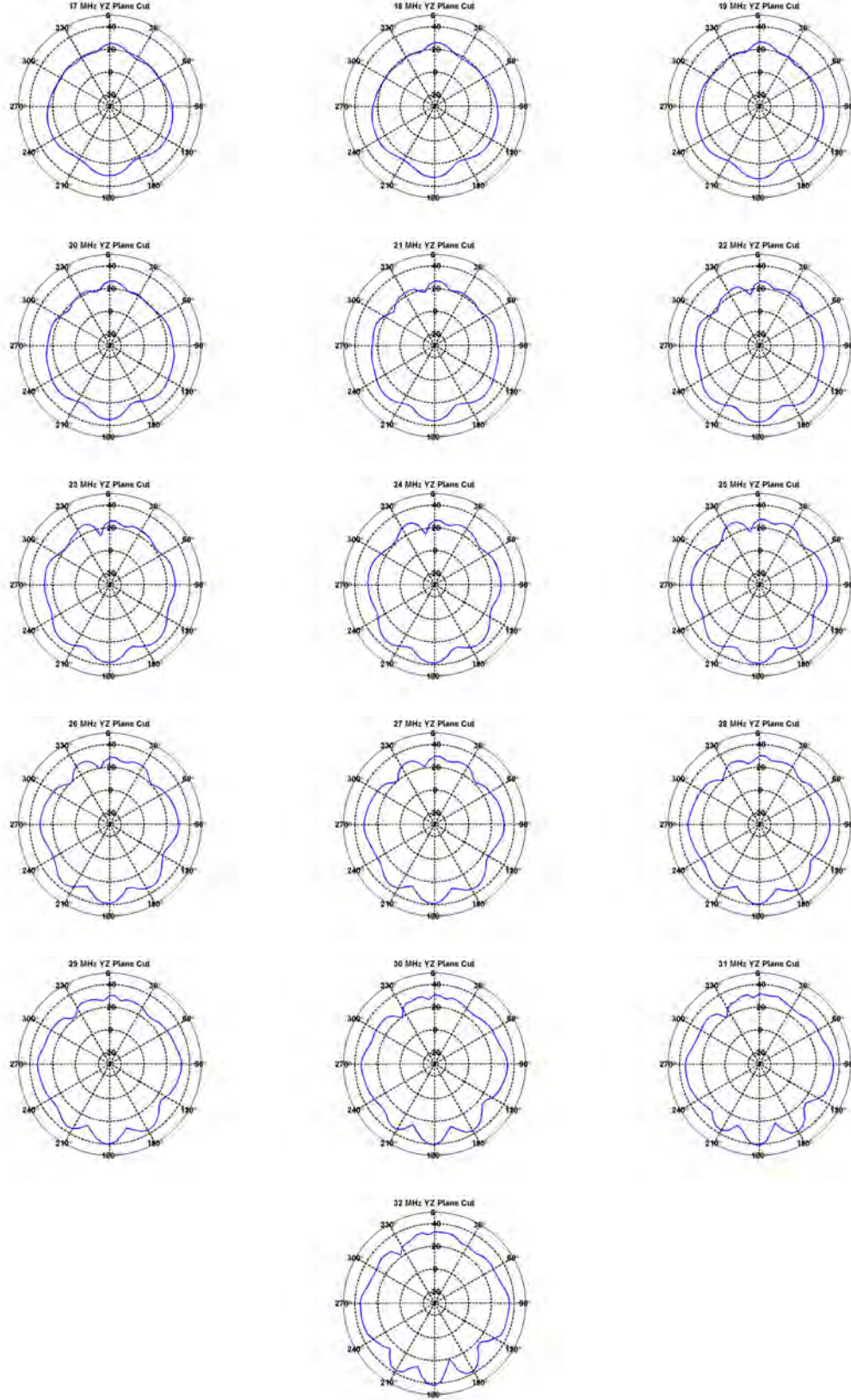


Figure A.6: YZ plane cut of an eight-cluster HFDF array for 17-32 MHz normalized to 2 MHz

Appendix B: Comparison of Eight and Ten-Element Direction Finding Arrays

THIS appendix includes the normalized waterline, XZ, and YZ pattern cut comparisons for the eight and ten-element high frequency direction finding array.

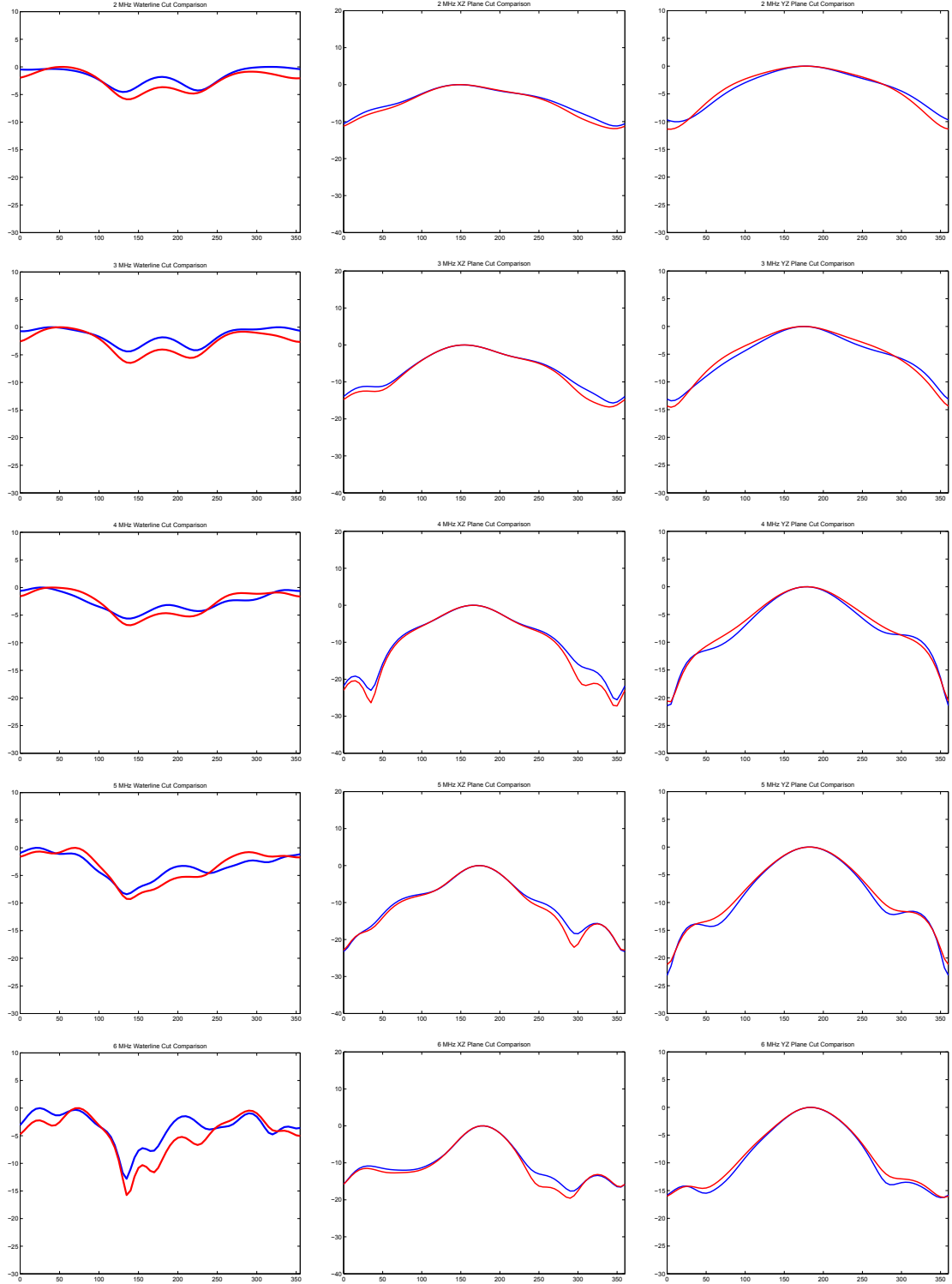


Figure B.1: Comparison of normalized waterline, XZ, and YZ plane cuts for ten vs eight-cluster array from 2-6 MHz

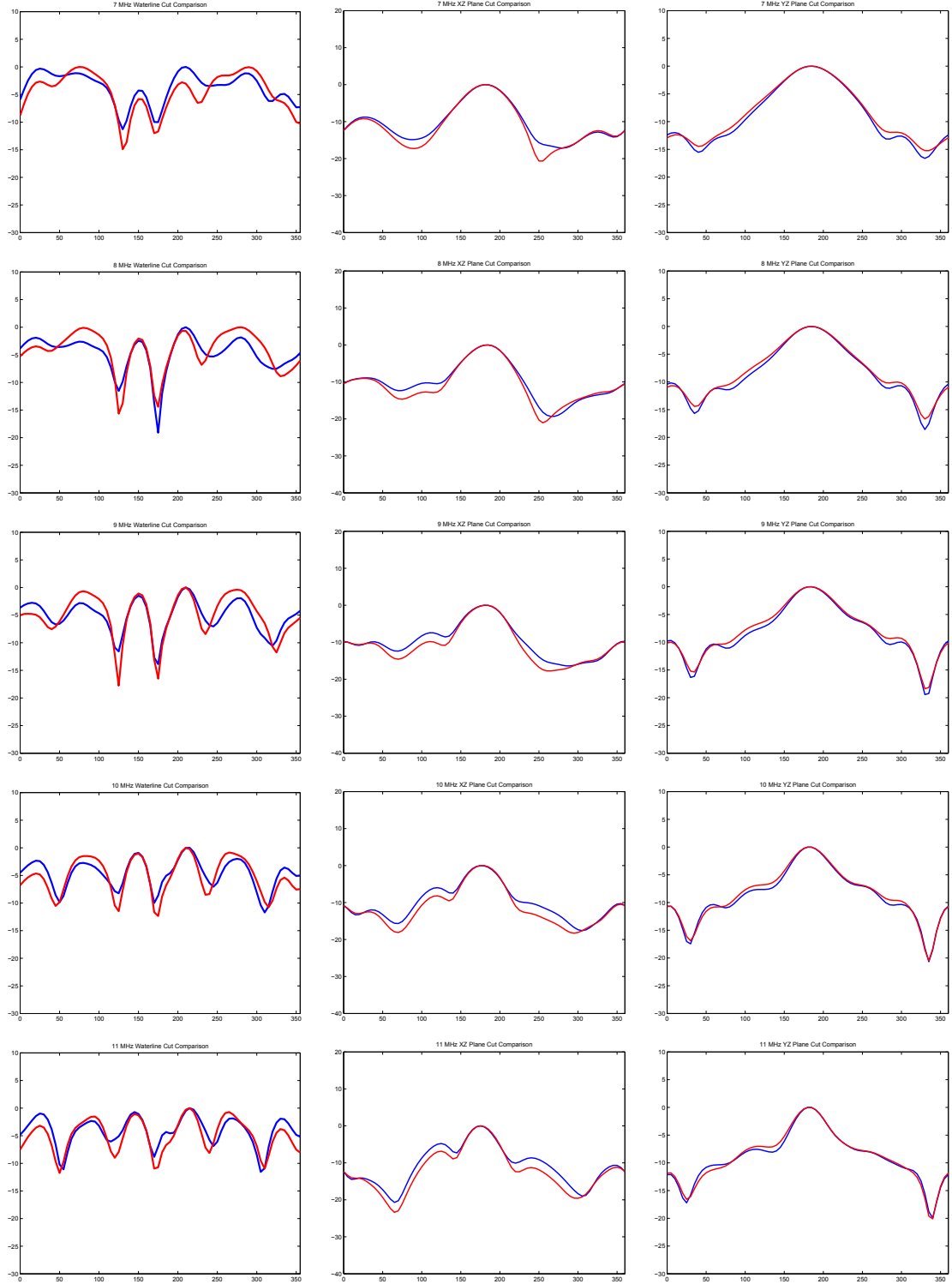


Figure B.2: Comparison of normalized waterline, XZ, and YZ plane cuts for ten vs eight-cluster array from 7-11 MHz

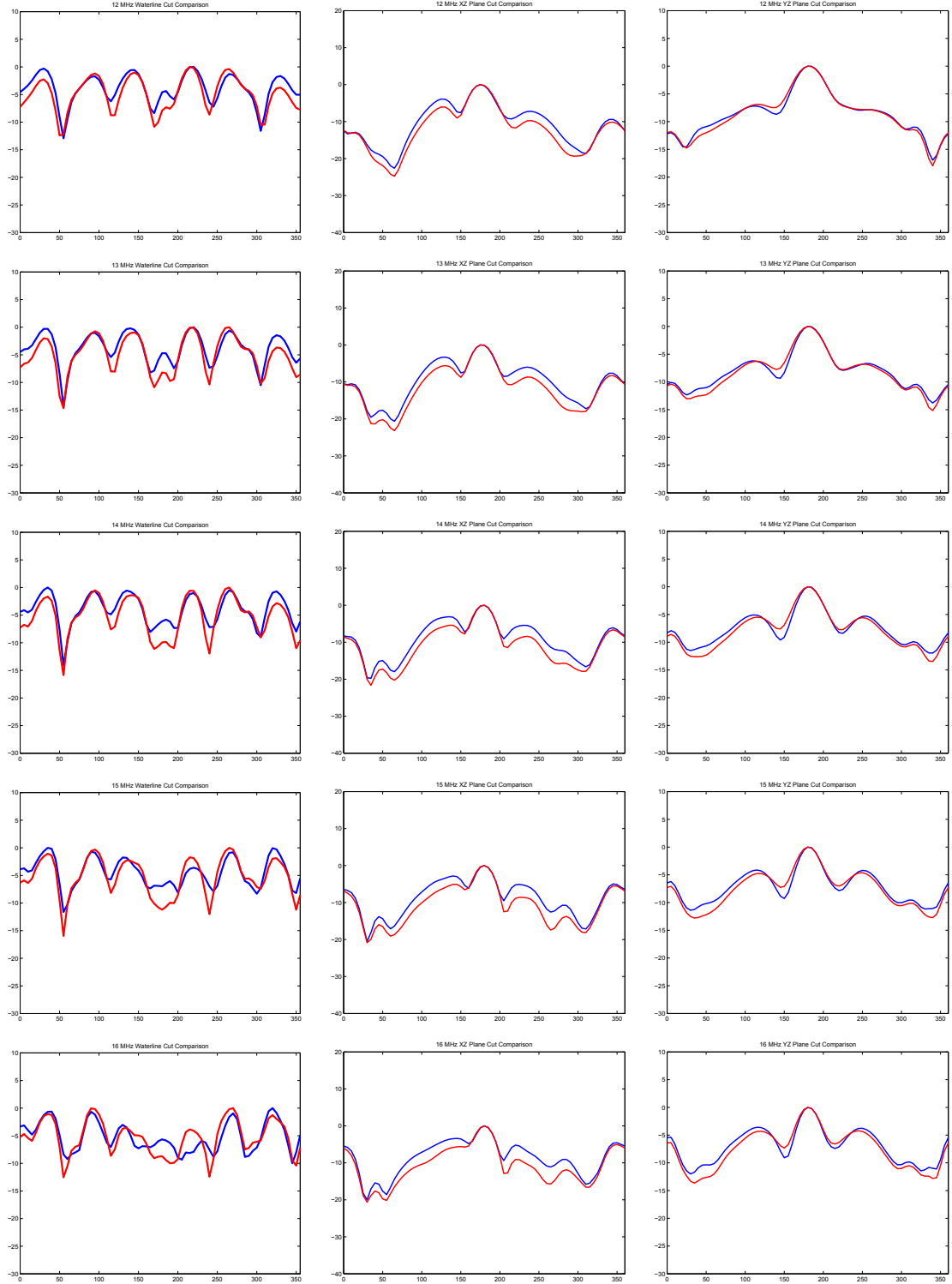


Figure B.3: Comparison of normalized waterline, XZ, and YZ plane cuts for ten vs eight-cluster array from 12-16 MHz

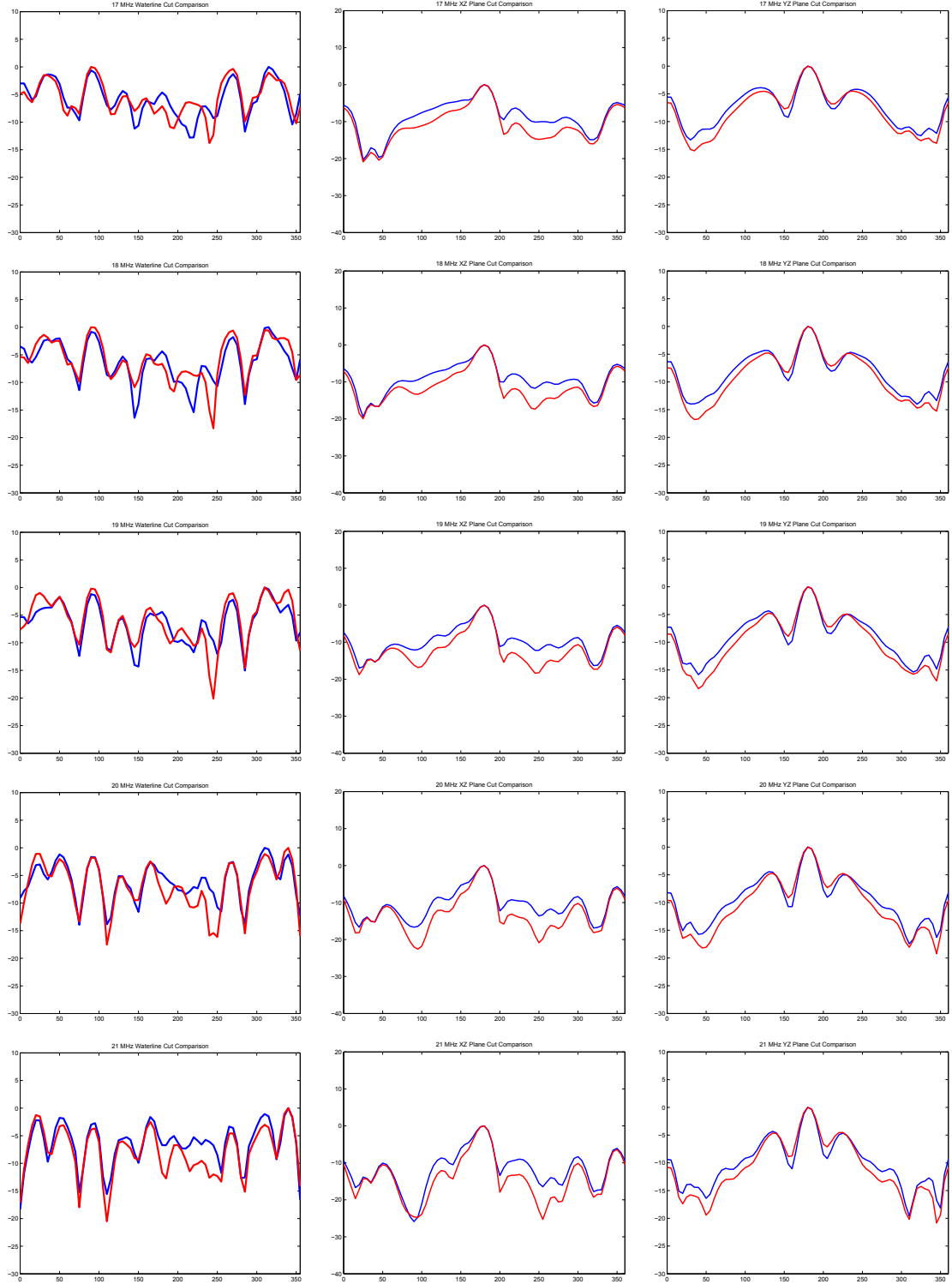


Figure B.4: Comparison of normalized waterline, XZ, and YZ plane cuts for ten vs eight-cluster array from 17-21 MHz

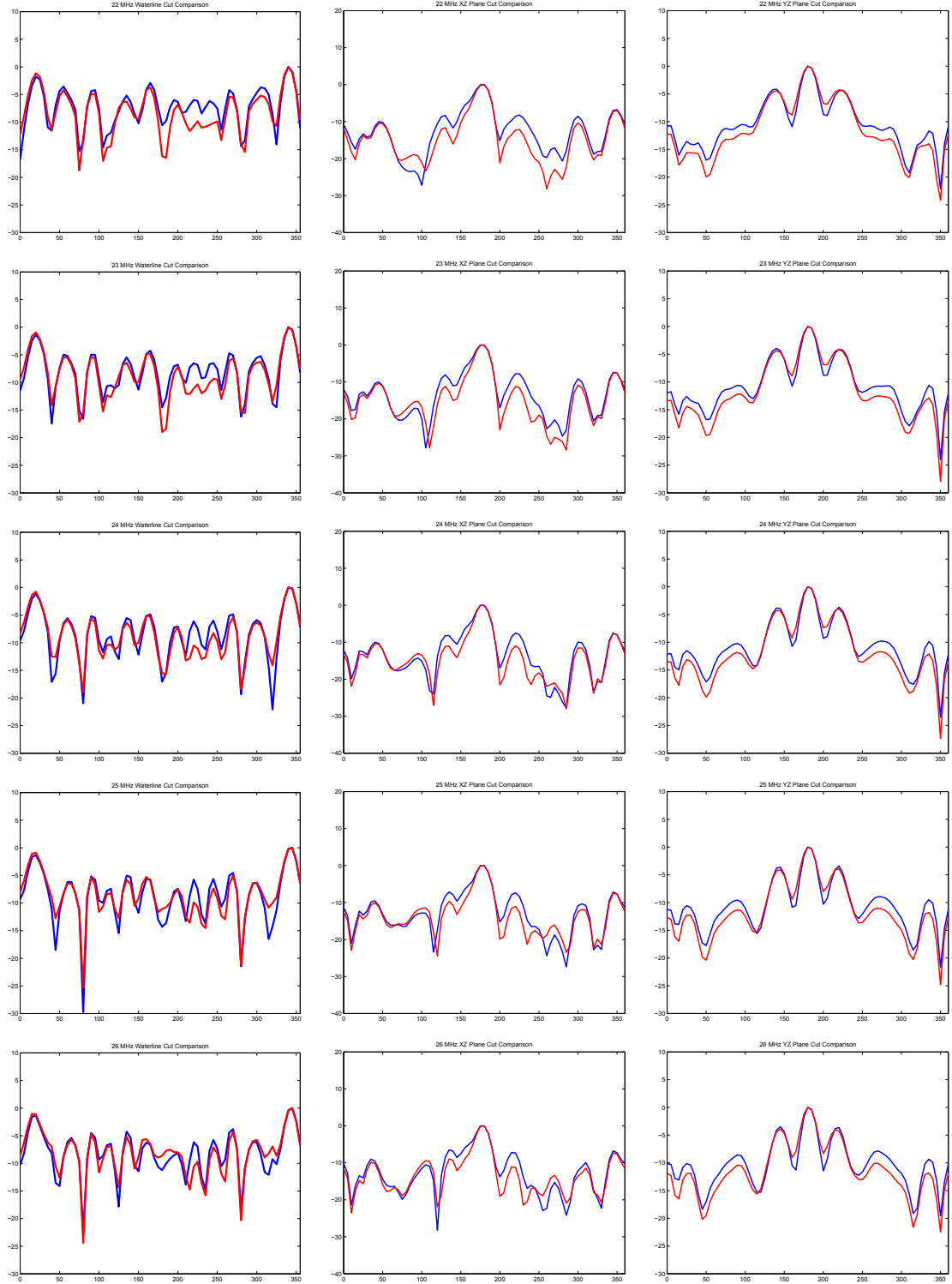


Figure B.5: Comparison of normalized waterline, XZ, and YZ plane cuts for ten vs eight-cluster array from 22-26 MHz

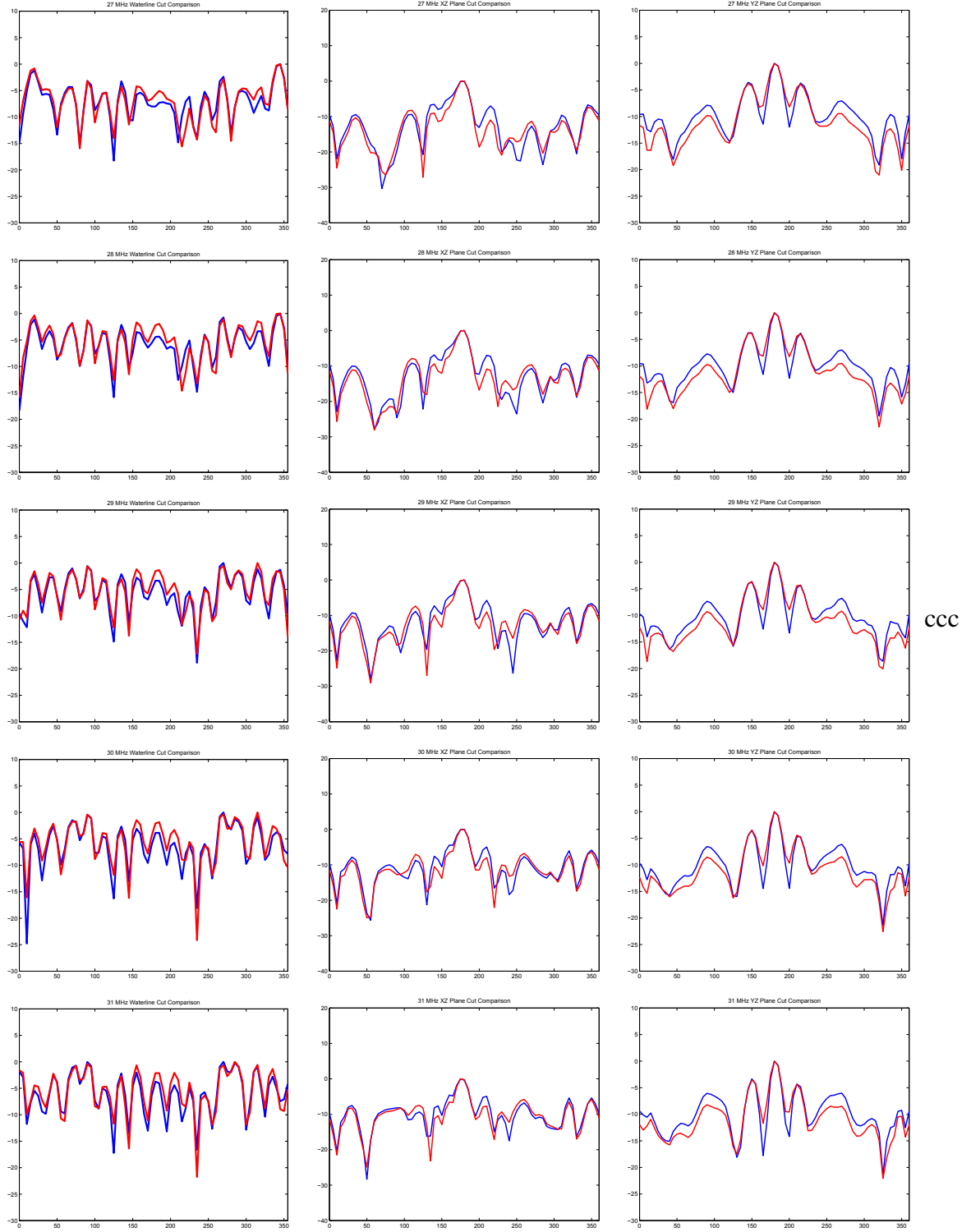


Figure B.6: Comparison of normalized waterline, XZ, and YZ plane cuts for ten vs eight-cluster array from 27-31 MHz

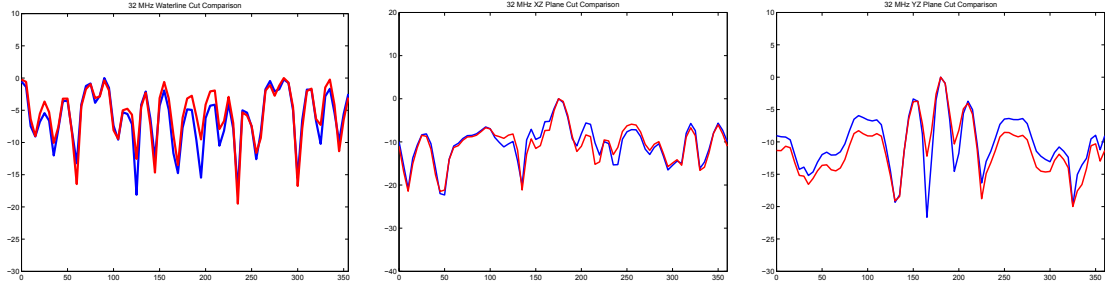


Figure B.7: Comparison of waterline, XZ, and YZ plane cuts for ten vs eight-cluster array at 32 MHz

Appendix C: Sidelobe Level for Eight-Element Arrays

THIS appendix includes the integrated and average sidelobe levels for waterline, XZ, and YZ pattern cut of the eight element high frequency direction finding array.

Table C.1: Average and integrated sidelobe level in dB for 2-19 MHz of the eight element array.

Freq (MHz)	Waterline Average	XZ Cut Average	YZ Cut Average	Waterline Integrated	XZ Cut Integrated	YZ Cut Integrated
2	-3.83	-7.07	-6.75	-72.76	-304.00	-256.62
3	-3.85	-9.32	-7.55	-57.77	-484.80	-369.72
4	-4.13	-13.01	-10.04	-132.31	-728.56	-542.33
5	-4.98	-12.58	-11.77	-189.15	-767.52	-647.57
6	-5.39	-11.98	-11.80	-204.67	-742.85	-660.84
7	-5.72	-12.06	-11.16	-217.25	-760.07	-647.49
8	-5.90	-11.64	-10.19	-295.04	-733.35	-611.51
9	-6.25	-11.02	-9.89	-337.32	-705.48	-603.03
10	-5.82	-11.32	-10.08	-296.59	-735.55	-634.74
11	-5.64	-11.92	-10.05	-248.21	-786.63	-653.48
12	-5.66	-11.64	-9.69	-237.58	-780.03	-629.68
13	-5.68	-10.68	-9.01	-238.44	-715.58	-585.45
14	-5.87	-9.84	-8.19	-252.40	-669.01	-548.92
15	-5.96	-9.59	-7.66	-291.80	-632.87	-513.27
16	-6.40	-9.16	-7.48	-351.85	-622.76	-501.39
17	-7.19	-9.44	-7.95	-388.37	-641.74	-540.90
18	-7.57	-9.82	-8.83	-424.17	-667.51	-600.68
19	-7.28	-10.37	-9.48	-444.35	-705.20	-653.82

Table C.2: Average and integrated sidelobe level in dB for 20-32 MHz of the eight element array.

Freq (MHz)	Waterline Average	XZ Cut Average	YZ Cut Average	Waterline Integrated	XZ Cut Integrated	YZ Cut Integrated
20	-7.09	-11.13	-10.09	-411.28	-767.86	-696.31
21	-7.54	-12.50	-10.65	-437.30	-862.35	-734.99
22	-7.85	-13.59	-11.05	-517.85	-937.46	-762.18
23	-8.68	-14.14	-11.23	-572.55	-975.69	-775.03
24	-9.41	-14.28	-11.22	-611.73	-984.99	-773.98
25	-9.54	-13.75	-11.05	-619.78	-948.43	-762.70
26	-8.76	-13.48	-10.74	-587.22	-929.86	-741.34
27	-7.77	-13.89	-10.29	-512.80	-958.13	-720.62
28	-6.84	-13.64	-10.30	-403.40	-941.44	-721.03
29	-7.02	-12.67	-10.51	-371.97	-874.16	-735.80
30	-7.45	-11.40	-10.45	-432.21	-786.63	-731.77
31	-7.65	-10.68	-10.21	-405.42	-736.74	-725.17
32	-7.93	-10.75	-10.38	-412.34	-752.83	-737.27

Appendix D: Sidelobe Level for Ten-Element Arrays

THIS appendix includes the integrated and average sidelobe levels for waterline, XZ, and YZ pattern cut of the ten element high frequency direction finding array.

Table D.1: Average and integrated sidelobe level in dB for 2-19 MHz of the ten element array.

Freq (MHz)	Waterline Average	XZ Cut Average	YZ Cut Average	Waterline Integrated	XZ Cut Integrated	YZ Cut Integrated
2	-4.47	-7.69	-7.35	-125.14	-346.21	-264.72
3	-4.92	-10.19	-8.04	-132.91	-530.10	-353.59
4	-5.08	-14.33	-9.93	-147.20	-802.71	-516.13
5	-6.21	-13.22	-11.22	-192.58	-806.70	-617.30
6	-6.69	-12.74	-11.27	-301.14	-789.92	-631.18
7	-6.78	-12.94	-10.62	-284.67	-815.48	-615.94
8	-6.44	-12.40	-9.93	-264.17	-781.08	-576.10
9	-6.99	-12.11	-9.55	-328.69	-774.83	-572.88
10	-6.82	-12.69	-9.80	-334.06	-825.09	-617.38
11	-6.25	-13.46	-10.10	-318.84	-888.16	-646.30
12	-6.36	-13.25	-9.80	-318.17	-888.07	-636.87
13	-6.78	-12.50	-9.28	-325.32	-837.83	-602.90
14	-7.09	-11.79	-8.65	-340.43	-801.40	-571.15
15	-7.11	-11.50	-8.23	-334.20	-782.11	-543.08
16	-6.69	-11.38	-8.13	-354.76	-773.79	-544.90
17	-7.13	-11.67	-8.84	-378.05	-793.65	-592.28
18	-7.75	-12.14	-9.75	-387.40	-825.52	-662.73
19	-8.12	-12.86	-10.54	-398.06	-874.58	-716.55

Table D.2: Average and integrated sidelobe level in dB for 20-32 MHz of the ten element array.

Freq (MHz)	Waterline Average	XZ Cut Average	YZ Cut Average	Waterline Integrated	XZ Cut Integrated	YZ Cut Integrated
20	-8.31	-13.80	-11.18	-465.43	-952.29	-760.53
21	-8.38	-15.01	-11.69	-553.11	-1035.60	-806.79
22	-8.94	-15.65	-12.17	-590.12	-1079.88	-839.64
23	-9.45	-15.91	-12.39	-623.61	-1097.95	-854.91
24	-9.60	-15.39	-12.37	-623.98	-1061.86	-853.24
25	-9.31	-14.62	-12.23	-604.98	-1008.69	-843.68
26	-8.72	-14.27	-11.96	-575.42	-984.83	-825.44
27	-7.50	-14.53	-11.66	-495.19	-1002.57	-804.29
28	-6.95	-14.24	-11.50	-347.39	-982.26	-804.81
29	-7.06	-13.26	-11.58	-338.89	-915.25	-810.84
30	-7.03	-11.90	-11.45	-379.81	-821.08	-801.59
31	-7.44	-11.03	-11.35	-364.34	-761.38	-794.66
32	-7.44	-11.02	-11.62	-364.45	-771.40	-813.24

Appendix E: BerrieHill and MGL-S8A B-dot Sensor Comparison

THIS appendix includes the plots of the comparisons between the BerrieHill structurally integrate monopole feeds and the MGL-S8A B-dot sensor at aircraft location two for 4 and 11 MHz.

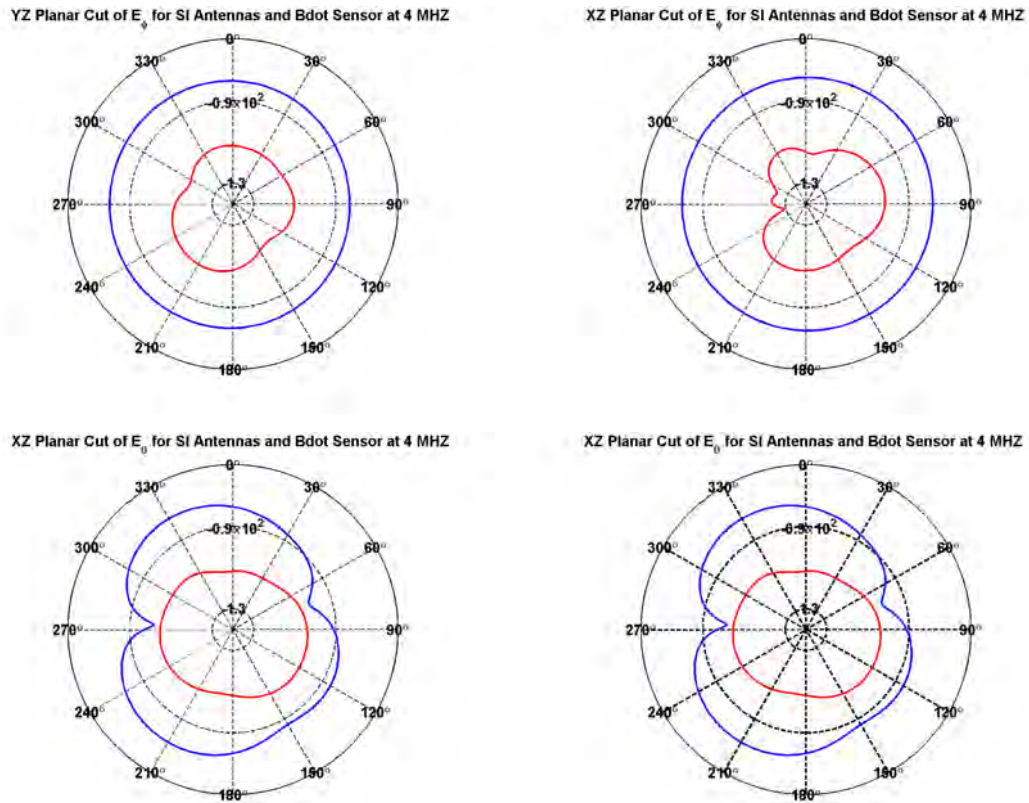
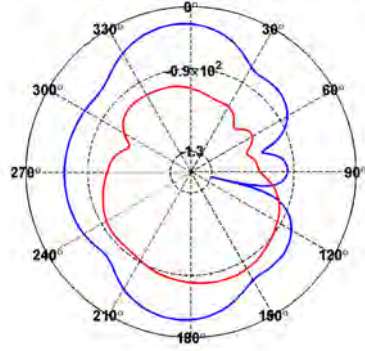
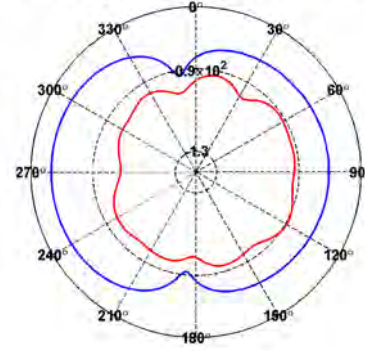


Figure E.1: XZ and YZ plane cuts for the theta and phi component of the electric field at 4 MHz of the SI monopole at location two versus B-dot sensor at location two.

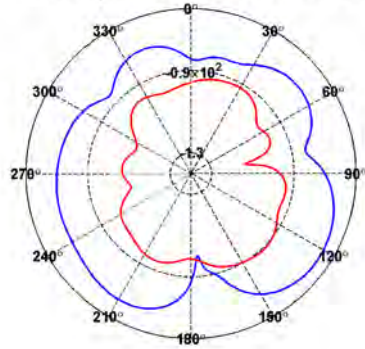
YZ Planar Cut of E_θ for SI Antennas and Bdot Sensor at 11 MHZ



XZ Planar Cut of E_θ for SI Antennas and Bdot Sensor at 11 MHZ



YZ Planar Cut of E_ϕ for SI Antennas and Bdot Sensor at 11 MHZ



XZ Planar Cut of E_ϕ for SI Antennas and Bdot Sensor at 11 MHZ

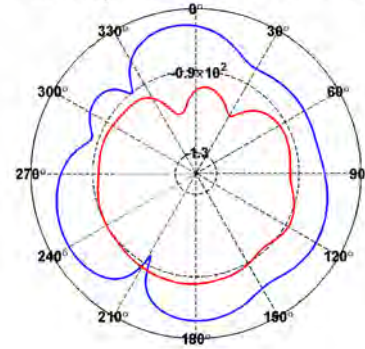


Figure E.2: XZ and YZ plane cuts for the theta and phi component of the electric field at 11 MHz of the SI monopole at location two versus B-dot sensor at location two.

Appendix F: Analysis of B-dot Test Data Using 100 msec Integration Time

THIS appendix includes the analysis of the B-dot test data using a 100 msec integration time from 26-32 MHz.

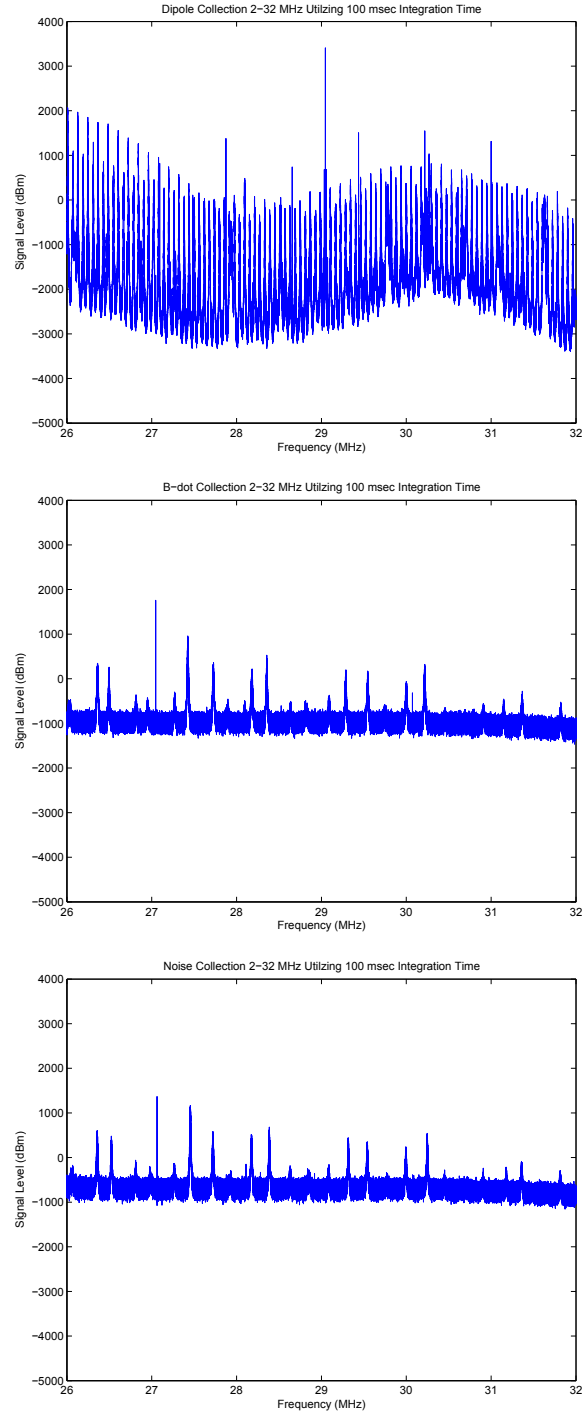


Figure F.1: Fast Fourier transform of 20 second collection with 100 msec integration time of dipole, B-dot sensor cluster, and noise from 2-32 MHz

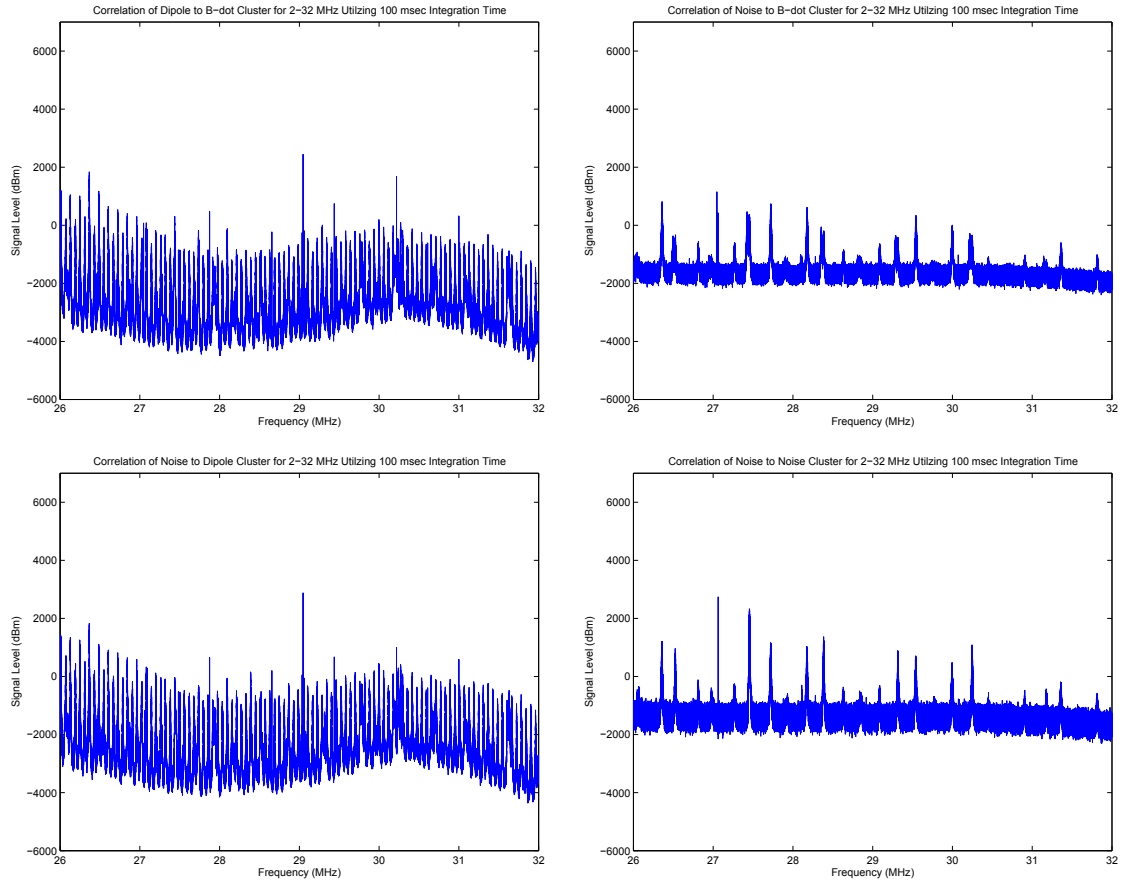


Figure F.2: Correlation of 20 second collection with 100 msec integration time of noise to B-dot cluster, noise to dipole, dipole to B-dot cluster, and noise to noise

Appendix G: Specifications Sheet For URS B-dot Sensor

THIS appendix includes the URS Corporation specifications sheet for the MGL-5 B-dot sensor and additional B-dot sensor variants.

SPECIFICATIONS										
Parameter	MGL-3		MGL-4		MGL-5		MGL-7		MGL-8	
$A_{eq} (m^2)$	1×10^{-1}		1×10^{-2}		1×10^{-3}		1×10^{-4}		1×10^{-5}	
Frequency Response (3 dB Point)	>78 MHz		>230 MHz		>700 MHz		<2GHz		<5 GHz	
Risetime (T_{r10-90})	<4.5 ns		<1.5ns		<0.5ns		<0.15ns		<0.05ns	
Maximum Output (peak)	5kV		5kV		5kV		1.0kV		150V	
Maximum Field Change	5×10^4 tesla/sec		5×10^5 tesla/sec		5×10^6 tesla/sec		1.0×10^7 tesla/sec		1.5×10^7 tesla/sec	
Output Connector	GR874L-50		GR874L-50		GR874L-50		ARM 2054-0000		ARMM 4052-0000	
Mass	25.8 kg		4.5 kg		2.7 kg		50 g		15 g	
Dimensions (cm)	Axial*	Radial*	Axial*	Radial*	Axial*	Radial*	Axial*	Radial*	Axial*	Radial*
L	9.75	97.5	66.0	43.2	35.0	28.6	10.4	5.6	7.62	2.54
W	92.7	92.7	43.2	43.2	25.4	25.4	5.6	5.6	2.54	2.54
h	38.6	38.6	13.2	13.2	6.3	6.3	2.3	2.3	1.38	1.38
T	0.47	0.47	0.25	0.38	0.35	0.35	0.25	0.25	0.10	0.10
D	--	9.9	--	9.9	--	9.9	--	1.56	--	1.19

*Note: Axial or Radial Output Specified by Designations MGL-N(A) and MGL-N(R), Respectively where N=3, 4,5,7 or 8.

Figure G.1: URS Corporation Specification Sheet for B-dot Sensor Variants

Appendix H: Comparison of MGL-S8A Air Gap and FR-4 Gap

THIS appendix includes a comparison plot of the simulated air gap filled FR-4 versus an air filled gap.

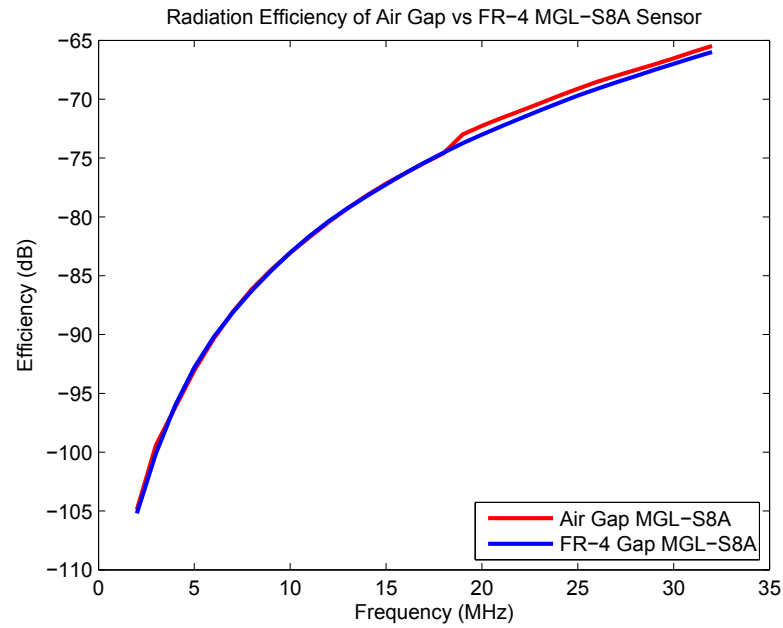
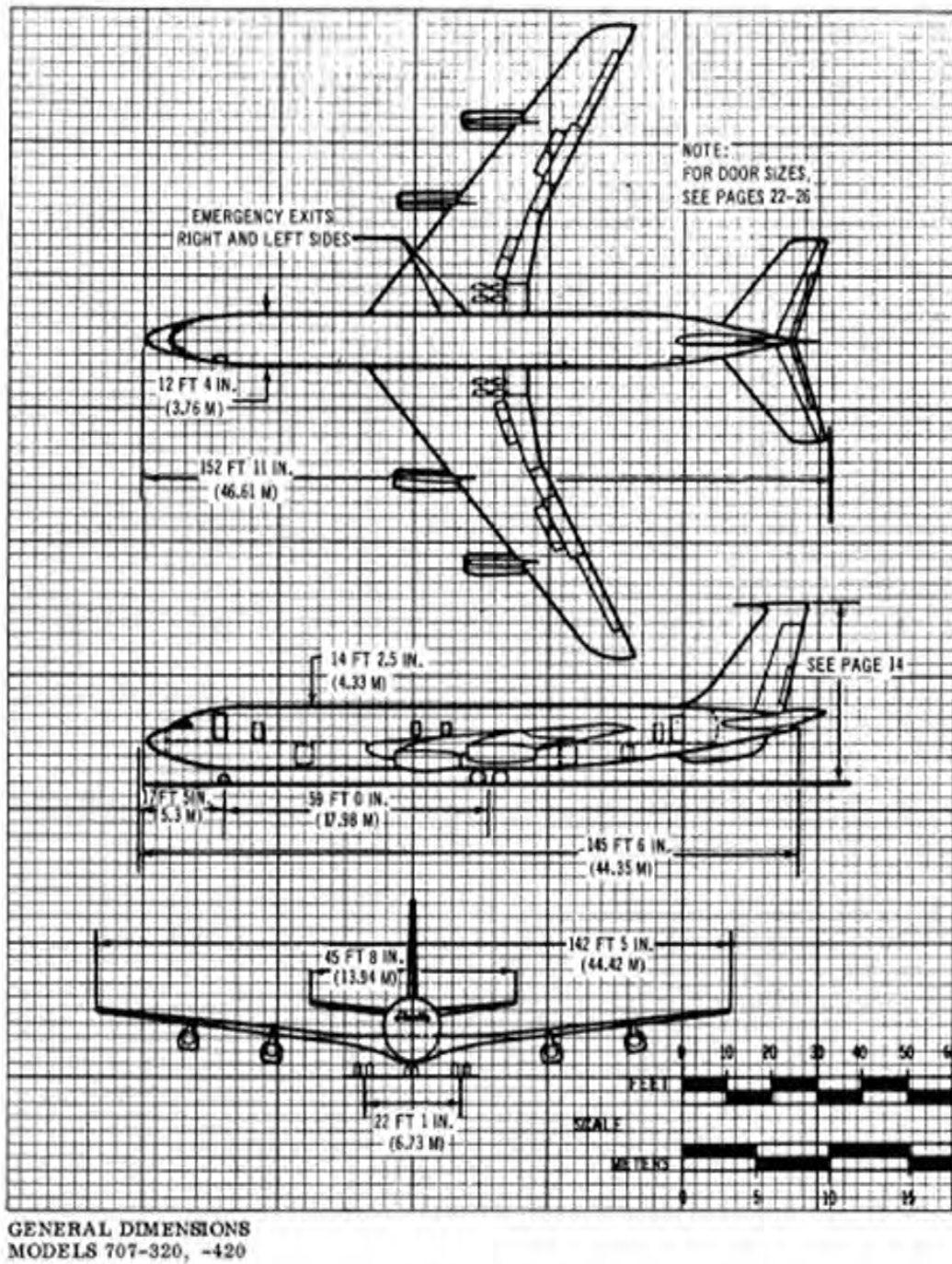


Figure H.1: Plot of radiation efficiency results for simulation of an air gap MGL-S8A and an FR-4 filled gap.

Appendix I: Boeing 707 General Specifications

THIS appendix includes the general airframe specifications for a Boeing 707 aircraft used to design the simulated aircraft for the eight and ten element arrays.



D6-55322

11

Figure I.1: Specification sheet for Boeing 707.

Bibliography

- [1] RC-135V/W rivet joint. [Online]. Available: <http://www.af.mil/information/factsheets/factsheet.asp?fsID=19540>
- [2] R. Hardin, "Magnetic field generation and B-dot sensor characterization," Master's thesis, Air Force Institute of Technology, March 2012.
- [3] The high frequency active auroral research program. electronic. 377th Air Base Wing Public Affairs.
- [4] T. Van, J. Berrie, P. Yan, M. Brewer, and D. Latypov, "Direction finding approaches for high frequency applications," BerrieHill Research Corporation, Tech. Rep., 2009.
- [5] C. A. Balanis, *Antenna Theory Analysis and Design*. John, 2005, vol. Third.
- [6] *AFI 33-106 Managing High Frequency Radios, Personal Wireless Communications Systems, and the Military Affiliate Radio System*.
- [7] C. Corbin, "High frequency direction finding using structurally integrated antennas," Master's thesis, Air Force Institute of Technology, March 2011.
- [8] J. D. Paduan, K. C. Kim, M. S. Cook, and F. P. Chavez, "Calibration and validation of direction-finding high-frequency radar ocean surface observations," *IEEE Journal of Oceanic Engineering*, vol. 31, pp. 862–874, 2006.
- [9] FCC online table of frequency allocations. [Online]. Available: <http://transition.fcc.gov/oet/spectrum/table/fcctable.pdf>
- [10] J. Phillip S. Carter, "Study of the feasibility of airborne HF direction-finding antenna systems," *IRE Transactions on Aeronautical and Navigational Electronics*, pp. 19–23, 1957.

- [11] P. Longhini, S. Berggren, A. Palacios, V. In, and A. L. de Escobar, "Coupled non-uniform bi-squid: A numerical investigation," *AIP Conference Proceedings*, vol. 1434, no. 1, pp. 1167–1174, 2012. [Online]. Available: <http://link.aip.org/link/?APC/1434/1167/1>
- [12] V. In, P. Longhini, N. Liu, A. Kho, J. D. Neff, A. Palacios, and A. R. Bulsara, "A bistable microelectronic circuit for sensing extremely low electric field," *Journal of Applied Physics*, vol. 107, no. 1, p. 014506, 2010. [Online]. Available: <http://link.aip.org/link/?JAP/107/014506/1>
- [13] J. Creekmore, T. Bronez, and R. Keizer, "Experimental results on high-frequency direction finding with modern methods," *IEEE*, pp. 73–76, 1993.
- [14] P. Cilliers, P. Coetzee, and J. Olckers, "Ionospheric mapping for HF communications and hf direction finding," in *AFRICON, 2004. 7th AFRICON Conference in Africa*, vol. 1, sept. 2004, pp. 145 –154 Vol.1.
- [15] C. A. Balanis, *Advanced Engineering Electromagnetics*. John Wiley and Sons Publishing, 1989.
- [16] M. A. Richards, J. A. Scheer, and W. A. Holm, *Principals of Modern Radar*, D. R. Kay, Ed. Scitech Publishing, 2010.
- [17] P. Stoica and R. Moses, *Spectral Analysis of Signals*. Pearson Prentice Hall, 2005, vol. First.
- [18] K. F. Warnick, *Numerical Methods for Engineering: An Introduction Using MATLAB and Computational Electromagnetic Examples*, D. R. Kay, Ed. Scitech Publishing, 2011.
- [19] International broadcast delivery. [Online]. Available: <http://www.hfcc.org/data/b11/index.phtml>

- [20] G. K. Nelson, M. A. Lombardi, and D. T. Okayama. (2005, January) NIST time and frequency radio stations: WWV, WWVH, and WWVB. National Institute of Standards and Technology. [Online]. Available: <http://tf.nist.gov/general/pdf/1969.pdf>
- [21] "Title 47 telecommunications part 97 amateur radio service," Federal Communications Commission, Tech. Rep., October 2010. [Online]. Available: http://www.access.gpo.gov/nara/cfr/waisidx_10/47cfr97_10.html
- [22] S. L. Olsen, "MGL-S8 B-dot sensor development," Air Force Weapons Laboratory, Tech. Rep., 1976.
- [23] 707 airplane description. Boeing. [Online]. Available: <http://www.boeing.com/commercial/airports/acaps/707sec2.pdf>
- [24] 707 family military derivatives. Boeing. [Online]. Available: <http://www.boeing.com/commercial/707family/deriv.html>
- [25] F. Hodjat and H. S., "Nonuniformly spaced linear and planar array antennas for sidelobe reduction," *Antennas and Propagation, IEEE Transactions on*, vol. 26, no. 2, pp. 198 – 204, mar 1978.
- [26] "MGL B-dot sensor (ground plane)," URS Corporation, Tech. Rep., 2003.
- [27] High performance receive only broadband LF, MF and HF preamplifiers. Advanced Receiver Research. [Online]. Available: <http://www.advancedreceiver.com/page46.html>
- [28] R. E. Ziemer and W. H. Tranter, *Principles of Communication: Systems, Modulation, and Noise*. Houghton Mifflin, 1990, vol. 5th.

- [29] N. Burntnyk, C. McLeish, and J. L. Wolfe, “A wide aperture sampling array for direction finding,” *IEEE Transactions on Antennas and Propagation*, pp. 248–256, 1964.

REPORT DOCUMENTATION PAGE			<i>Form Approved</i> <i>OMB No. 0704-0188</i>	
<p>The public reporting burden for this collection of information is estimated to average 1 hour per response, including the time for reviewing instructions, searching existing data sources, gathering and maintaining the data needed, and completing and reviewing the collection of information. Send comments regarding this burden estimate or any other aspect of this collection of information, including suggestions for reducing this burden to Department of Defense, Washington Headquarters Services, Directorate for Information Operations and Reports (0704-0188), 1215 Jefferson Davis Highway, Suite 1204, Arlington, VA 22202-4302. Respondents should be aware that notwithstanding any other provision of law, no person shall be subject to any penalty for failing to comply with a collection of information if it does not display a currently valid OMB control number. PLEASE DO NOT RETURN YOUR FORM TO THE ABOVE ADDRESS.</p>				
1. REPORT DATE (DD-MM-YYYY) 21-03-2013		2. REPORT TYPE Master's Thesis		3. DATES COVERED (From — To) August 2011 - March 2013
4. TITLE AND SUBTITLE High Frequency Magnetic Field Direction Finding Using MGL-S8A B-dot Sensors			5a. CONTRACT NUMBER	
			5b. GRANT NUMBER	
			5c. PROGRAM ELEMENT NUMBER	
6. AUTHOR(S) Archer, Michael D., Capt, USAF			5d. PROJECT NUMBER	
			5e. TASK NUMBER	
			5f. WORK UNIT NUMBER	
7. PERFORMING ORGANIZATION NAME(S) AND ADDRESS(ES) Air Force Institute of Technology Graduate School of Engineering and Management (AFIT/ENG) 2950 Hobson Way WPAFB OH 45433-7765			8. PERFORMING ORGANIZATION REPORT NUMBER AFIT-ENG-13-M-02	
9. SPONSORING / MONITORING AGENCY NAME(S) AND ADDRESS(ES) Air Force Research Laboratory Attn: AFRL/RMYR (Dr Charles Cerny) 2241 Avionics Circle, BLDG 620 WPAFB, OH 45433-7734 (937) 528-8248 Charles.Cerny@wpafb.af.mil			10. SPONSOR/MONITOR'S ACRONYM(S) AFRL/RMYR	
			11. SPONSOR/MONITOR'S REPORT NUMBER(S)	
12. DISTRIBUTION / AVAILABILITY STATEMENT APPROVED FOR PUBLIC RELEASE; DISTRIBUTION UNLIMITED				
13. SUPPLEMENTARY NOTES This material is declared a work of the U.S. Government and is not subject to copyright protection in the United States.				
14. ABSTRACT Aircraft based direction finding (DF) in the high frequency (HF) band is difficult due to the aircraft's size with respect to wavelength and limited azimuthal resolution. A B-dot sensor is useful for detection of the time varying magnetic field and offers improved integration into an aircraft. What the B-dot sensor gains in integration it gives up in sensitivity because it is designed for frequencies above 5 GHz. Design of an airborne HFDF array using B-dot sensors is based in maximizing the physical extent of the array and eliminating multiple main beams. The goals of this research are to complete a computational analysis of a B-dot sensor, evaluate a cluster of closely spaced B-dot sensors, and design an array of B-dot sensor clusters on a simulated airborne HFDF platform. The B-dot sensors are simulated to determine the sensitivity of the sensor and sensor cluster. Eight and ten-sensor elements are placed on a simulated airframe to characterize the direction finding capability in the HF band. Additionally, a field test is accomplished to compare the simulated B-dot sensor cluster to an actual cluster of B-dot sensors. The B-dot sensor is inadequate for use in an HFDF array due to a lack of sensitivity, but based on initial simulations a larger B-dot sensor, designed for 700 MHz, offers equivalent sensitivity to previous research. Utilizing a cluster of sensors improves the radiation efficiency by 6 dB. The eight and ten-element arrays offer a limited direction finding capability due limited sidelobe reduction. The addition of two sensors does present sidelobe reduction; therefore, additional sensors will improve the direction finding capability of the airborne HFDF array.				
15. SUBJECT TERMS High frequency, direction finding, magnetic field sensor, airborne array design				
16. SECURITY CLASSIFICATION OF:			17. LIMITATION OF ABSTRACT UU	18. NUMBER OF PAGES 137
a. REPORT U	b. ABSTRACT U	c. THIS PAGE U		
			19a. NAME OF RESPONSIBLE PERSON Lt. Col. Geoffrey Akers (ENG)	
			19b. TELEPHONE NUMBER (Include Area Code) (937)255-3636, ext (937)255-3636 x 4659 geoffrey.akers@afit.edu	